ARTIFICIAL INTELLIGENCE-EMPOWERED STRUCTURAL HEALTH MONITORING, DAMAGE DIAGNOSIS, AND PROGNOSIS OF METALLIC STRUCTURES

A Dissertation
Submitted to the Graduate Faculty
of the
North Dakota State University
of Agriculture and Applied Science

By

Zi Zhang

In Partial Fulfillment of the Requirements
for the Degree of
DOCTOR OF PHILOSOPHY

Major Department:
Civil and Environmental Engineering

July 2022

Fargo, North Dakota

North Dakota State University
Graduate School

Title

ARTIFICIAL INTELLIGENCE-EMPOWERED STRUCTURAL HEALTH MONITORING, DAMAGE DIAGNOSIS, AND PROGNOSIS OF METALLIC STRUCTURES

By

Zi Zhang

The Supervisory Committee certifies that this ***disquisition*** complies with North Dakota State University's regulations and meets the accepted standards for the degree of

DOCTOR OF PHILOSOPHY

SUPERVISORY COMMITTEE:

Dr. Zhibin Lin
Chair

Dr. Long Jiang

Dr. Nita Yodo

Dr. Qifeng Zhang

Dr. Yan Zhang

Approved:

June 29, 2022
Date

Xuefeng Chu
Department Chair

ABSTRACT

Metallic structures are the key backbone of the society and economy, which are often subjected to different types of loadings resulting cracking, corrosion, and other material discontinuity, and affecting structural integrity and safety. Therefore, ultrasonic guided wave (UGW) has been widely used for structural health monitoring (SHM) to gain a deep understanding of structural performance, assess the current state of structural conditions, and avoid potential catastrophic events.

Despite advances in technologies and methods in data process, microdamage detection still posts great challenges in their detectability. Different from conventional physics-based methods, artificial intelligence and machine learning (AI/ML) has recently fueled profound automation solutions toward signal process and data fusion, thereby dramatically overcoming the limits.

Along this vein, this study aims to propose AI-empowered SHM framework by decoding the UGW to uncover complex interconnected information among data, models, uncertainty, and risk for enhanced structural diagnosis and prognosis to improve metallic structural integrity and safety. Several structural cases, from one-dimensional plates/rods to three-dimensional pipes, were deliberately selected to demonstrate the real-world applications. Three different levels of the AI/ML approaches, from shallow learning to deep learning, are used to explore the effectiveness of the data fusion and data representation. Meanwhile, noise interference and structurally initial nonlinearity as typical structural uncertainty are included in data collection to understand the effects of data quality and uncertainty on the robustness of the proposed methods.

The results showed that the proposed method was an efficient and accuracy way to identify the damage characteristics. Results from the shallow learning demonstrated that different features had certain levels of sensitivity to damage, while the feature selection method in the shallow

learning revealed that time-frequency features and wavelet coefficients exhibited the highest damage-sensitivity. However, with the increase of noise level, the shallow learning failed in detectability.

By taking advantage of higher automation in feature extraction, the deep learning exhibited significant improvement in accuracy, robustness, and reliability for structural diagnosis and prognosis. Particularly, the higher-layer architecture could outperform the shallow learning in terms of higher effective and efficient data fusion, and enhanced their capability in decoding information over noise interference and structural uncertainty.

ACKNOWLEDGEMENTS

First and foremost, I would like to thank my advisor, Dr Zhibin Lin, for his constant advice and patient guidance throughout my doctoral work. His support and encouragement have helped me overcome many difficulties on my research. All the knowledge and skills I have learned from him will be an invaluable treasure for my whole life. He inspired me to reach toward greater self-awareness and solve problems in scientific ways from a different point of view. This will be a lifetime encouragement in my future career.

I would also like to thank Dr. Long Jiang, Dr. Nita Yodo, Dr.Qifeng Zhang and Dr. Yan Zhang for being part of my committee and for their valuable guidance and continuous attention regarding this work.

Great thanks to my colleagues, Dr. Hong Pan, Dr. Xingyu Wang, Dr. Mingli Li, and Matthew Pearson. Thank you for your contributions and help with the experimental study. I am particularly grateful to Dr. Hong Pan for his great help help in technical support and valuable discussions and comments during the thesis preparation.

Special thanks to my family. I am incredibly grateful for your steadfast support, love, and encouragement throughout this journey.

DEDICATION

To my parents.

TABLE OF CONTENTS

ABSTRACT iii

ACKNOWLEDGEMENTS v

DEDICATION vi

LIST OF TABLES xii

LIST OF FIGURES xiv

1.INTRODUCTION 1

1.1. Background 1

1.2. Problem Statement 2

1.2.1. Structural Health Monitoring in Metal Structures 2

1.2.2. Damage Diagnosis and Prognosis by Machine Learning Techniques 4

1.3. Research Objectives 6

1.4. Research Significance 6

1.5. Organization of the Dissertation 8

1.6. Reference 9

2. LITERATURE REVIEW 13

2.1. Ultrasonic Guided Waves in Structural Health Monitoring 14

2.2. Ultrasonic Guided Wave Propagation in Plate Structures 16

2.3. Ultrasonic Guided Wave Propagation in Cylindrical Structure 19

2.4. Machine Learning Methods in Structural Health Monitoring 21

2.5. Summary 23

2.6. Reference 24

3. SVM BASED ULTRASONIC GUIDED WAVE APPROACHES FOR AUTOMATED DAMAGE DETECTION 30

3.1. Introduction 30

3.2. Machine Learning Enriched Lamb Wave Approaches 31

3.3. Numerical Simulation and Data Generation 33

3.3.1. Simulation of Lamb Wave Excitation Along Metal Structures 33

3.3.2. Calibration of Simulation 34

3.3.3. Design of Scenarios and Data Augmentation 37

3.4. Feature Representation and Classification using Machine Learning 40

3.4.1. Feature Extraction Methods 40

3.4.2. Feature Selection and Criteria 42

3.4.3. Support Vector Machine for Classification 43

3.4.4. Assessment of Effectiveness of Learning Models using Roc Curves 46

3.5. Results and Discussion 47

3.5.1. Damage-sensitive Features 47

3.5.2. Effectiveness and Sensitivity of Feature Extraction Methods to Data Classification 52

3.5.3. Effectiveness of Damage Type and Size to the Robustness of Feature Captured 55

3.5.4. Effectiveness of Damage Orientation to the Robustness of Feature Captured 59

3.6. Discussion of Structural Uncertainty Related to Engineering Applications 60

3.6.1. Impacts of Structural Uncertainty Due to Noise Interferences to the Robustness of Data Classification 60

3.6.2. Impacts of Structural Uncertainty Due to Mixed Data Types to the Robustness of Data Classification 62

3.6.3. Impacts of Structural Uncertainty Due to Material Discontinuity from Weldment to the Robustness of Data Classification 65

3.7. Summary 67

3.8. References 68

4. CONVOLUTIONAL NEURAL NETWORK BASED DAMAGE DIAGNOSIS OF STRUCTRES WITH WELDMENT BY ULTRASONIC GUIDED WAVE 71

4.1. Introduction 71
4.2. Databases Generation 72
4.2.1. Calibration of Simulation 72
4.2.2. Characteristics of Ultrasonic Guided Waves 76
4.2.3. Design of Scenarios and Data Augmentation 80
4.3. Deep Learning-based Damage Detection 83
4.3.1. CNN Architecture 84
4.3.2. Convolutional Layer 85
4.3.3. Pooling Layer 86
4.3.4. Fully Connected Layer 87
4.3.5. Analyses of CNN Parameters 87
4.4. Results and Discussions 93
4.4.1. Classification Performance for Case 1 and 2: Detection of Notch-shaped Damage Location 93
4.4.2. Classification Performance for Case 3: Detection of Weld Defect Types 98
4.4.3. Classification Performance for Case 4: Detection of Damage Severities 100
4.5. Summary 102
4.6. Reference 104
5. DEEP LEARNING BASED CORROSION DETECTION OF METALLIC STRUCTURES 105
5.1. Introduction 105
5.2. Corrosion Measurement for Metal Structure 105
5.2.1. Mass Loss 105
5.2.2. Electrochemical Impedance Spectroscopy 105
5.3. Experiment of Pipeline Corrosion Process 107
5.3.1. Uncoated Pipes 107

5.3.2. Coated Pipes 109
5.4. Numerical Simulation 110
5.5. Results and Discussion 117
5.5.1. Results of Uncoated Pipe 117
5.5.2. Results of Coated Pipe 120
5.6. Summary 123
5.7. Reference 124
6. CNN BASED STRESS LEVEL PREDICTION OF STRUCTURES BY ULTRASONIC GUIDED WAVE 126
6.1. Introduction 126
6.2. Numerical Simulation 127
6.2.1. Calibration of the FE Analysis of the Ultrasonic Guided Waves through the Rod 127
6.2.2. Design of Scenarios 128
6.2.3. Data Collection and Augmentation 130
6.3. Deep Learning Framework 134
6.3.1. CNN Architecture 135
6.3.2. Feature Visualization with T-SNE 136
6.4. Results and Discussion 137
6.4.1. Feature Visualization 137
6.4.2. Classification for Prestress Levels of the Rod by CNN 139
6.4.3. Classification for Embedding Situation by CNN 144
6.5. Summary 146
6.6. Reference 147
7. DEEP CNN BASED DAMAGE DETECTION FOR STRUCTURES WITH WELDMENT BY ULTRASONIC GUIDED WAVES 148

7.1. Introduction 148
7.2. Machine Learning-based Damage Detection Method 149
7.2.1. Residual Network (ResNet) 152
7.2.2. Batch Normalization 153
7.2.3. Identity Shortcut Connections 154
7.2.4. Loss Function 155
7.2.5. Architecture of ResNet 155
7.3. Case Study 157
7.3.1. An Ultrasonic Guided Wave-based Damage Detection System of a Pipeline 157
7.3.2. Data Acquisition and Labeling 159
7.3.3. Design and Training ResNet-based Damage Detection 160
7.4. Results and Discussion 162
7.4.1. Damage Location Identification: Case 1 and 2 162
7.4.2. Identification of Welding Defect Types and Severities: Case 3 and 4 164
7.5. The Effectiveness of Damage Identification Comparing with Other Methods 166
7.6. Summary 171
7.7. Reference 172
8. CONCLUSIONS AND FUTURE WORK 174
8.1. Conclusions 174
8.2. Future Work 175

LIST OF TABLES

Table		Page
1.	Number and cost of incidence in pipelines.	2
2.	Proportions of pipeline failure for different reasons.	2
3.	Test matrix for computation modeling.	38
4.	Feature selection.	50
5.	Accuracy of different features.	51
6.	Prediction.	67
7.	Test matrix for computation modeling.	81
8.	Results of different filter sizes.	90
9.	Results of different filter numbers.	91
10.	Results of different Pooling sizes.	92
11.	Detail of the proposed CNN.	92
12.	Test matrix for pipes.	108
13.	Test matrix for pipes.	109
14.	Test matrix for pipe models.	112
15.	Experience results.	119
16.	Experience results.	123
17.	Test matrix for computation modeling.	130
18.	Details of the proposed CNN.	136
19.	Confusion matrices in various noise levels.	141
20.	Confusion matrices in Case 2.	143
21.	Confusion matrices in Case 3.	144
22.	Confusion matrices in varying embedding conditions.	145
23.	Detail of the proposed ResNet-20.	156

24. Data acquisition and labeling. 160
25. The result in Case1 168
26. The result in Case2 168
27. The result in Case3 168
28. The result in Case4 169

LIST OF FIGURES

Figure		Page
1.	Dispersion curves. (a) phase velocity and (b) group velocity.	18
2.	Phase velocities and group velocities.	21
3.	Framework of machine learning-enriched method for damage detection.	32
4.	Excited Lamb wave in the simulation.	35
5.	Aluminum beam.	35
6.	Wave propagation through the span.	36
7.	Comparison of the results. (a) Undamaged state predicted by the proposed work and literature(Giurgiutiu, Bao et al. 2003); (b) Damage state with 8-mm crack predicted by the proposed work and the literature (Giurgiutiu, Bao et al. 2003).	36
8.	The signal received at sensors A-E predicted by the proposed work.	37
9.	Noise level: (a) Original signal; (b) SNR = 120 dB; (c) SNR = 100 dB; (d) SNR = 80 dB.	40
10.	Full fifth level wavelet transform.	42
11.	Features in time domain. (a) Amplitude; (b) RMS; (c) correlation coefficient.	48
12.	Features in frequency domain.	48
13.	Features in time-frequency domain.	49
14.	Weight of each feature under different noise levels.	50
15.	Received signals through Pitch-catch method.	53
16.	Damage features distribution (SNR=90dB).	53
17.	Received signals through Pitch-catch method.	54
18.	Feature distribution under two different noise levels.	55
19.	Classification of damage types under two noise levels.	56
20.	Classification of damage sizes under two noise levels.	57
21.	The ROC curves for multiclass: (a) Comparison between State #1 and #7; (b) Comparison between State #1 and #8.	58

22. Received signals through Pitch-catch method. 59

23. Damage identification results. 60

24. Damage identification to noise interference: (a) Damage type; (b) Damage size; (c) Damage orientation. 62

25. Data classification for mixed data types: (a)-(c). 64

26. Plate with weldment and 6 mm-long notch-type damage (a)-(b). 66

27. Classification of damage sizes under two noise levels. 67

28. Comparison of the results. 73

29. The pipeline model with notch-shaped damage and weldment. 75

30. Experiment setup. 75

31. Calibration of experiment and simulation: (a) Pipeline with undamaged state; (b) Pipeline with welding and notch. 76

32. Signal characteristics under varying mechanical damage integrated with weldment: (a) intact pipe; (b) pipe with grith weld; (c) pipe with crack; and (d) pipe coupled with weldment and mechanical damage. 79

33. Welding defects (a) Lack of fusion; (b) Cracks; (c) Undercut; (d) Lack of penetration 81

34. Wave propagation through the whole span. (a) ~ (f) 82

35. Signals with different noise levels. (a) Original signal; (b) SNR = 100 dB; (c) SNR = 80 dB; (d) SNR = 60 dB 83

36. Flowchart for the damage detection by CNN 84

37. Flowchart for the damage detection by CNN 85

38. Convolutional layer 86

39. Pooling layer. 87

40. Weights of the third convolutional layer at 60 dB 89

41. Feature maps. (a) SNR = 100 dB; (b) SNR = 60 dB. 94

42. Training and validation results: (a) SNR = 80 dB; (b) SNR = 70 dB; (c) SNR = 60 dB. 95

43. Training and validation results: (a) SNR = 80 dB; (b) SNR = 70 dB, (c) SNR = 60 dB. 95

44. Testing results: (a) SNR = 80 dB (100%); (b) SNR = 70 dB (92.33%). 96

45. Testing results: (a) SNR = 70 dB (95%), (b) SNR = 60 dB (68%). 98

46. Location identification in pipeline. 98

47. Training and validation results: (a) SNR = 70 dB; (b) SNR = 60 dB. 99

48. Testing results: (a) SNR = 70 dB (99.4%); (b) SNR = 60 dB (75.4%). 100

49. Training and validation results: (a) SNR = 80 dB; (b) SNR = 70 dB. 101

50. Testing results: (a) SNR = 80 dB (100%); (b) SNR = 60 dB (88.75%). 102

51. Locations defect in pipeline. 102

52. Equivalent electric circuit models (Nair, Cai et al. 2019)..... 107

53. Experiment set up 109

54. Experiment samples. 110

55. Model of pipes with and without weldment in different aging states..... 111

56. Calibration of numerical simulation. 113

57. Guided waves propagated through the pipe. 114

58. Guided waves propagated through the corroded pipe..... 114

59. Signals from different states (a)-(f)..... 116

60. Training and validation results..... 118

61. Testing results: (a) SNR = 100 dB, accuracy = 100%; (b) SNR = 60 dB, accuracy = 93%. 119

62. Training and validation results..... 120

63. Testing results: (a) SNR = 100 dB, accuracy = 100%; (b) SNR = 60 dB, accuracy = 93.5%. 121

64. EIS test and the materials in chamber. 121

65. Experiment results. 122

66. EIS results. 122

67. Damage index. 123

68. Calibration of the FE model. 128

69. Rod models. 129

70. Received signals in different stress levels. (a) zero; (b) 20% UST; (c) 40% UTS; (d) 60% UTS; (e) 80% UTS. 132

71. Received signals for rods with different grout methods. (a) no grout; (b) grease; (c) cement. 133

72. Received signal in different noise level. 133

73. Flow chart of CNN. 134

74. Feature visualization by t-SNE. (a) Feature maps in first convolutional layer; (b) Feature maps in the last layer. 138

75. Feature maps: (a) 0% UTS; (b) 20% UTS; (c) 40% UTS; (d) 60% UTS; (e) 80% UTS. 138

76. Feature visualization by t-SNE: (a) SNR = 100 dB; (b) SNR = 70 dB; (c) SNR = 60 dB. 139

77. Learning result of CNN at various noise levels: (a) Training curve; (b) Test curve. 140

78. Results of CNN at various noise levels: (a) Case 2; (b) Case 3. 142

79. Results of CNN at various noise levels. 145

80. Frameworks of machine learning based damage detection methods: (a) shallow learning, (b) deep learning. 151

81. The architecture of 20-layer ResNet. 153

82. The building block of ResNet. 154

83. Calibration of simulation. 158

84. Simulation model of the pipeline. 159

85. Feature maps in ResNet. 162

86. Result of notch-shaped damage location (pipe with health welding): (a) SNR = 80 dB; (b) SNR = 70 dB.. 164

87. Result of notch-shaped damage location (pipe with welding defects): (a) SNR = 70 dB; (b) SNR = 60 dB. 164

88. Result of damage types: (a) SNR = 70 dB; (b) SNR = 60 dB. 165

89. Result of damage severity: (a) SNR = 70 dB; (b) SNR = 60 dB. 166

90. Parametric comparison in different models in Case 2 (70 dB). 170

91. Parametric comparison in different models in Case 2 (60 dB). 170

1. INTRODUCTION

1.1. Background

Large-scale metallic structures, including steel building, bridges, railways and pipelines, form the networks of our society and economy (Holnicki-Szulc and Soares 2004, Farrar and Worden 2010). However, these structures are often vulnerable to various damage due to aging and various operational loadings and environmental attacks. Therefore, it is crucial to identify the potential risk due to mechanical damage and assess the current state of the structures.

Take metallic pipelines as an example, the United States has over 2.2 million miles of pipelines for gas transportation and 228 thousand miles of pipelines for hazardous liquid transportation in 2020. According to the information reported from 2015 to 2020 from the Pipeline and Hazardous Material Safety Administration (PHMSA) of the Department of Transportation (DOT), about 600 incidents occurred each year, leading to more than 3 billion dollars on repair and retrofitting. Table *2*. Proportions of pipeline failure for different reasons. shows the statistical data on the number and cost of serious accidents in these serviced pipeline networks, where 45% of the failure cases were stemmed from the material/weld/equip, 16% was due to corrosion, and 11% came from third-party damage (as shown in Table *2*). In response to this, structural health monitoring is essential to understanding structural performance, assessing structural conditions, and providing real-time decision-making.

Currently, Various nondestructive evaluation techniques are used for assessing the integrity of structures according to their materials and damage types. However, most of the scheduled inspections require the structure to be closed or out of service during the entire inspection period, as well as expensive equipment and a large number of trained personnel (Dib 2014). Therefore, high performance of structural health monitoring is much necessary for metallic structures.

Table 1. Number and cost of incidence in pipelines.

Year	incident	Total cost
2015	712	$351,449,851
2016	632	$376,497,725
2017	647	$341,277,963
2018	634	$2,253,734,655
2019	656	$335,567,452
2020	578	$339,095,134

Table 2. Proportions of pipeline failure for different reasons.

Failure reason	Proportion
Material/weld/equip failure	45%
corrosion	16%
Excavation damage	12%
Incorrect operation	12%
Other outside force damage	7%
Natural force damage	4%
All other causes	4%

1.2. Problem Statement

1.2.1. Structural Health Monitoring in Metal Structures

In recent years, structural health monitoring (SHM), which envisions the performance of the structure at the serving stage, has become more significant in civil engineering. It aims to make a real-time damage inspection instead of schedule-driven inspections, which could extend the serving period of the structures, reduce the cost, and improve safety (Giurgiutiu 2007). Traditional

methods, where the results can be obtained by processing and analyzing the reception, usually consist of transducers for actuation and sensors for the reception. Several methods have been proposed, including vision-based techniques(Feng and Feng 2016, Pan, Zhang et al. 2019), vibration-based techniques (Doebling, Farrar et al. 1998, Kong, Cai et al. 2014, Kong, Cai et al. 2017), guided wave-based techniques, and so on. However, vision-based techniques, such as using the digital camera to capture the damage or detect the model shape of the structure, are difficult to detect minor and inner damage like crack or corrosion on a micro-scale. As for vibration measuring methods, it usually needs a huge number of sensors and a data acquisition system. In addition, some passive methods, such as acoustic emission, can only detect the occurrence of damages Compared with low-frequency vibration detection methods, guide waves, an active method, involve higher frequency waves that can detect more minute damage and structural damping has less influence on it (Mitra and Gopalakrishnan 2016).

The SHM techniques can be classified into five levels (Goyal, D. et al. 2016, Kralovec and Schagerl 2020): Level 1 is to detect the presence of damage in the structure; level 2 is to determine the geometric location of damage; Level 3 is to quantify the damage severities; Level 4 is to classify the damage types; Level 5 is to assess the condition of structural integrity. Some of the research focused on the issues only related to a single level of SHM. This study is concerned with data-driven based damage detection of metallic structures by ultrasonic guided waves and focused on multiple strategies. On the one hand, ultrasonic guided waves can be utilized in long-distance inspection with less energy loss. On the other hand, ultrasonic guided waves are cost-effective and sensitive to tiny defects. Therefore, the guide waves can be useful for structural damage detection, especially for metallic structures.

1.2.2. Damage Diagnosis and Prognosis by Machine Learning Techniques

Traditional damage diagnosis and prognosis techniques involved four main steps: (1) data acquisition, (2) signal processing, (3) feature extraction and selection, and (4) setting up a physical model and validation (Duan, Shi et al. 2020). For each step, a broad range of methods has been proposed with their advantages for different structures, which achieved credible results to some extent (Raghavan 2007, Raghavan and Cesnik 2007). However, some impediments have existed to these methods. On the one hand, it is difficult to judge the quality among of techniques. The choice of each method leads to a substantial impact on the results and the existence of uncertainties may cause the deviation of the prediction. On the other hand, handling large sensor datasets is a limitation for conventional SHM approaches replied on physics-based models. However, these issues can be solved by machine learning methods in most cases.

Recently, the data-driven machine learning techniques are rapidly evolving and have already exploded in SHM, damage diagnosis, and prognosis systems, such as structure health diagnosis and estimation of life expectance (Zhang, Pan et al. 2019, Zhao, Yan et al. 2019, Zhang, Pan et al. 2020). Compared to traditional approaches, machine learning methods have lower requirements for the measurement noise, more simple steps for data processing (Azimi, Eslamlou et al. 2020) and higher performance for operating large capacity datasets. The literature review indicated that some studies have attempted to utilize the capability of machine learning for enhancing damage inspection in SHM systems. For instance, He et al. proposed a novel fault detection method by a *k*-nearest neighbor which is a nonlinear classifier to make decisions based on local neighbors in 2007 (He and Wang 2007). an artificial neural network (ANN) was employed by Su et al. (Su and Ye 2004) to set up a quantitative identification shame for delamination in composite structures. Later, support vector machine (SVM) operated by optimization algorithms

was applied as a classifier to identify the damage of a three-story frame structure. recently emerging machine learning, particularly deep learning, could provide potential solutions to improve the signal process of the guided waves (Hong, Gui et al. 2018, Lin, Pan et al. 2018, Zhang, Pan et al. 2021, Zhang, Pan et al. 2022). The deep learning algorithms have been employed in time series (Abdeljaber, Avci et al. 2017, Pan, Azimi et al. 2018, Pan, Gui et al. 2018, Fawaz, Forestier et al. 2019, Zhang, Wang et al. 2019) and image processing (Cha, Choi et al. 2017, An, Jang et al. 2018, Cha, Choi et al. 2018, Pan, Zhang et al. 2019). Guo et al. (Guo, Xie et al. 2014) utilized a sparse coding-based deep learning algorithm to process wireless sensory data of a three-span bridge. The features of the dataset were learned by sparse coding and then trained by the network. Cha et al. (Cha, Choi et al. 2017) proposed a vision-based method by deep learning network to detect the concrete cracks without calculating the features. The comparative study indicated that the deep learning-based technique had better performance than the conventional physics-based methods. Furthermore, Cha et al. (Cha, Choi et al. 2018) investigated the fast region-based convolutional neural network to detect five types of damage in real-time. Zhang et al. (Zhang, Peng et al. 2017) proposed a CNN framework with some convolutional kernels to identify the vibration signals. While deep learning approaches have been successfully used in many aspects of structural health monitoring, less research is involved in deep learning-based ultrasonic guided wave diagnoses. In addition, deep belief network (DBN) (Bartram and Mahadevan 2014), recurrent neural networks (RNN) (Cha, Choi et al. 2018) and deep neural networks (DNN) (Bao, Chen et al. 2019) are also proposed for structural health monitoring, damage diagnosis and prognosis.

1.3. Research Objectives

The ultimate goal of this research is to develop a holistic learning framework from data collection to decision making, attempting to increase the accuracy of metallic structure damage detection by ultrasonic guided waves. To address the challenges mentioned above, the major objectives of this research are:

- To investigate multiple strategies of SHM using ultrasonic guided wave, obtain more detailed damage information of target structure, and prepare for decision-making.
- To decode the complicated guided wave signals, including complex dispersion and coherent multi-mode interaction. To use machine learning methods to extract more sensitive features, interpret the hidden information in signals, and avoid restraints from independent physical features.
- To consider the real situation of damage interaction, address the challenge of noise interference and high levels of uncertainties, and increase the accuracy of damage prediction.
- To establish a damage detection learning framework based on ultrasonic guided wave and demonstrate the effectiveness of the proposed learning framework under structural uncertainties due to mixed data types, noise levels and material discontinuity.

1.4. Research Significance

Civil engineering structures are the key backbone of the society and economy. Aging issue such as cracking, corrosion, and prestress reduction, manufacturing defects like welding defects, are all potential hazards that metallic structures are prone to during service time. Understanding structural performance, assessing structural condition, and providing real-time decision making are crucial components in structural health monitoring (SHM), in order to avoid catastrophic

events, and improve public safety. Therefore, an efficiency, cost effective and damage sensitive inspection technique is critical important. As compared to conventionally vision-based techniques(Feng and Feng 2016, Pan, Zhang et al. 2019) or vibration-based techniques (Doebling, Farrar et al. 1998, Kong, Cai et al. 2014, Kong, Cai et al. 2017) that are mostly sensitive only to severe damage, guided wave-based techniques are often capable of identifying more minute damage and tiny anomaly in active manner (Mitra and Gopalakrishnan 2016). However, due to intrinsic guided waves propagation and scattering, complex modes generated near the defects and boundaries post great challenges in data classification. Particularly, combined effects introduced from other interferences, including measuring noise and inherent structural uncertainty, hinder the applications of conventional physics-based methods. Thus, machine learning methods, shallow learning algorithms and deep learning algorithms, are employed in this research for better characterization of damage features and improving the robustness of damage detection methods. In addition, this study aims to establish a learning framework for damage diagnosis and prognosis, which consisted of (a) Datasets collected from either experiment or simulation for mechanical damage/defects; (b) Features generated by feature extraction for associated physics-based signal process; (c) Sensitive features through feature selection and related criteria; (d) Prediction formulated by learning model training (e.g., shallow learning or deep learning) for knowledge discovery associated with mechanical damage if actual data are applied.

1.5. Organization of the Dissertation

This dissertation is constructed with eight chapters:

Chapter 1 introduces the background, problem statement, and then presents the research significance and objectives, as well as the organization of this dissertation.

Chapter 2 presents a comprehensive literature review on structural health monitoring by ultrasonic guided waves. Previous research about machine learning methods used in structural health monitoring. In addition, the ultrasonic guided wave propagated in plate structures and cylinder structures is also introduced.

Chapter 3 presents an SVM-based learning framework for damage detection by the ultrasonic guided wave. The datasets were generated by Lamb wave signal through finite element simulation, in which different damage types, severities and orientations were specifically designed for damage detection. Wavelet coefficients and other forms were extracted and evaluated in terms of their damage sensitivity using feature selection criteria. Different noise levels were included to receive signals to simulate structural uncertainty.

Chapter 4 explores the feasibility of CNN models to detect damages in ultrasonic guided wave-based system. The proposed deep learning framework consisted of dataset collected by the simulation and data augmenting method, training CNN and testing, and predicting the testing data formed by the CNN models. Four cases involved in 16 different states were designed in this study, including the damage location, severity, and interaction, attempting to investigate the effect of different damage characteristics on the detecting method. The framework of CNNs, CNN training, and testing was detailed discussed to ensure the effectiveness and accuracy of data classification.

Chapter 5 presents the corrosion detection of metallic structures by ultrasonic guided waves. The deep leaning method was employed to classify the severity of corrosion. Pipes with

and without coating were put into the chamber to accelerate the corrosion. Numerical simulations were established for analysis. Signals collected from simulation were used to train the model, and experiment results were used to test the model.

Chapter 6 presents the prediction of stress level and the rod embedded conditions of prestressed rods in PC structures through the guided waves. The deep learning approach, convolutional neural network (CNN), was used to process the guided wave dataset. A total of fifteen scenarios were designed to address the effectiveness of the stress level prediction under different noise levels and grout materials

Chapter 7 presents the frameworks of machine learning-based damage detection systems with shallow learning and deep learning algorithms respectively. In addition, the deep learning method, a 20-layer residual network (ResNet), was adopted for damage detection and localization in the pipeline with welding part, accelerating the entire processing, and leading to more accurate predictions. Training and validation accuracy curves, loss curves, and confusion metrics were presented to illustrate the performance of the model. Finally, the results were compared with SVM and CNN models obtained high scores in accuracy precision, recall, and F1-score.

Chapter 8 summarizes the primary conclusions and addresses future research directions.

1.6. Reference

Abdeljaber, O., O. Avci, S. Kiranyaz, M. Gabbouj and D. J. Inman (2017). "Real-time vibration-based structural damage detection using one-dimensional convolutional neural networks." *Journal of Sound Vibration* 388: 154-170.

An, Y.-K., K. Jang, B. Kim and S. Cho (2018). "Deep learning-based concrete crack detection using hybrid images". *Sensors and Smart Structures Technologies for Civil, Mechanical, and Aerospace Systems* 2018, International Society for Optics and Photonics.

Azimi, M., A. D. Eslamlou and G. Pekcan (2020). "Data-Driven Structural Health Monitoring and Damage Detection through Deep Learning: State-of-the-Art Review." *Sensors* 20(10): 2778.

Bao, Y., Z. Chen, S. Wei, Y. Xu, Z. Tang and H. Li (2019). "The state of the art of data science and engineering in structural health monitoring." *Engineering* 5(2): 234-242.

Bartram, G. and S. Mahadevan (2014). "Integration of heterogeneous information in SHM models." *Structural Control and Health Monitoring* 21(3): 403-422.

Cha, Y. J., W. Choi and O. Büyüköztürk (2017). "Deep learning‐based crack damage detection using convolutional neural networks." *Computer‐Aided Civil Infrastructure Engineering* 32(5): 361-378.

Cha, Y. J., W. Choi, G. Suh, S. Mahmoudkhani and O. Büyüköztürk (2018). "Autonomous structural visual inspection using region‐based deep learning for detecting multiple damage types." *Computer‐Aided Civil Infrastructure Engineering* 33(9): 731-747.

Dib, G. (2014). "Assessment of ultrasonic guided wave inspection methods for structural health monitoring", *Michigan State University*.

Doebling, S. W., C. R. Farrar and M. B. Prime (1998). "A summary review of vibration-based damage identification methods." *Shock vibration digest* 30(2): 91-105.

Duan, J., T. Shi, H. Zhou, J. Xuan and S. Wang (2020). "A novel ResNet-based model structure and its applications in machine health monitoring." *Journal of Vibration and Control* 1077546320936506.

Farrar, C. R. and K. Worden (2007). "An introduction to structural health monitoring." Philos *Trans A Math Phys Eng*, 365(1851):303-315.

Fawaz, H. I., G. Forestier, J. Weber, L. Idoumghar and P.-A. Muller (2019). "Deep learning for time series classification: a review." *Data Mining and Knowledge Discovery* 33(4): 917-963.

Feng, D. and M. Q. Feng (2016). "Vision‐based multipoint displacement measurement for structural health monitoring." *Structural Control and Health Monitoring* 23(5): 876-890.

Giurgiutiu, V. (2007). "Structural health monitoring: with piezoelectric wafer active sensors", *Elsevier*.

Goyal, D., B. S. Pabla, (2016). "The Vibration Monitoring Methods and Signal Processing Techniques for Structural Health Monitoring: A Review." *Archives of Computational Methods in Engineering* 23(4): 585-594.

Guo, J., X. Xie, R. Bie and L. Sun (2014). "Structural health monitoring by using a sparse coding-based deep learning algorithm with wireless sensor networks." *Personal and ubiquitous computing* 18(8): 1977-1987.

He, Q. P. and J. Wang (2007). "Fault detection using the k-nearest neighbor rule for semiconductor manufacturing processes." *IEEE transactions on semiconductor manufacturing* 20(4): 345-354.

Holnicki-Szulc, J. and C. M. Soares (2004)." Advances in smart technologies in structural engineering", *Springer Science & Business Media*.

Hong, P., G. Gui, Z. Lin and C. Yan (2018). "Deep BBN Learning for Health Assessment toward Decision-Making on Structures under Uncertainties." *KSCE J. Civ. Eng* 22(3): 928-940.

Kong, X., C.-S. Cai and J. Hu (2017). "The state-of-the-art on framework of vibration-based structural damage identification for decision making." *Applied Sciences* 7(5): 497.

Kong, X., C. Cai and B. Kong (2014). "Damage detection based on transmissibility of a vehicle and bridge coupled system." *Journal of engineering mechanics* 141(1): 04014102.

Kralovec, C. and M. Schagerl (2020). "Review of Structural Health Monitoring Methods Regarding a Multi-Sensor Approach for Damage Assessment of Metal and Composite Structures." *Sensors* 20(3): 826.

Lin, Z., H. Pan, X. Wang and M. Li (2018). "Data-Driven structural diagnosis and conditional assessment: from shallow to deep learning". *SPIE Smart Structures and Nondestructive Evaluation*. Denver, CL, USA.

Mitra, M. and S. Gopalakrishnan (2016). "Guided wave based structural health monitoring: A review." *Smart Materials and Structures* 25(5): 053001.

Pan, H., M. Azimi, F. Yan and Z. Lin (2018). "Time-frequency-based data-driven structural diagnosis and damage detection for cable-stayed bridges." *Journal of Bridge Engineering* 23(6): 04018033.

Pan, H., G. Gui, Z. Lin and C. Yan (2018). "Deep BBN learning for health assessment toward decision-making on structures under uncertainties." *KSCE Journal of Civil Engineering* 22(3): 928-940.

Pan, H., Z. Zhang, X. Wang and Z. Lin (2019). "Image-based damage conditional assessment of large-scale infrastructure systems using remote sensing and deep learning approaches". *2019 TechConnect World Innovation Conference*. Boston, MA, USA.

Raghavan, A. (2007). "Guided-wave structural health monitoring". *Doctoral dissertation, University of Michigan.*

Raghavan, A. and C. E. Cesnik (2007). "Guided-wave signal processing using chirplet matching pursuits and mode correlation for structural health monitoring." *Smart Materials Structures* 16(2): 355.

Su, Z. and L. Ye (2004). "Lamb wave-based quantitative identification of delamination in CF/EP composite structures using artificial neural algorithm." *Composite Structures* 66(1-4): 627-637.

Zhang, W., G. Peng, C. Li, Y. Chen and Z. Zhang (2017). "A new deep learning model for fault diagnosis with good anti-noise and domain adaptation ability on raw vibration signals." *Sensors* 17(2): 425.

Zhang, Z., H. Pan and Z. Lin (2019). "Data-Driven Identification for Early-Age Corrosion-Induced Damage in Metallic Structures". *Bridge Engineering Institute Conference 2019 (BEI-2019)*. Honolulu, Hawaii,USA, Bridge Engineering Institute Conference 2019.

Zhang, Z., H. Pan, X. Wang and Z. Lin (2020). "Machine Learning-Enriched Lamb Wave Approaches for Automated Damage Detection." *Sensors* 20(6): 1790.

Zhang, Z., H. Pan, X. Wang and Z. Lin (2021). "Machine learning-enabled Lamb wave approaches for damage detection". *2021 10th International Conference on Structural Health Monitoring of Intelligent Infrastructure*. Porto, Portugal.

Zhang, Z., H. Pan, X. Wang, F. Tang and Z. Lin (2022)." Ultrasonic guided wave approaches for pipeline damage diagnosis based on deep leaning". *ASCE Pipelines 2022 Conference*. Indianapolis, IN, USA.

Zhang, Z., X. Wang, H. Pan and Z. Lin (2019). "Corrosion-induced damage identification in metallic structures using machine learning approaches". *2019 Defense TechConnect Innovation Summit*. National Harbor, Maryland, USA.

Zhao, R., R. Yan, Z. Chen, K. Mao, P. Wang and R. X. Gao (2019). "Deep learning and its applications to machine health monitoring." *Mechanical Systems and Signal Processing* 115: 213-237.

2. LITERATURE REVIEW

In last two decades, structure health monitoring has been widely used for detecting metallic structure damage, assessing the structure conditions and periodical inspection. More techniques are applied for SHM of metallic structures. For instance, Lee and Shinozuka (Lee, Shinozuka et al. 2006) introduced a vision-based displacement sensor system to detect the structural displacement time history. They used a digital video to catch the location change of a high-contrast pattern attached on a bridge. The drawback in this method is difficult to detect minor and inner damage. Meanwhile, Doebling et al. (Doebling, Farrar et al. 1998) and Sohn et al. (Sohn, Farrar et al. 2003) reported reviews on the vibration-based approaches in SHM. Most researchers bonded or embedded vibration-based sensors on structure surface, measured global variations of structures such as frequency, damping ratio, mode shapes, and analyzed these changes to determine the damage state of the structure (Dib 2014). In addition, Bartoli et al. (Ivan Bartoli and Mechanics 2011) employed dynamic identification techniques to investigate the correlation between the PC beam prestressing forces. Their results demonstrated that the vibration frequency could assist in identifying the prestress level. Chen et al. (Chen, Wu et al. 2019) used distributed sensor, long-gauge fiber Bragg grating, to detect the damage of a bridge under stochastic traffic flow. However, these methods are hard to located damage and inefficient for tiny damage. As compared to conventionally vision-based techniques(Feng and Feng 2016, Pan, Zhang et al. 2019) or vibration-based techniques (Doebling, Farrar et al. 1998, Kong, Cai et al. 2014, Kong, Cai et al. 2017) that are mostly sensitive only to severe damage, guided wave-based techniques are often capable of identifying more minute damage and tiny anomaly in active manner(Mitra and Gopalakrishnan 2016).

2.1. Ultrasonic Guided Waves in Structural Health Monitoring

Ultrasonic guided waves, as a nondestructive testing method in SHM systems, have been widely used to evaluate the quality and assessment of metallic structures, such as beams, rods, plates and pipelines, in the past two decades(Alleyne and Cawley 1996, Wang, Peter et al. 2010), owing to the potential of long-distance propagation and sensitivity to mechanical damage.

In plate structure, Lamb waves are more sensitive for damage detection due to the two modes, symmetric mode and antisymmetric mode, allowing them to propagate in thin plate structure with high attenuation ratio. Much research has been conducted on physics-based signal process of Lamb wave for capturing delamination (Saravanos and Heyliger 1995), monitoring fatigue damage and thermal damage in composite structures(Seale, Smith et al. 1998), identifying and locating the damage of metallic structures (Hu, Shimomukai et al. 2008), and improving the effectiveness of the time-reversal damage detection procedure by single-mode (Xu and Giurgiutiu 2007).

For cylinder structures, three modes, including longitudinal, flexural, and torsional modes, are generated when guided wave propagated. For instance, guided waves in torsional mode[9] and longitudinal mode[14] were used for pipe damage detection. Ultrasonic guided waves have been also broadly applied in weldment inspection due to their sensitivity to material discontinuity and structural faults. Ogilvy (Ogilvy 1986) presented a method of ultrasonic ray to trace a butt weld by examining the behavior of waves. David et al.(Alleyne and Cawley 1992) confirmed that the lamb waves through selecting different modes and frequency range provided effective detection of welded steel plates. Arone et al. (Arone, Cerniglia et al. 2006) employed the lamb wave to locate defect and used several parameters to identify and characterize different typologies of defects. Many investigations covered a wide range of applications of ultrasonic guided waves in SHM,

including characterizing mechanical performance of welded structures (Burkov, Eremin et al. 2017), identifying defect of shrink fit welded structures(Lee, Park et al. 2016), quantifying heat affected zone of welded joints (Doerr, Lakocy et al. 2017), and estimating welding quality of spot welding(Hua, Wang et al. 2019).

In addition, the longitudinal modes are the more sensitive for tensile stress and easy to excite by piezoelectric actuators (Sun and Zhu 2020), including use for inspection of steel bar for corrosion, fracture, and stress reduction. Bread et al. (Beard, Lowe et al. 2003) used the pulse-echo technique to detect the corrosion and fracture of grouted tendons anchors and rock bolts by the ultrasonic guided waves. Lanza di Scalea et al. (Lanza di Scalea, Rizzo et al. 2003) applied the guided waves through magnetostrictive transducers to monitor the stress in seven-wire strands. Their results demonstrated the feasibility of determination of prestressing level using the guided wave method. Ervin et al. (Ervin, Kuchma et al. 2009) created an embeddable ultrasonic sensor network to localize and monitor the corrosion of rebar embedded by mortar. They studied the characteristics of guided wave propagated in rebar and the effect forms for corrosion detection, then, showed that the waves were sensitive to corrosion through scattering, mode conversions and reflections. Chaki and Bourse (Chaki and Bourse 2009) detected the stress level of the seven-wire steel strands by ultrasonic guided wave with L (0,1) mode. The typical calibration curves were plotted, which showed the stress level corresponded to the phase velocity change of guided waves. More recently, Treyssède and Laguerre (Treyssede and Laguerre 2010) employed semi-analytical finite element approach to study the guided wave propagation in multi-wire strands. In addition, high order longitudinal modes was indicated to solve the leakage problem of fundamental mode L(0,1) by Dubuc et al. (Dubuc, Ebrahimkhanlou et al. 2018). They used the acoustoelastic theory to propose an approximate theory for predicting the effect of stress on higher mode. Shoji Masanari

(Shoji 2019) employed 60 kHz L (0,1) mode as the guided wave to inspect anchor rods embedded in soil, and unveiled the capability of the ultrasonic guided waves for stress identification in rods.

With the increasing large volumes of data, numerous uncertainties and complex guided wave propagation post great challenges in data process and decision making. Physics-based damage detection and assessment using ultrasonic signals mainly stem from physical features of signals under different domains, such as use of amplitude, correlate coefficient and RMS (Case and Waag 1996, Zhang and Chen 2017). Wavelet transform is also a common method for extracting features from signals (Drai, Khelil et al. 2002, Lee and Estivill-Castro 2007). Due to intrinsic guided waves propagation and scattering, complex modes generated near defects post great challenges in data classification. Particularly, combined effects introduced from other interferences, including measuring noise, inherent structural uncertainty, and signal attenuation, hinder the applications of conventional physics-based methods.

2.2. Ultrasonic Guided Wave Propagation in Plate Structures

Guided waves display in different forms, such as axial wave, flexural wave, shear wave, Rayleigh wave and Lamb wave. Among them Lamb waves exhibit their merits over other types for damage detection and classification, due to their strong penetration that can allow them to propagate in thin plate structure with high attenuation ratio. Particularly, their two modes, symmetric mode and antisymmetric mode, could transfer to other types (Ahmed 2014). for instance, some researchers (Mitra and Gopalakrishnan 2016) found that at low frequency, the symmetric Lamb wave had a similar with axial waves, while the anti-symmetric Lamb wave was identical to flexural waves. When at high frequency, the speed of Lamb wave can be converged as Rayleigh waves.

Lamb-wave based damage detection is a non-destructive strategy by identifying change of the wave form when the excited Lamb-wave signals encounter damage or other material discontinuity and quantifying their location and severity of the damage. Lamb wave excited in thin plate exhibits in different modes, symmetric mode (labelled as *S* mode) and anti-symmetric mode (labelled as *A* mode), while each one has its own application for different types of damage (Su and Ye 2009). For instance, S_0 mode is sensitively for internal damages in thin plate-like structure, while A_0 mode is sensitively for surface damages (Ahmed 2014). Particularly, these two modes could carry more energy than others. The Lamb wave in a thin plate can be expressed as (Achenbach 2012)

$$\frac{\tan(q*h)}{\tan(p*h)} = \frac{-4k^2pq}{(q^2-k^2)^2} \quad (S \text{ mode}) \tag{1}$$

$$\frac{\tan(q*h)}{\tan(p*h)} = \frac{(q^2-k^2)^2}{-4k^2pq} \quad (A \text{ mode}) \tag{2}$$

$$p^2 = \frac{\omega^2}{C_L^2} - k^2 \tag{3}$$

$$q^2 = \frac{\omega^2}{C_S^2} - k^2 \tag{4}$$

$$\omega = 2\pi f \tag{5}$$

where k is wavenumber, f is frequency and h represent the thickness. The Lamb wave speed is given by $c_p = \frac{\omega}{k}$, which is the velocity of individual waves.

C_L and C_S are the longitudinal and transverse waves, by the form:

$$C_L = \sqrt{\frac{\lambda+2*\mu}{\rho}} \tag{6}$$

$$C_S = \sqrt{\frac{\mu}{\rho}} \tag{7}$$

$$\lambda = \frac{\nu E}{(1-2\nu)(1+\nu)} \tag{8}$$

$$\mu = \frac{E}{2(1+\nu)} \tag{9}$$

where ρ is the mass density, E is the Young's modulus and ν is the Poisson's ratio.

Group velocity, C_g, is the propagation speed of wave energy, as shown below:

$$C_g = \frac{d\omega}{dk} \tag{10}$$

Substituting $k=\omega/C_p$ and $\omega=2\pi f$ in Eqn. (10) yields:

$$C_g = C_p^2[C_p - fd\frac{d(C_p)}{d(fd)}]^{-1} \tag{11}$$

where fd denotes frequency time thick. As such, Lamb wave phase velocities and group velocities of an aluminum plate are shown in Figure 1(a) and (b), in which the modes increase with the increase of the higher frequency range.

Pulse-echo method is one way to excite a Lamb wave, where two actuators are usually mounted at the same side of the plate for signal transmitting and receiving in process(Yang, Qiao et al. 2005). One is for the transmitter and the other services as receiver, as pulse-echo configuration. In this configuration, the signal is reflected when it reaches the boundary or damage of the plate, then, this echoed signal is captured by the receiver.

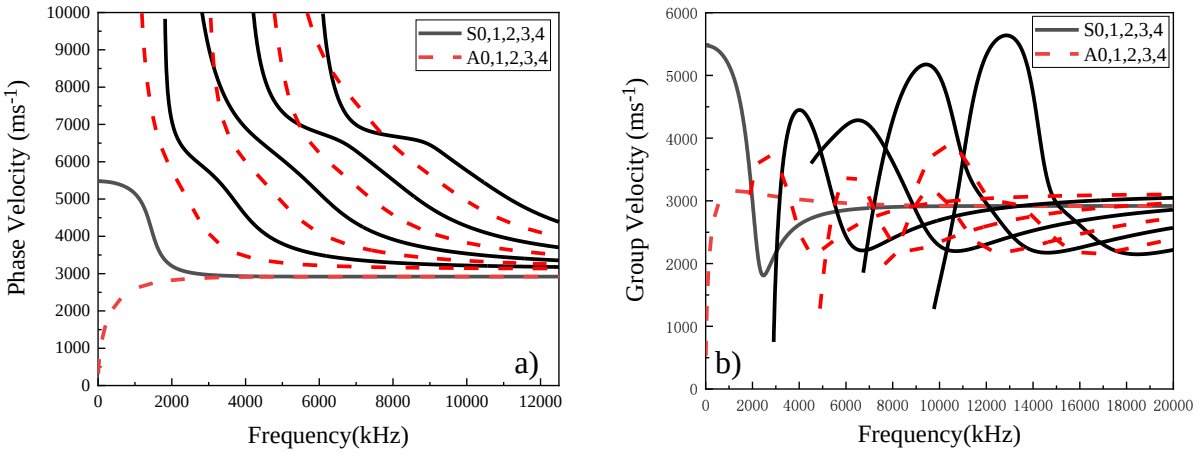

Figure 1. Dispersion curves. (a) phase velocity and (b) group velocity.

2.3. Ultrasonic Guided Wave Propagation in Cylindrical Structure

Guided waves introduced in cylinder structures were stated in 19th century (Chree 1889). Yang and Zhang represented the wave solution when propagated in the isotropic and elastic material. The governing equation of wave propagating in isotropic cylinders was expressed as (Raghavan and Cesnik 2007)

$$(\lambda + 2\mu)\nabla(\nabla * \boldsymbol{u}) + \mu\nabla^2\boldsymbol{u} + \boldsymbol{f} = \boldsymbol{\rho}\left(\frac{\partial^2\boldsymbol{u}}{\partial x^2}\right) \tag{12}$$

where $\boldsymbol{u}$ represents the displacement vector; x is the time; ∇^2 is the three-dimensional Laplace operator; λ and μ indicate the Lame's constants; $\boldsymbol{\rho}$ is the mass density; and the body force $\boldsymbol{f}$ is equal to 0. Then, Helmholtz decomposition was used in the Equation (1) to simplify the problem as

$$\boldsymbol{u} = \nabla\varphi + \nabla * \mathbf{H} \tag{13}$$

$$\nabla * \mathbf{H} = 0 \tag{14}$$

Where φ and $\mathbf{H}$ represent the scalar and vector potentials. Substitution of equation (1) and (2),

$$\nabla\left[(\lambda + 2\mu)\nabla^2\varphi - \boldsymbol{\rho}\left(\frac{\partial^2\varphi}{\partial x^2}\right)\right] + \nabla\left[\mu\nabla^2\mathbf{H} - \boldsymbol{\rho}\left(\frac{\partial^2\mathbf{H}}{\partial x^2}\right)\right] = 0 \tag{15}$$

To satisfy the equation (4), the following resulting equations are

$$\frac{(\lambda + 2\mu)}{\boldsymbol{\rho}}\nabla^2\varphi = \frac{\partial^2\varphi}{\partial x^2} \tag{16}$$

$$\frac{\mu}{\boldsymbol{\rho}}\nabla^2\mathbf{H} = \frac{\partial^2\mathbf{H}}{\partial x^2} \tag{17}$$

The velocities of longitudinal and shear waves can be expressed as (Løvstad 2012)

$$c_l = \sqrt{\frac{(\lambda + 2\mu)}{\boldsymbol{\rho}}} \tag{18}$$

$$c_s = \sqrt{\frac{\mu}{\boldsymbol{\rho}}} \tag{19}$$

Equations (5) and (6) represented that the longitudinal waves and shear waves independently propagated in the field. The solutions (Lowe 1995) of them are listed as

$$\boldsymbol{\varphi} = A_l e^{i(\boldsymbol{k}_l * \boldsymbol{r} - \omega x)} \tag{20}$$

$$\mathbf{H} = A_s e^{i(\boldsymbol{k}_s * \boldsymbol{r} - \omega x)} \tag{21}$$

where A_l and A_s are the amplitudes at direction **r**, and $\boldsymbol{k}_l$ and $\boldsymbol{k}_s$ are the wave number vectors, ω is the wave frequency.

Three types of guided wave were generated when waves propagation in a cylindrical structure, including longitudinal mode (L (0, m)), torsional mode (T (0, m)) and flexural mode (F (n, m)). In the modes, n and m are present the circumferential order and modulus. When n = 0, the waves are symmetrical, such as L (0, m) and T (0, m). Otherwise, the waves are asymmetrical. The dispersion relation for cylindrical rod were derived by Pochhammer and Chree. The wave equations corresponding with the frequency are expressed as (Rose 2014)

$$\frac{2\alpha}{r}(\beta^2 + k^2)J_1(\alpha r)J_1(\beta r) - (\beta^2 - k^2)J_0(\alpha r)J_1(\beta r) - 4k^2\alpha\beta J_0(\beta r) = 0 \tag{22}$$

$$k = \frac{\omega}{c} \tag{23}$$

$$\alpha = \frac{\omega^2}{C_l^2} - k^2 \tag{24}$$

$$\beta = \frac{\omega^2}{C_s^2} - k^2 \tag{25}$$

where r is the radius; ω is the circular frequency and c is the phase velocity; J_0 and J_1 are Bessel's function with the parameter α and β.

The stress affects the phase velocity of the guided wave. The change of the phase velocity ΔC is expressed as

$$\Delta C = -\left[\frac{(C^0)^2}{l}\right]\Delta t \tag{26}$$

where C^0 is the unstressed velocity; l represents the length of wave propagation in stress area; Δt is the time change.

The phase velocity and Group velocity were shown in Figure 2, which was calculated by matlab PCDisp (Seco, Martín et al. 2002, Seco and Jiménez 2012). To reduce the dispersion of the guided wave, the frequency of the excitation wave was lower than 50 kHz.

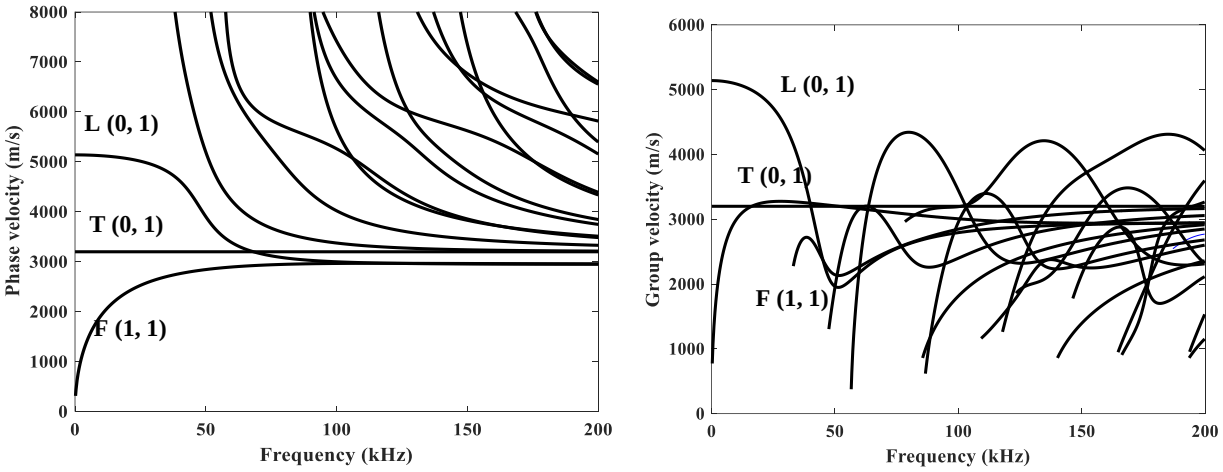

Figure 2. Phase velocities and group velocities.

2.4. Machine Learning Methods in Structural Health Monitoring

Artificial intelligence (AI) and machine learning methods (Pan, Gui et al. 2018, Nair, Cai et al. 2019, Zhang, Pan et al. 2019, Zhang, Wang et al. 2019) become an emerging strategy in recent years to solve complex data fusion and information extraction, thereby offering automated ultrasonic signal feature selection of interest and enhanced accurate predictions. Literature review demonstrated that a few studied attempted to deploy the capability of machine learning for enhancing lamb wave-based damage detection. For instance, matching pursuit algorithms were

introduced into this area by Wang (Wang, Bao et al. 2018), who designed a comprehensive dictionary to identify the location of damage. Yang and He (Yang, He et al. 2016) employed Bayesian method to achieve crack size predictions accurately. Legendre et al. (Legendre, Massicotte et al. 2001) presented an automated system to classify the metallic welds based on wavelet transform of Lamb wave by a neural network. Su et al. (Su and Ye 2004) used an artificial neural network (ANN) to establish a Lamb wave propagation based quantitative identification shame for delamination in composite structures. Das et al. (Das, Chattopadhyay et al. 2010) used one-class support vector machine (SVM) technique to demonstrate damage classification. This method also demonstrated better classification in the presence of material and experimental uncertainties. Sun et al. (Sun, Wang et al. 2017) employed a Lamb wave damage quantification method using least square support vector machine (LS-SVM) and genetic algorithm (GA). Three sensitive features were extracted from Lamb wave signal, normalized amplitude, phase change, and correlation coefficient. GA was used for obtaining the optimal model parameters. Hossein et al. (HosseinAbadi, Amirfattahi et al. 2014) applied multiclass SVM classified the damage and estimated the severity of damages. Kim et al. employed wavelet-based autoregressive model to estimate the structure responses and used SVM to distinguish the damaged or undamaged state of the structure (Kim, Chong et al. 2012). With the development of machine learning algorithms, deep learning methods, as a breakthrough, were achieved impressive results. Recent studies demonstrated that deep learning algorithms could deploy their advantages in several challenging tasks in SHM. Specifically, convolutional neural networks (CNNs) with different architectures were utilized for corrosion assessment on metallic surfaces outperformed the previous detection approaches (Atha and Jahanshahi 2018), crack damage detection of concrete structures getting consistent high performance under realistic situations (Cha, Choi et al. 2017), measuring

compressed response data (Azimi and Pekcan 2020)and developing data-driven surrogate model to predict building's seismic responses (Zhang, Liu et al. 2020). Alternatively, several deep learning algorithms were proposed in these areas, such as deep belief network (DBN) (Bartram and Mahadevan 2014), recurrent neural networks (RNN) (Cha, Choi et al. 2018) and deep neural networks (DNN) (Bao, Chen et al. 2019). From shallow learning to deep learning, machine learning methods aim to decode the data and find the relationships by increasing the analysis layer. In 2015, He et al. proposed residual networks (ResNet) achieved high accuracy in image recognition and object detection (He, Zhang et al. 2016). Following, ResNet was applied for time series classification (Wu, Zhang et al. 2019) , visual recognition (Wu, Shen et al. 2019) and fault diagnosis (Wen, Li et al. 2019), which achieved high accuracy performance in different areas.

2.5. Summary

In this section, previous research for ultrasonic guided waves in structural health monitoring has been reviewed. As a nondestructive testing method, ultrasonic guided waves achieved success in detecting and locating damage. However, there are still several challenges to overcome due to the damage interaction, the complexity of wave scattering and multiple uncertainties during the inspection.

Therefore, the following chapters aim to propose machine learning-empowered methods for structural health monitoring, damage diagnosis and prognosis. A learning framework is established from datasets collection, feature extraction to prediction by learning model. Several cases of metallic structures (from one-dimensional plated and rods to three-dimensional pipes) are deliberately selected to demonstrate the potential real-world applications. Mechanical damage and aging defects, which are commonly appeared during service live, are considered in this study, such as cracks, welding defects, corrosion, and stress reduction. Multiple strategies are involved to

estimate damage locations, types, severities, and orientations. In addition, complex interconnected information among data, models, uncertainty, and risk for enhanced structural diagnosis and prognosis are considered to improve metallic structural integrity and safety.

Additionally, AI approaches are involved to interpret hidden information from signal. Three different levels of the AI/ML approaches, from shallow learning to deep learning, are used to explore the effectiveness of the data fusion and data representation for damage diagnosis and prognosis. Meanwhile, noise interference and structurally initial nonlinearity as typical structural uncertainty are included in data collection to understand the effects of data quality and uncertainty on the robustness of the proposed methods.

2.6. Reference

Achenbach, J. (2012)." Wave propagation in elastic solids", *Elsevier*.

Ahmed, M. N. (2014). "A study of guided ultrasonic wave propagation characteristics in thin aluminum plate for damage detection", *University of Toledo*.

Alleyne, D. and P. C. Cawley (1996). "The excitation of Lamb waves in pipes using dry-coupled piezoelectric transducers." *Journal of Nondestructive Evaluation* 15(1): 11-20.

Alleyne, D. N. and P. Cawley (1992). "Optimization of Lamb wave inspection techniques." *NDT & E International* 25(1): 11-22.

Arone, M., D. Cerniglia and V. Nigrelli (2006). "Defect characterization in Al welded joints by non-contact Lamb wave technique." *Journal of Materials Processing Technology* 176(1-3): 95-101.

Atha, D. J. and M. R. Jahanshahi (2018). "Evaluation of deep learning approaches based on convolutional neural networks for corrosion detection." *Structural Health Monitoring* 17(5): 1110-1128.

Azimi, M. and G. Pekcan (2020). "Structural health monitoring using extremely compressed data through deep learning." *Computer‐Aided Civil and Infrastructure Engineering* 35(6): 597-614.

Bao, Y., Z. Chen, S. Wei, Y. Xu, Z. Tang and H. Li (2019). "The state of the art of data science and engineering in structural health monitoring." *Engineering* 5(2): 234-242.

Bartram, G. and S. Mahadevan (2014). "Integration of heterogeneous information in SHM models." *Structural Control and Health Monitoring* 21(3): 403-422.

Beard, M., M. Lowe and P. Cawley (2003). "Ultrasonic guided waves for inspection of grouted tendons and bolts." *Journal of Materials in Civil Engineering* 15(3): 212-218.

Burkov, M., A. Eremin, P. Lyubutin, A. Byakov and S. Panin (2017). "Applying an Ultrasonic Lamb Wave Based Rechnique to Testing the Condition of V96ts3T12 Aluminum Alloy." *Russian Journal of Nondestructive Testing* 53(12): 817-829.

Case, T. J. and R. C. Waag (1996). "Flaw identification from time and frequency features of ultrasonic waveforms." *IEEE transactions on ultrasonics, ferroelectrics, and frequency control* 43(4): 592-600.

Cha, Y. J., W. Choi and O. Büyüköztürk (2017). "Deep learning‐based crack damage detection using convolutional neural networks." *Computer‐Aided Civil Infrastructure Engineering* 32(5): 361-378.

Cha, Y. J., W. Choi, G. Suh, S. Mahmoudkhani and O. Büyüköztürk (2018). "Autonomous structural visual inspection using region‐based deep learning for detecting multiple damage types." *Computer‐Aided Civil Infrastructure Engineering* 33(9): 731-747.

Chaki, S. and G. Bourse (2009). "Guided ultrasonic waves for non-destructive monitoring of the stress levels in prestressed steel strands." *Ultrasonics* 49(2): 162-171.

Chen, S. Z., G. Wu and D. C. Feng (2019). "Damage detection of highway bridges based on long-gauge strain response under stochastic traffic flow." *Mechanical Systems and Signal Processing* 127: 551-572.

Chree, C. (1889). "The equations of an isotropic elastic solid in polar and cylindrical co-ordinates their solution and application." *TCaPS* 14: 250.

Das, S., A. Chattopadhyay and A. N. Srivastava (2010). "Classifying induced damage in composite plates using one-class support vector machines." *Aiaa Journal* 48(4): 705-718.

Dib, G. (2014). "Assessment of ultrasonic guided wave inspection methods for structural health monitoring", *Michigan State University*.

Doebling, S. W., C. R. Farrar and M. B. Prime (1998). "A summary review of vibration-based damage identification methods." *Shock vibration digest* 30(2): 91-105.

Doerr, C., A. Lakocy, J.-Y. Kim, P. M. Singh, J. J. Wall, J. Qu and L. J. Jacobs (2017). "Evaluation of the heat-affected zone (HAZ) of a weld joint using nonlinear Rayleigh waves." *Materials Letters* 190: 221-224.

Drai, R., M. Khelil and A. Benchaala (2002). "Time frequency and wavelet transform applied to selected problems in ultrasonics NDE." *NDT & e International* 35(8): 567-572.

Dubuc, B., A. Ebrahimkhanlou and S. Salamone (2018). "Higher order longitudinal guided wave modes in axially stressed seven-wire strands." *Ultrasonics* 84: 382-391.

Ervin, B. L., D. A. Kuchma, J. T. Bernhard and H. Reis (2009). "Monitoring corrosion of rebar embedded in mortar using high-frequency guided ultrasonic waves." *Journal of engineering mechanics* 135(1): 9-19.

Feng, D. and M. Q. Feng (2016). "Vision‐based multipoint displacement measurement for structural health monitoring." *Structural Control and Health Monitoring* 23(5): 876-890.

He, K., X. Zhang, S. Ren and J. Sun (2016). "Deep residual learning for image recognition". *Proceedings of the IEEE conference on computer vision and pattern recognition*.

HosseinAbadi, H. Z., R. Amirfattahi, B. Nazari, H. R. Mirdamadi and S. A. Atashipour (2014). "GUW-based structural damage detection using WPT statistical features and multiclass SVM." *Applied Acoustics* 86: 59-70.

Hu, N., T. Shimomukai, H. Fukunaga and Z. Su (2008). "Damage identification of metallic structures using A0 mode of Lamb waves." *Structural Health Monitoring* 7(3): 271-285.

Hua, L., B. Wang, X. Wang, X. He and S. Guan (2019). "In-situ ultrasonic detection of resistance spot welding quality using embedded probe." *Journal of Materials Processing Technology* 267: 205-214.

Ivan Bartoli, S. S., Robert Phillips, S.M.ASCE, Francesco Lanza di Scalea, and C. S. S. J. J. o. E. Mechanics (2011). "Use of Interwire Ultrasonic Leakage to Quantify Loss of Prestress in Multiwire Tendons." 137(5): 324-333.

Kim, Y., J. W. Chong, K. H. Chon and J. Kim (2012). "Wavelet-based AR–SVM for health monitoring of smart structures." *Smart Materials and Structures* 22(1): 015003.

Kong, X., C.-S. Cai and J. Hu (2017). "The state-of-the-art on framework of vibration-based structural damage identification for decision making." *Applied Sciences* 7(5): 497.

Kong, X., C. Cai and B. Kong (2014). "Damage detection based on transmissibility of a vehicle and bridge coupled system." *Journal of engineering mechanics* 141(1): 04014102.

Lanza di Scalea, F., P. Rizzo and F. Seible (2003). "Stress measurement and defect detection in steel strands by guided stress waves." *Journal of Materials in Civil Engineering* 15(3): 219-227.

Lee, J., J. Park and Y. Cho (2016). "A novel ultrasonic NDE for shrink fit welded structures using interface waves." *Ultrasonics* 68: 1-7.

Lee, J. J., M. J. N. Shinozuka and E. International (2006). "A vision-based system for remote sensing of bridge displacement." 39(5): 425-431.

Lee, K. and V. Estivill-Castro (2007). "Feature extraction and gating techniques for ultrasonic shaft signal classification." *Applied Soft Computing* 7(1): 156-165.

Legendre, S., D. Massicotte, J. Goyette and T. K. Bose (2001). "Neural classification of Lamb wave ultrasonic weld testing signals using wavelet coefficients." *IEEE Transactions on Instrumentation and Measurement* 50(3): 672-678.

Løvstad, A. (2012). "Detection of localised corrosion in pipes using guided waves." *Materials Science*

Lowe, M. J. (1995). "Matrix techniques for modeling ultrasonic waves in multilayered media." *IEEE transactions on ultrasonics, ferroelectrics, and frequency control* 42(4): 525-542.

Mitra, M. and S. Gopalakrishnan (2016). "Guided wave based structural health monitoring: A review." *Smart Materials and Structures* 25(5): 053001.

Nair, A., C. Cai and X. Kong (2019). "Acoustic emission pattern recognition in CFRP retrofitted RC beams for failure mode identification." *Composites Part B: Engineering* 161: 691-701.

Ogilvy, J. A. (1986). "Ultrasonic beam profiles and beam propagation in an austenitic weld using a theoretical ray tracing model." *Ultrasonics* 24(6): 337-347.

Pan, H., G. Gui, Z. Lin and C. Yan (2018). "Deep BBN learning for health assessment toward decision-making on structures under uncertainties." *KSCE Journal of Civil Engineering* 22(3): 928-940.

Pan, H., Z. Zhang, X. Wang and Z. Lin (2019). Image-based damage conditional assessment of large-scale infrastructure systems using remote sensing and deep learning approaches. *2019 TechConnect World Innovation Conference*. Boston, MA, USA.

Raghavan, A. and C. E. Cesnik (2007). "3-D elasticity-based modeling of anisotropic piezocomposite transducers for guided wave structural health monitoring." *Journal of Vibration and Acoustics* 129(6):739-751.

Rose, J. L. (2014). "Ultrasonic guided waves in solid media", *Cambridge university press.*

Saravanos, D. A. and P. R. Heyliger (1995). "Coupled layerwise analysis of composite beams with embedded piezoelectric sensors and actuators." *Journal of Intelligent Material Systems and Structures* 6(3): 350-363.

Seale, M. D., B. T. Smith and W. Prosser (1998). "Lamb wave assessment of fatigue and thermal damage in composites." *The Journal of the Acoustical Society of America* 103(5): 2416-2424.

Seco, F. and A. R. Jiménez (2012). "Modelling the generation and propagation of ultrasonic signals in cylindrical waveguides." *Ultrasonic waves*: 1-28.

Seco, F., J. M. Martín, A. Jiménez, J. L. Pons, L. Calderón and R. Ceres (2002). "*PCDISP:* a tool for the simulation of wave propagation in cylindrical waveguides". 9*th International Congress on Sound and Vibration*.

Shoji, M. (2019). "Ultrasonic Guided Wave Inspection of Anchor Rods Embedded in Soil." *Journal of Nondestructive Evaluation* 38(4): 96.

Sohn, H., C. R. Farrar, F. M. Hemez, D. D. Shunk, D. W. Stinemates, B. R. Nadler and J. J. Czarnecki, USA (2004). "A review of structural health monitoring literature: 1996–2001." *Technical report LA-13976_MS, NM, USA: Los Alamos National Laboratory*.

Su, Z. and L. Ye (2004). "Lamb wave-based quantitative identification of delamination in CF/EP composite structures using artificial neural algorithm." *Composite Structures* 66(1-4): 627-637.

Su, Z. and L. Ye (2009). *Identification of damage using Lamb waves: from fundamentals to applications*, Springer Science & Business Media.

Sun, F., N. Wang, J. He, X. Guan and J. Yang (2017). "Lamb wave damage quantification using GA-based LS-SVM." *Materials* 10(6): 648.

Sun, H. and J. Zhu (2020). "Nondestructive evaluation of steel-concrete composite structure using high-frequency ultrasonic guided wave." *Ultrasonics* 103: 106096.

Treyssede, F. and L. Laguerre (2010). "Investigation of elastic modes propagating in multi-wire helical waveguides." *Journal of sound and vibration* 329(10): 1702-1716.

Wang, W., Y. Bao, W. Zhou and H. Li (2018). "Sparse representation for Lamb-wave-based damage detection using a dictionary algorithm." *Ultrasonics* 87: 48-58.

Wang, X., W. T. Peter, C. K. Mechefske and M. Hua (2010). "Experimental investigation of reflection in guided wave-based inspection for the characterization of pipeline defects." *NDT & e International* 43(4): 365-374.

Wen, L., X. Li and L. Gao (2019). "A transfer convolutional neural network for fault diagnosis based on ResNet-50." *Neural Computing and Applications*: 1-14.

Wu, J., Z. Zhang, Y. Ji, S. Li and L. Lin (2019). *A ResNet with GA-based Structure Optimization for Robust Time Series Classification*. 2019 IEEE International Conference on Smart Manufacturing, Industrial & Logistics Engineering (SMILE), IEEE.

Wu, Z., C. Shen and A. Van Den Hengel (2019). "Wider or deeper: Revisiting the resnet model for visual recognition." *Pattern Recognition* 90: 119-133.

Xu, B. and V. Giurgiutiu (2007). "Single mode tuning effects on Lamb wave time reversal with piezoelectric wafer active sensors for structural health monitoring." *Journal of Nondestructive Evaluation* 26(2-4): 123-134.

Yang, J., J. He, X. Guan, D. Wang, H. Chen, W. Zhang, Y. Liu (2016). "A probabilistic crack size quantification method using in-situ Lamb wave test and Bayesian updating." *Mechanical Systems and Signal Processing* 78: 118-133.

Yang, M., P. J. S. m. Qiao and structures (2005). "Modeling and experimental detection of damage in various materials using the pulse-echo method and piezoelectric sensors/actuators." *Smart Materials and Structures* 14(6): 1083.

Zhang, R., Y. Liu and H. Sun (2020). "Physics-guided convolutional neural network (PhyCNN) for data-driven seismic response modeling." *Engineering Structures* 215: 110704.

Zhang, Z. and S. Chen (2017). "Real-time seam penetration identification in arc welding based on fusion of sound, voltage and spectrum signals." *Journal of Intelligent Manufacturing* 28(1): 207-218.

Zhang, Z., H. Pan and Z. Lin (2019). Data-Driven Identification for Early-Age Corrosion-Induced Damage in Metallic Structures. *Bridge Engineering Institute Conference 2019 (BEI-2019)*. Honolulu, Hawaii,USA, Bridge Engineering Institute Conference 2019.

Zhang, Z., X. Wang, H. Pan and Z. Lin (2019). Corrosion-induced damage identification in metallic structures using machine learning approaches. *2019 Defense TechConnect Innovation Summit*. National Harbor, Maryland, USA.

3. SVM BASED ULTRASONIC GUIDED WAVE APPROACHES FOR AUTOMATED DAMAGE DETECTION

3.1. Introduction

Lamb wave approaches have been accepted as efficiently non-destructive evaluations in structural health monitoring for identifying damage in different states. Despite significant efforts in signal process of Lamb waves, physics-based prediction is still a big challenge due to complexity nature of the Lamb wave when it propagates, scatters and disperses. Machine learning in recent years has created transformative opportunities for accelerating knowledge discovery and accurately disseminating information where conventional Lamb wave approaches cannot work. Therefore, the learning framework was proposed with a workflow from dataset generation, to sensitive feature extraction, to prediction model for lamb-wave-based damage detection. A total of 17 damage states in terms of different damage type, sizes and orientations were designed to train the feature extraction and sensitive feature selection. Machine learning method, support vector machine (SVM), was employed for learning model. Grid searching (GS) technique was adopted to optimize the parameters of SVM model. The results show that the machine learning-enriched Lamb wave-based damage detection method is an efficient and accuracy wave to identify the damage severity and orientation. Results demonstrated that different features generated from different domains had certain levels of sensitivity to damage, while the feature selection method revealed that time-frequency features and wavelet coefficients exhibited the highest damage-sensitivity. These features were also much more robust to noise. With increase of noise, the accuracy of the classification dramatically dropped.

3.2. Machine Learning Enriched Lamb Wave Approaches

This section aimed to propose machine-learning-enriched methods for damage detection. As illustrated in Figure *3*, the learning framework consisted of (a) Datasets collected from either experiment or simulation for mechanical damage/defects; (b) Features generated by feature extraction for associated physics-based signal process; (c) Sensitive features through feature selection and related criteria; (d) Prediction formulated by learning model training (e.g., shallow learning or deep learning) for knowledge discovery associated with mechanical damage if actual data are applied.

This learning framework provided a workflow from data to sensitive feature extraction. Although large datasets from different sources could enrich the extraction of representation, simulation using Lamb wave excitation was selected herein as demonstration to generate data. Accordingly, different signal process under frequency or time domains could be selected to filter data and extract features that could represent the hidden information associated with mechanical damage. To apply damage-sensitive features for data training, feature selection and criteria were determined in this study, while SVM learning algorithms were designed for learning model training, where the radial basis function (RBF) kernel was herein chosen as the kernel function, as presented in detail in the following sections. Note that deep learning algorithms, such as convolutional neural networks (CNN) or deep belief network, are powerful for automated feature extraction. Such functionality in the deep learning requires less or even no physics meaning during the feature extraction and feature selection, while one of the objectives in this study was to gain understanding of selective features provided in the shallow learning. Thus, the deep learning was not selected herein for such consideration.

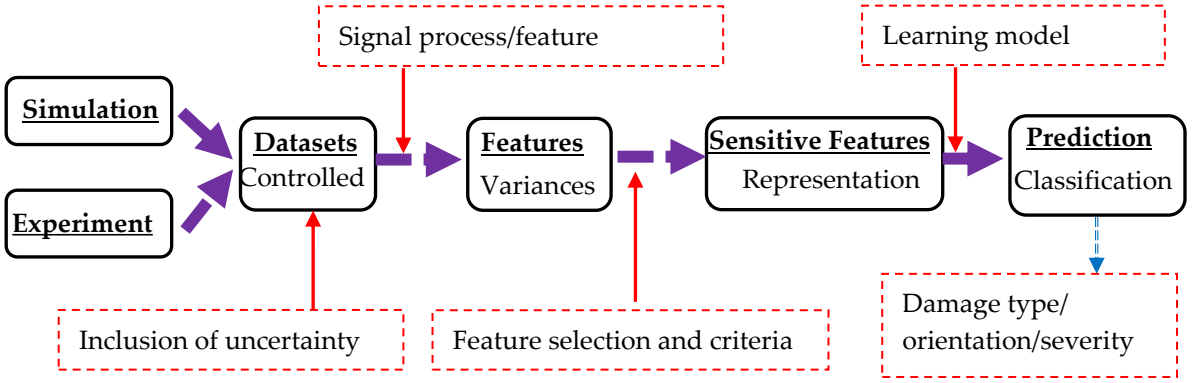

Figure 3. Framework of machine learning-enriched method for damage detection.

To achieve that, Section 3.3 was to present Lamb-wave based damage detection in detail, including brief summary of signal process by basic lamb wave theory and simulation, while test scenarios were designed to account for different damage type, damage level, damage orientation. Section 3.4 discussed feature extraction methods using signal characteristics under time and frequency domains, while sensitive features to defects were extracted using feature selection methods for better data classification. The merits of using the proposed machine-learning-enriched methods over conventional physics-based signal process were mainly on:

(a) Handling nonlinear and high-dimensional features; physics-based features such as amplitude, phase change, and correlation coefficient, which are often used explicitly for determining damage level and size, could be insensitive to defects in some cases when facing with complexity of Lamb wave multimodal interaction, noise or other interference. Differently, feature extraction and feature selection in the machine learning could effectively extract sensitive features for damage detection, with less physical representation, as discussed in Section 3.4;

(b) Tackling more structural complexity with less physical restraints; As stated in Section 3, Lamb wave exhibits non-stationary and nonlinear behavior, experiencing complex dispersion and coherent multi-mode interaction. Different to physics-based methods that attempt decomposition of mixed modes for signal process, such as using the first symmetric mode (S0) or

anti-symmetric mode (A0), the machine learning could extract sensitive damage features, with less or without such physical restraints. As a result, with representative data, the machine learning could provide better damage detection with minimized explicit formation that physics-based methods highly rely on.

(c) Uncovering structural uncertainty; Consider that engineering structures are often exposed to high levels of uncertainty, structural uncertainty is one of challenges for physics-based methods in SHM. The cases were designed in section 3.5 to address this challenge and demonstrate the effectiveness of the proposed learning framework under structural uncertainty due to mixed data types, noise level and material discontinuity from weldment. The findings were expected to provide new vision using machine learning methods for engineering applications.

3.3. Numerical Simulation and Data Generation

3.3.1. Simulation of Lamb Wave Excitation Along Metal Structures

Lamb wave propagates in the plate as a pattern illustrated in Figure 1, while different damage location and severity could cause the wave scattering in the form of mode conversion, as well as reflection and transmission. As a result, linking the changes of the wave modes with associated damage types, localization and severity make it flexible for damage identification. Much research (Farrar and Worden 2007, Ahmed and Gradworks 2014) has demonstrated that Lamb wave is highly sensitive to relatively tiny damage, which is often failed by other non-destructive detection methods. Also, the Lamb wave is robust since it can propagate to a large distance with little attenuation. In the context of the phase velocity of the Lamb wave, more wave modes are involved when the frequency of the wave is higher, which could lead to more complicatedly interacted modes. To make signal more sensitive to damage, the frequency of the Lamb wave used in the excitation should be limited at the lower level (less than 1000 kHz) (Farrar

and Worden 2007, Farrar and Worden 2007, Ahmed and Gradworks 2014), which in turn leads to remaining the lowest modes, S0 and A0.

As such, the commercially available finite element software, COMSOL®, was used in this study. As shown in Figure 4, the excitation signal with 100 kHz, D(t), was defined by a 5-cycle sine function operated with a hanning window by the form:

$$D(t) = A(1 - cos\frac{2\pi f_c t}{n})\sin(2\pi f_c t) \quad (27)$$

where A is amplitude of the signal, fc is the frequency, and n is the number of the period. The signal was defined in COMSOL to simulate the effect of the actuator, while the displacement was set with opposite orientation at the ends of the piezo actuator.

3.3.2. Calibration of Simulation

This section was to calibrate the parameter used for modeling and characterizing Lamb wave propagation along a structure. A prototype of a thin narrow-strip aluminum beam was selected from the literature work by V.Giurgiutiu (Giurgiutiu, Bao et al. 2003). The plate had a dimension of 914 mm by 14 mm with a thickness of 1.6 mm. The piezo actuator was installed in front of the beam, as shown Figure 5. Five different spots, A to E, were selected to receive the signal, as shown in Figure 5. The damage was located at the point C (457mm away from left side) of the plate. An 8-mm through-the-thickness notch was defined in the COMSOL to simulate the shape of the damage.

Free triangular elements available in COMSOL were used to mesh the aluminum plate. The maximum size of each element was 4.937 mm, and the minimum size was 2.468 mm. Boundary conditions were given as free.

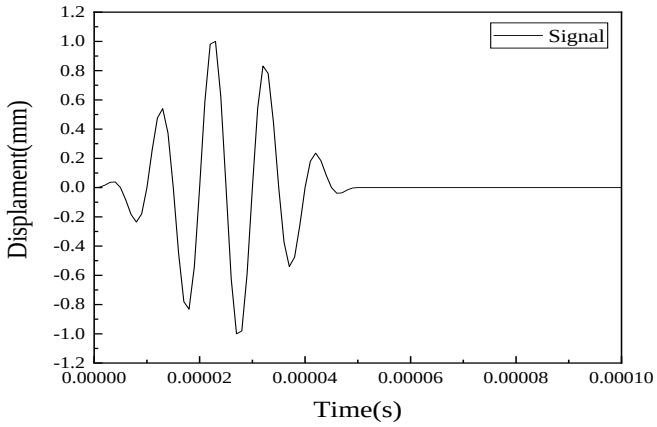

Figure 4. Excited Lamb wave in the simulation.

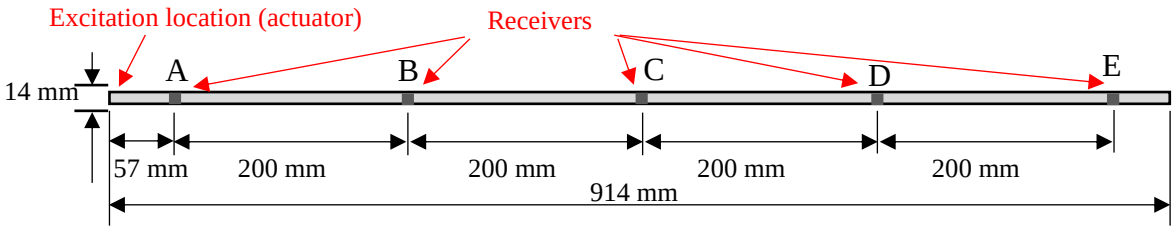

Figure 5. Aluminum beam.

The results were plotted in Figure 6 to display Lamb wave propagating through the plate under damage state. It gives a detail about the wave propagating in different period. The excitation was sent into the plate at left side and then the wave propagated to both sides. The wave returned when it arrived at the left boundary. At the other side, when the wave interacted with the damage, part of the wave reflected, and the rest continued to propagate forward. The echoed signals were accepted at location A. Figure 7 presents the results from the simulation comparing with the result in the literature (Giurgiutiu, Bao et al. 2003). Figure 7**(a)** is the signal under undamaged state, which has an initial signal at the front of the signal and an echoed signal located around 4e-4s. The amplitudes of the signals are different due to the different amplitude of the excitation. Figure 7**(b)** represents the results of an 8mm crack. These two signals had a similar reflection at 2e-4s, suggesting that the signal received from the damage. Figure 8 displayed the signals received at

sensors A to E. Note that there was a different in amplitude of the signals, the reason could be that the parameters of the signal and the material were not shown. The comparison verified the simulation used in this study was proper for Lamb wave simulation and thus the further exploration of simulation was used for the following parametric study and data generation.

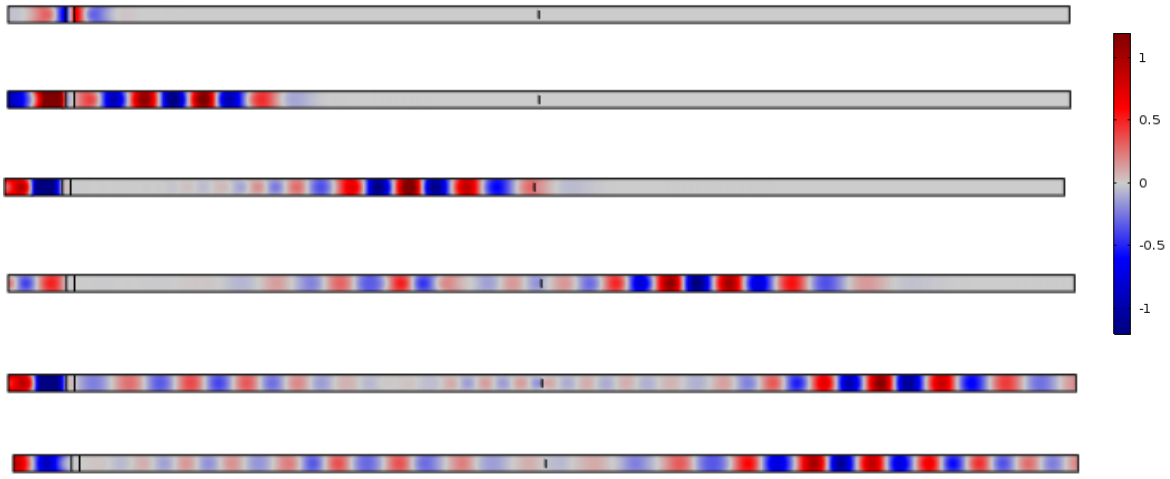

Figure 6. Wave propagation through the span.

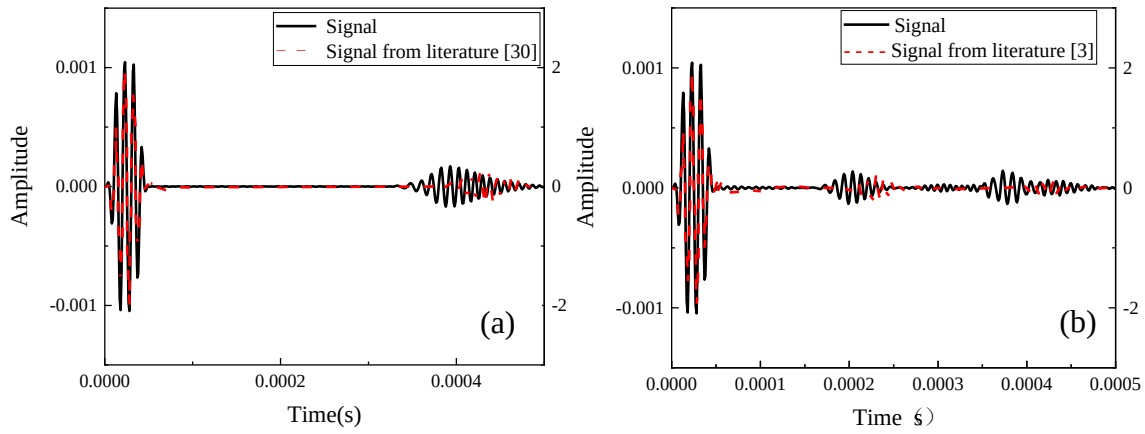

Figure 7. Comparison of the results. (a) Undamaged state predicted by the proposed work and literature(Giurgiutiu, Bao et al. 2003); (b) Damage state with 8-mm crack predicted by the proposed work and the literature (Giurgiutiu, Bao et al. 2003).

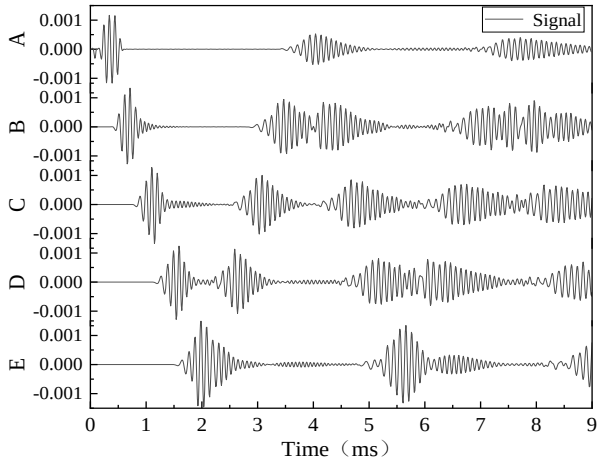

Figure 8. The signal received at sensors A-E predicted by the proposed work.

3.3.3. Design of Scenarios and Data Augmentation

3.3.3.1. Design of scenarios

Five different damage types were designed, including notch-shaped damage, circular-shaped damage, square-shaped damage, diamond-shaped damage, and oval-shaped damage. All these through-the-thickness damages were located at the middle of the plate. The length of them is 6mm equally. In addition, the notch-shaped damage was designed in 6 different sizes and 7 different orientations, similar to a crack. Therefore, the overall of 17 different states were designed and listed in Table 3. The excitation was a 5-cycle tone burst with Hanning window of frequency of 100 kHz used for the model.

Table 3. Test matrix for computation modeling.

Case	Label	Damage Type	Damage Size	Damage Orientation	Noise Interference
Reference	State #1	/	/	/	Noise levels of from 80dB to 120dB
Variance due to damage type	State #2	Notch-shaped damage	6-mm long	90 degree	
	State #3	Circular-shaped damage	6-mm diameter	/	
	State #4	Square-shaped damage	6-mm long	/	
	State #5	Diamond-shaped damage	6-mm long	/	
	State #6	Oval-shaped damage	6-mm long	/	
Variance due to damage size	State #7	Notch-shaped damage	2-mm long	90 degree	
	State #8	Notch-shaped damage	4-mm long	90 degree	
	State #2	Notch-shaped damage	6-mm long	90 degree	
	State #9	Notch-shaped damage	8-mm long	90 degree	
	State #10	Notch-shaped damage	10-mm long	90 degree	
	State #11	Notch-shaped damage	12-mm long	90 degree	
Variance due to damage orientation	State #12	Notch-shaped damage	6-mm long	0 degree	
	State #13	Notch-shaped damage	6-mm long	15 degree	
	State #14	Notch-shaped damage	6-mm long	30 degree	
	State #15	Notch-shaped damage	6-mm long	45 degree	
	State #16	Notch-shaped damage	6-mm long	60 degree	
	State #17	Notch-shaped damage	6-mm long	75 degree	
	State #2	Notch-shaped damage	6-mm long	90 degree	

3.3.3.2. Data augmentation and noise interferences

Response data from sensors could easily be contaminated by noise. Noise was added to the collected signals based on the signal to noise ratio (SNR) that represents the ratio of the signal strength to the background noise strength as (Lin, Pan et al. 2018):

$$SNR_{dB} = 10\log_{10}(\frac{P_{\text{signal}}}{P_{\text{noise}}}) \tag{28}$$

where P_{signal} and P_{noise} are the average power of signal and noise by dB scale, respectively. Five different noise levels, ranging from 80 dB to 120 dB, were selected to State # 1- 17 for machine learning to check the sensitivity of the uncertainty due to noise, which shown in Figure 9. Figure 9(a) represented the original signal of undamaged state and 6 mm-long damage state, which included the with damage reflected package and boundary reflected package. Figure 9(b) and (c) showed the signals with the SNR equal to 120 dB and 100 dB respectively. When SNR reduced to 80 dB, the damage package was difficult to identify.

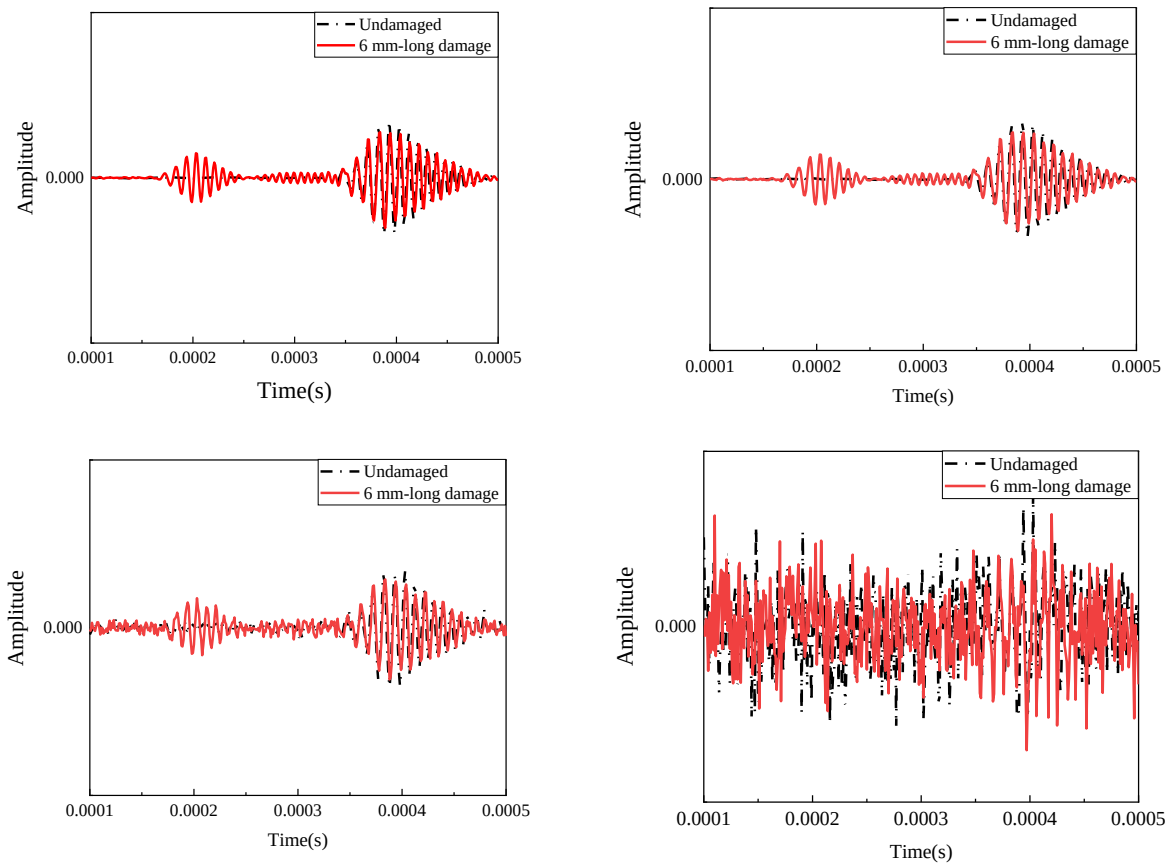

Figure 9. Noise level: (a) Original signal; (b) SNR = 120 dB; (c) SNR = 100 dB; (d) SNR = 80 dB.

3.4. Feature Representation and Classification using Machine Learning

3.4.1. Feature Extraction Methods

Lamb waves exhibit apparently non-stationary and nonlinear behavior. Hence, selection of damage-sensitive features is crucial to assist the classification and prediction (Pan, Lin et al. 2019). In addition, the robustness of the feature under noise is also an essential factor for selecting features (Gui, Pan et al. 2017). In this study, features were extracted from frequency-, time-, or time-frequency-domains, while those damage-sensitive features were then selected in accordance with feature selection methods.

In time domain, physics-based features play an important role in Lamb wave feature extraction. Amplitude, energy, and correlation coefficient are three features which can represent

the wave characteristic. The amplitude was obtained by the peak value of the damage wave packet. The energy calculated by the root mean square of wave (RMS) in the damage part were defined as

$$\text{rms} = \sqrt{\frac{1}{n}\sum_{i=1}^{n} e_i^2} \tag{29}$$

where n is the number of data point and e_i is the signal. The correlation coefficient under the damage state was used to compare with that of the health state.

In frequency domain, the amplitude was extracted as the features. 50 samples were generated randomly in each scenario by additive white Gaussian noise, which was used for feature extraction and feature selection.

Time-frequency domain analyze is effective to track the change of a system and its nonlinear behavior and the conventional techniques are mostly encompassed by the Wavelet transform. It shows a good deal of potential in nonstationary signals analysis due to excellent local zooming property of wavelet. By shifting and dilating the mother wavelet, a particular set of function, the signal can be decomposed which could preserve the temporal information. Meanwhile, the wavelet coefficients are obtained to weight the signal, which represents the feature of the signal.

Discrete wavelet transforms analyze the signal through decomposing it into successive low and high frequency components. By implementing a wavelet filter of particular frequency band shifts along the time axis, DWT analyzes the signal which makes the local examination of the signal become possible. The signal can be expressed as wavelet details and approximation in every level as shown (Lin, Pan et al. 2018)

$$x(t) = \sum_{i=1}^{n} D_i(t) + A_n(t) \tag{30}$$

where $D_i(t) and\ A_n(t)$ are the wavelet detail at the i^{th} level and the wavelet approximation at the n^{th} level. The frequency recursive relations are shown in Figure 10 for a full 5^{th} level wavelet

decomposition, called the Mallat-tree decomposition. DMeyer was chosen as the mother wavelet and six of the wavelet coefficients were applied as the damage sensitive features.

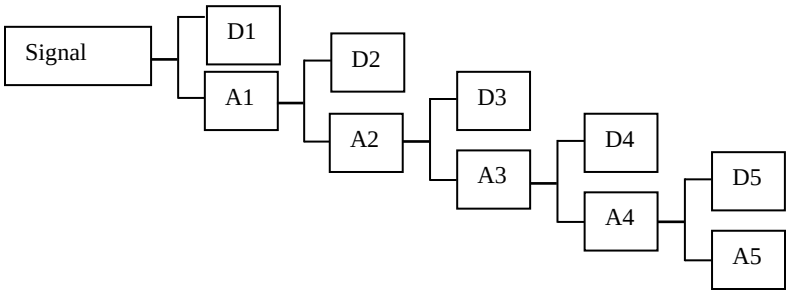

Figure 10. Full fifth level wavelet transform.

3.4.2. Feature Selection and Criteria

Relief algorithm (Kira and Rendell 1992) is a supervised features selection method. Its simplicity and efficiency enable determining the sensitive features, especially for binary classification. Relief-F extended the relief into multi-class problems (Kononenko, Šimec et al. 1997). It randomly selects an observation from the training data and then searches for the most similar samples (near hit) in the same class and the nearest instances in different class (near miss). For each feature, it calculates the weights vector according to the absolute difference between the selected sample with the near hit and the near miss. To consider the incomplete or noisy data which may cause the incorrect results, the relief-F selects *n* nearest hits and misses and calculates the average contributions to the weights instead of the single value. The differences between the values of attribute A for two observations I_1 and I_2, *diff(A,* I_1*,* I_2*)*, were defined as (Stief, Ottewill et al. 2018)

$$diff(A, I_1, I_2) = \frac{|value(A,I_1) - value(A,I_2)|}{\max(A) - \min(A)} \tag{31}$$

and then, relief-F's estimation *W*(*A*) was defined as the probabilities by the form:

$$W(A) = P(\text{different value of } A | \text{nearest instance from different class}) - P(\text{different value of } A | \text{nearest instance from same class}) \tag{32}$$

As a result, the relief-F algorithm gave a weight to each feature depending on the feature's ability to discriminate between samples in the different class. In this paper, this method was used to select the most sensitive feature among the different extracted features for further study.

3.4.3. Support Vector Machine for Classification

SVM is a powerful tool for classification in machine learning, which was developed by Vapnik (Vapnik 2013). The principle of SVM for classification is to construct a hyperplane which separates the data into two classes. It maps the input vector into a higher-dimensional feature space by applying kernel function (e.g. linear, polynomial or Gaussian radial basis function). An optimal hyperplane is then established in that feature space makes the separation by maximizing the margin from the hyperplane to the closest data points in either class.

Consider the set of training vectors $(\mathbf{x}_1, y_1), \ldots (\mathbf{x}_k, y_k), \in \mathbf{R}^N$ belonging to two classes ($y_i = \{-1, 1\}$). The aim is to look for the hyperplane to separate the data (Dibike, Velickov et al. 2001):

$$(\mathbf{w} \cdot \mathbf{x}) + b = 0, \mathbf{w} \in \mathbf{R}^N, b \in \mathbf{R} \tag{33}$$

where $\mathbf{w}$ is the weight parameter controlling the orientation of the hyperplane; b is a scalar threshold adjusting the bias of margins between the optimal hyperplane and the support vectors (HosseinAbadi, Amirfattahi et al. 2014). Then the feature space for the linear classifier is shown

$$f(\mathbf{X}) = \text{sgn}((\mathbf{w} \cdot \mathbf{x}) + b) \tag{34}$$

For the simplest case of a two-dimensional space, several linear classifiers could separate the data. The goal is to look for the hyperplane with largest margin, which is called the optimal hyperplane. Thus, all the training data are satisfying the constraints as follow (Burges 1998)

$$\mathbf{x}_i \cdot \mathbf{w} + b \geq +1 \text{ for } y_i = +1 \tag{35}$$

$$\mathbf{x}_i \cdot \mathbf{w} + b \leq -1 \text{ for } y_i = -1 \tag{36}$$

Combining the Eqns. (35) and (36) into one set of inequalities yields the decision space by the form

$$y_i(\mathbf{x}_i \cdot \mathbf{w} + b - 1 \geq 0), i = 1 \cdots k \tag{37}$$

The geometric distance from data point to hyperplane ($\mathbf{w}$, b) is shown (Boswell 2002)

$$d\big((\mathbf{w}, b), \mathbf{x}_i\big) = \frac{y_i(\mathbf{x}_i \cdot \mathbf{w} + b)}{\|\mathbf{w}\|} \geq \frac{1}{\|\mathbf{w}\|} \tag{38}$$

To obtain the optimal hyperplane, the maximum distance to the closest data points should be find. From the Eqn. (38), acquiring the maximum distance is same as finding the minimum value of $\|\mathbf{w}\|$. Therefore, the optimization could also change into a convex quadratic programming problem (Burbidge and Buxton 2001)

$$\text{Minimize } \boldsymbol{\Phi}(\boldsymbol{w}) = \frac{1}{2}\|\boldsymbol{w}\|^2 \tag{39}$$

Lagrange multiplier is the main method to finding the local maxima and minima of a function subject to equality constraints. The problem is transformed into (Burbidge and Buxton 2001)

$$L(\mathbf{w}, b, \Lambda) = \frac{1}{2}\|\boldsymbol{w}\|^2 - \sum_{i=1}^{k} \lambda_i [y_i(\mathbf{w}^{\mathrm{T}}\mathbf{x}_i + b) - 1] \tag{40}$$

where $\Lambda = (\lambda_1 \cdots \lambda_k)^{\mathrm{T}}$ are the Lagrange multiplier. The $L(\mathbf{w}, b, \Lambda)$ has to be minimized with respect to $\mathbf{w}$ and b, and maximized with respect to $\Lambda \geq 0$

$$\frac{\partial \mathbf{L}}{\partial \mathbf{w}} = \mathbf{w} - \sum_{\boldsymbol{i=1}}^{\boldsymbol{k}} \lambda_i y_i \mathbf{x}_i = 0 \tag{41}$$

$$\frac{\partial \mathbf{L}}{\partial b} = -\sum_{\boldsymbol{i=1}}^{\boldsymbol{k}} \lambda_i y_i = 0 \tag{42}$$

Then, the results are obtained as

$$\mathbf{w}^* = \sum_{i=1}^{k} \lambda_i y_i \mathbf{x}_i \tag{43}$$

Combining the Eqns. (42), (43) with Eqn. (40), the Eqn. (43) yields

$$F(\mathbf{\Lambda}) = \sum_{i=1}^{k} \lambda_i - \frac{1}{2}\|\boldsymbol{w}\|^2 \tag{44}$$

which could be determined in accordance with the Kuhn-Tucker theorem of optimization theory. Only when $y_i(\mathbf{x}_i \cdot \mathbf{w} + b)$ is equal to 1, the Lagrange multipliers are non-zero. The vectors $\mathbf{x}_i$ for those are called support vectors, which lies the closest to the separating hyperplane. Then b^* is expressed as

$$b^* = y_i - \mathbf{w}^{*\mathrm{T}}\mathbf{x}_i \tag{45}$$

The decision function is given by (Burbidge and Buxton 2001)

$$f(\mathbf{X}) = \mathrm{sgn}(\sum_{i=1}^{k} \lambda_i^* y_i K(x, x_i) + b) \tag{46}$$

where the $K(x, x_\mathrm{i})$ is the kernel function, and three commonly used types are listed below (Santos, Figueiredo et al. 2016):

a) the Gaussian radial basis function (RBF):

$$K(x, x_\mathrm{i}) = \exp(-\gamma\|x_i - x\ \ \|^2), \quad \gamma > 0 \tag{47a}$$

or b) the polynomial function:

$$K(x, x_i) = (\langle x, x_i \rangle + 1)^p \tag{47b}$$

or c) the sigmoid function:

$$K(x, x_i) = \tanh(\langle x, x_i \rangle + 1) \tag{47c}$$

In general, these three kernel functions, shown in Eqns. (47a)-(47c), tend to construct a higher dimensional feature space and allows a projectile of data to this hyperplane(s) to achieve being linearly separable. These kernel function helps SVM much more suitable for different dataset which can be used in non-linear classification. These different kernel functions have their applicability, including computation cost and parameter tuning. In this paper, RBF was selected as

the kernel function. To enhance the accuracy of the damage prediction, it is important to select suitable penalty coefficient and kernel function parameter for the SVMs.

Grid-search techniques (GS) was used to develop a set of optimal combination of the parameters (C, γ) in Eqn. (47). C is penalty coefficient adjusting the confidence interval range of the learning machine and γ is kernel function parameter changing the mapping function (Han, Qubo et al. 2012). The main steps of the GS method in SVM can be list. Firstly, gird search space needs to be built including the minimum and maximum value; Then, through orthogonal grid point matrix optimal value of parameter pairs (C, γ) are search and the fitness values of each point are calculated; Finally, the best values of parameters C, γ can be use in SVM model for classification. Although GS method would repeat the calculation for several times to search the optimal parameters, it is one of the simplest and most exhaustive method and can parallelize the searching for these two independent parameters (C, γ) (Hsu, Chang et al. 2003, Gui, Pan et al. 2017).

3.4.4. Assessment of Effectiveness of Learning Models using Roc Curves

The receiver operating characteristic (ROC) curves, which is generated by plotting the true positives rate against the false positives rate based on different thresholds, were employed as the evaluate tool in machine learning (Gui, Pan et al. 2017, Pan, Azimi et al. 2018). The area under the ROC curve (AUC) was summarized the degree or measure of separability. Consider that the method could be affected by skewed classes and insensitive to the change of class distribution, ROC was typically used in binary classification problems. Later, some researchers (Shah, Wang et al. 2017, Wang 2018) extended it to multi-class classification by binarizing the labels. In this study, ROC curves are used to measure the ability of SVM model which identify the damages.

3.5. Results and Discussion

3.5.1. Damage-sensitive Features

This section was to address the effectiveness and sensitivity of the feature extraction and feature selection methods for capturing proper features for damage detection. Features from different domains were plotted in Figure 11-Figure 13, in which six different damage states (State#2, #7 ~#11 in Table 3) and the reference state (State #1) were displayed when the SNR was 100 dB. As illustrated in Figure 11(a)-(c) demonstrated three features in time domain (i.e., amplitude, RMS and the correlation coefficient) and different symbols represented the different states for better visualizing different clusters.

Clearly, features using the amplitude, or the RMS provided distinguishable separation at most cases. Specifically, it seemed that RMS provided better result than the amplitude, because several crossed data were occurred between 10-mm and 12-mm damages using amplitude feature. Certain overlapping points were observed at the case of relatively small damage near 2mm-long damage state (in red circles in Figure 11(a) and (b)) with the reference in black asterisks. The results of the correlation coefficient were mixed together, which could not help to classify different states. As shown in Figure 12, the amplitude of the wave in frequency domain showed the similar result as the amplitude and RMS in time domain, easily to distinguish the bigger damage (from 4-mm to 12-mm cases) and hardly to separate the smaller cases with the references.

The results of the wavelet coefficients were shown in Figure 13, where three of the wavelet coefficients were in a coordinate system. Clearly, most features are more distinguishable. Data in state of base and 2-mm long damage were also much easier to separate.

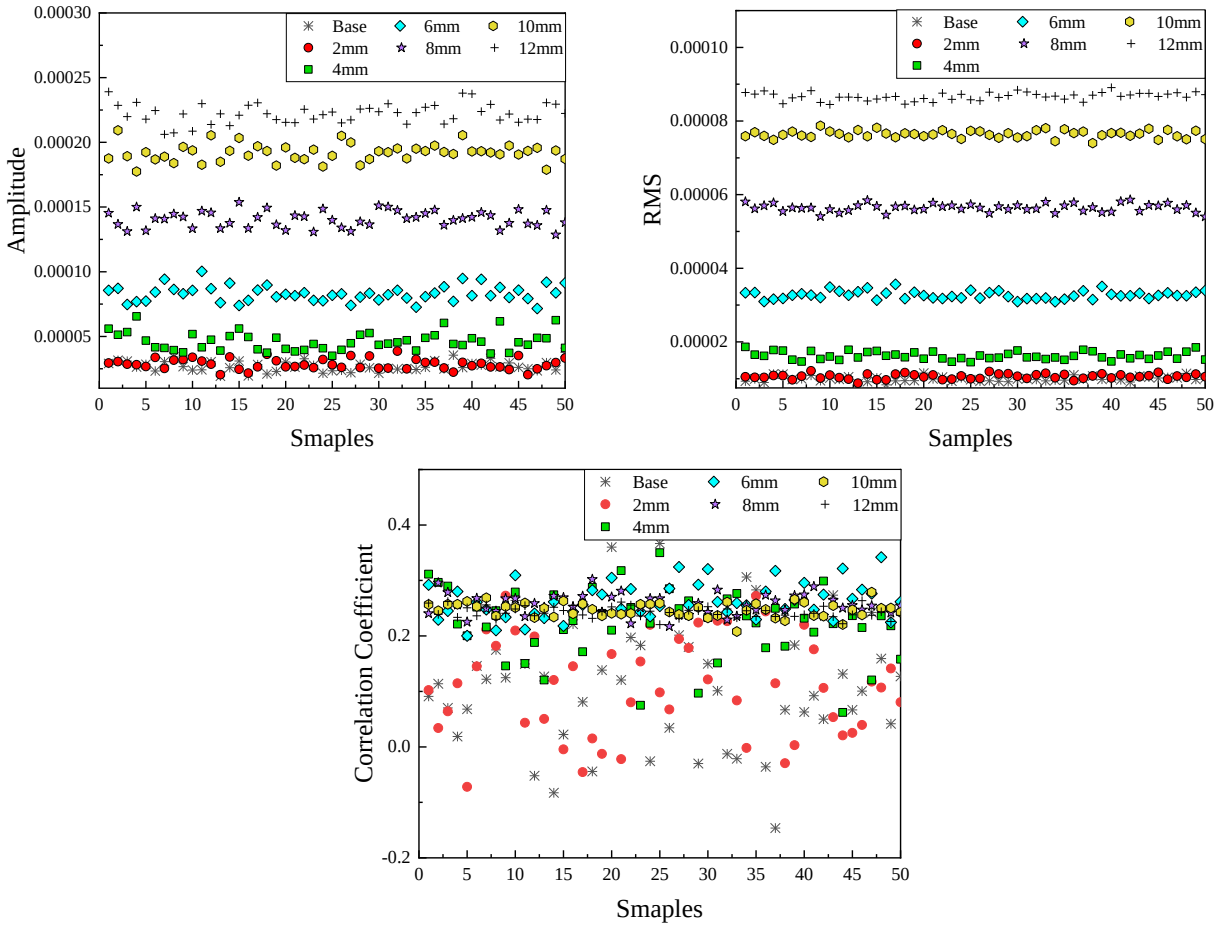

Figure 11. Features in time domain. (a) Amplitude; (b) RMS; (c) correlation coefficient.

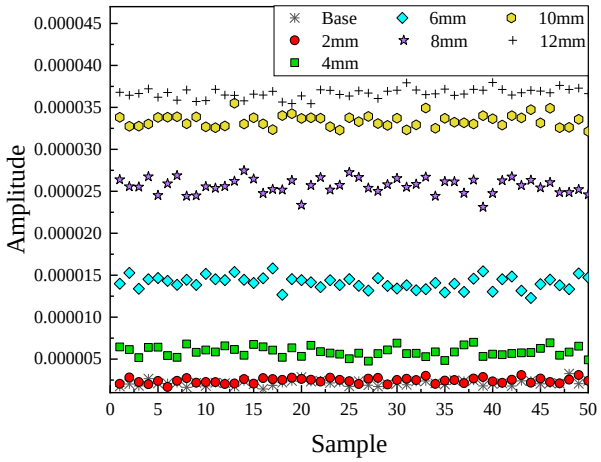

Figure 12. Features in frequency domain.

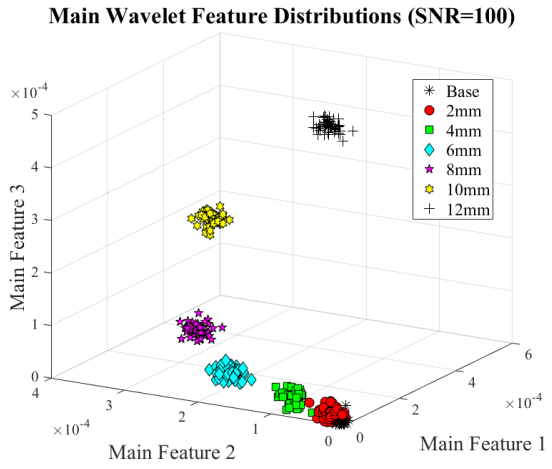

Figure 13. Features in time-frequency domain.

As stated, to quantitatively determine the quality of these features, Relief-F was used to rank the sensitive features in terms of their sensitiveness and the robustness, which is an individual evaluation filtering feature selection method for multi-label data (Urbanowicz, Meeker et al. 2018). It calculated the weights of features which could estimate the quality and the relevance between each feature and target classification.

For each damage scenario, 5 different noise levels (which SNR were decreased from 120dB to 80dB) were considered to analyze the robustness of the features under noisy condition. In Table 4, 10 features were ranked by relief-F method, including 6 wavelet coefficient features (W_1 to W_6), the amplitude of wave in time domain (Amp), the amplitude of the wave in frequency domain (Frq), the correlation coefficient (Cor) and the RMS of wave (RMS).

The best features in different noise levels are W_5, W_4 respectively which are all belonging to wavelet coefficients. On the contrast, correlation coefficient (Cor) indicates the worst results which was the same as Figure 11. Figure 14 shows the weights of each feature. At low noise level (SNR=120 dB), W_5, W_4, Amp have good performance for the classification which shows the higher weights comparing with other features. When SNR decreased, all the feature

weights declined, however, W_4 still maintaining the highest weight. Wavelet coefficient could reduce the effects of the noise which shows the stable high quality among other features. Hence these should be the most suitable features for further study.

Table 4. Feature selection.

Noise level	**Feature rank**									
	1st	2nd	3rd	4th	5th	6th	7th	8th	9th	10th
120dB	***W_5***	*W_4*	*Frq*	*W_6*	*RMS*	*W_2*	*Amp*	*W_1*	*W_3*	*Cor*
110dB	***W_4***	*Frq*	*RMS*	*W_5*	*W_2*	*Amp*	*W_1*	*W_6*	*W_3*	*Cor*
100dB	***W_4***	*RMS*	*Frq*	*W_5*	*W_2*	*W_1*	*Amp*	*W_3*	*W_6*	*Cor*
90dB	***W_4***	*W_1*	*RMS*	*Frq*	*W_2*	*W_5*	*W_3*	*Amp*	*W_6*	*Cor*
80dB	***W_4***	*W_1*	*Frq*	*W_3*	*RMS*	*W_2*	*W_5*	*Cor*	*Amp*	*W_6*

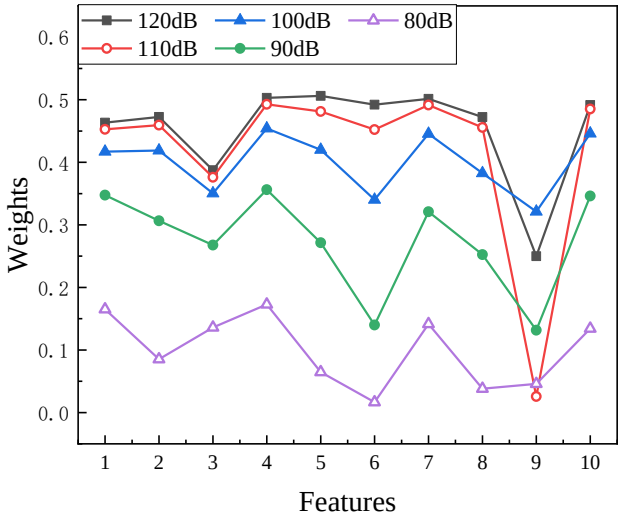

Figure 14. Weight of each feature under different noise levels.

Although the physics-based features can classify the damage into different state at a low noisy environment (SNR=100 dB), it is hard to get a high accuracy result under higher noise level. Table 5 shows the result of the classification with different method and features. Three physics-based features were used for classification by the traditional way respectively. Then, SVM was

involved by three feature groups, including physics-based features (Amp, Frq, Cor and RMS), all feature pools (4 of the physics-based features and 12 of the wavelet coefficients) and the selected features by feature selection methods.

Table 5. Accuracy of different features.

Method		**Classification by physics-based**			**Classification by SVM**		
Features					No feature selection		Feature selection
		Amp	*Frq*	*RMS*	Physics based Features	All Features	Selected features (Wavelet coefficients)
Noise level	120dB	100.00%	100.00%	100.00%	100.00%	100.00%	**100.00%**
	110dB	97.71%	100.00%	98.86%	98.86%	98.86%	**100.00%**
	100dB	81.14%	86.29%	84.00%	92.00%	84.00%	**95.43%**
	90dB	44.00%	64.00%	72.00%	80.00%	72.00%	**86.29%**
	80dB	19.43%	34.86%	39.43%	53.71%	39.43%	**56.00%**

By traditional method, Amp, Frq and RMS presented the good result at 120 dB and 110 dB. However, with the level of SNR increased, the accuracy of the separation was dropped down sharply. Specifically, only 39.43% of the data can be classified correctly through RMS which was the highest one comparing with the Amp (19.43%) and Frq (34.86%). On the other hand, SVM method showed the superiority by the high dimensional features which was much more accurate especially at high noise level states. In this method, the results were distinct by different feature groups. Using physics-based features to train the data, although the accuracy was reached to 100% (SNR = 120 dB), the ratio began to reduce into 98.86% at 110 dB and then decreased to 53.17% at 80 dB. To increase the dimension of the features, all the features were used for training data. The accuracy of each state was not increased dramatically, which was lower than the model trained by selected features. Clearly, using selected features, 95.43% of the data was identified at 100 dB

comparing with the 84% by all the features. In the case of SNR equal to 80 dB, nearly 17% of the accuracy was increased by feature selection. Therefore, SVM combining with the feature selection method can increase the accuracy of the classification.

3.5.2. Effectiveness and Sensitivity of Feature Extraction Methods to Data Classification

The waves traveled through the plate and echoed when it arrived the damage and boundary under different scenarios (shown in Figure 15(a)). In order to reduce the complexity of the signal, only the first three wave packets received by the receiver were used to analyze the characteristics of the signal. In the received signal, the first signal packet presented the excitation which was same in each scenario. The second packet collected at around 0.0002s represented the echoed wave from the damage part which certificated that the damage locates at the middle of the plate. Moreover, the third packet showed the echoed signal from the boundary away from the receiver. It is obvious that the wave gradually disperses when it propagates further. Therefore, the second packet carried the information of the damage which was chosen to extract the feature.

The signals with different damage types were received respectively in Figure 15(a). To analyze the received signal clearly, the signals were cut off at the second echoed signal, shown in Figure 15(b). The amplitude of each signal was close. Moreover, the frequency of each signal was slightly different. The red short line represented the square-shaped damage had highest amplitude (1.658e-4) and lowest frequency. On the contrary, the green dotted line (oval-shaped damage) had the highest frequency. The notch-shaped damage had the lowest amplitude which is 7.44e-5.

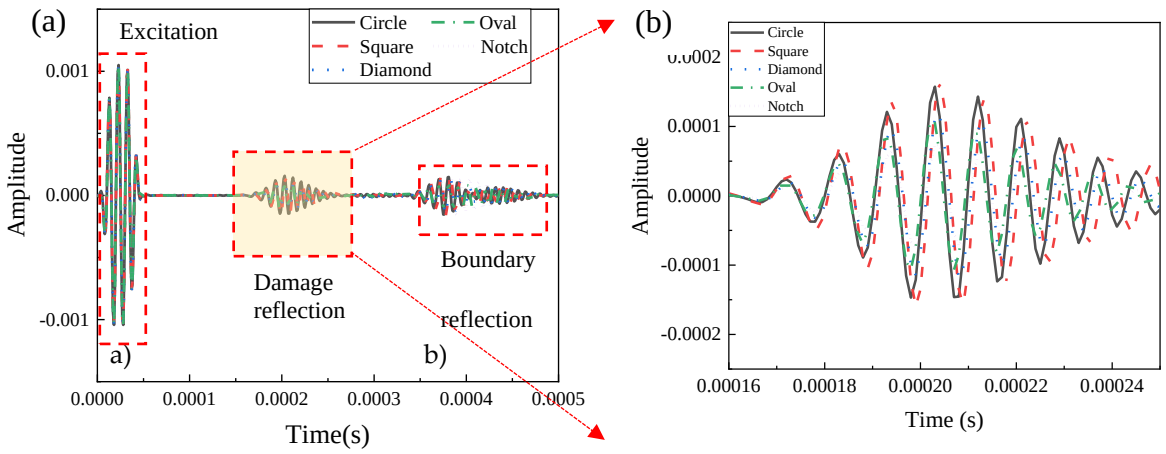

Figure 15. Received signals through Pitch-catch method.

From the result, 6 wavelet features were used to distinguish the damage types. To consider the interference of the noise and obtain more data, additive white Gaussian noise were added into the signal, which SNRs were set from 120 *dB* to 80 *dB*. Representing these data into the feature space, three of the wavelet features were selected to set a coordinate system. Figure 16 shows the feature clusters. 5 different shapes represented the different damage types. Clearly, the features could separate the data into different damage shapes under SNR= 90 *dB*.

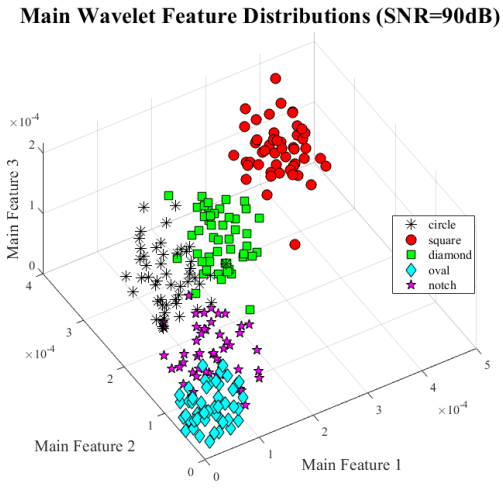

Figure 16. Damage features distribution (SNR=90dB).

The differences among these damage sizes were responded in Figure 17(b) which showed the detail of the damage part under different states. The frequencies of this part were similar when the length of damage changed. However, with the crack length increased, the amplitude of the receival signal at second packet was increased. Comparing the amplitude of base state in black short line and the 2-mm long damage in red dash line, the difference between them was small which the figures were 1.405E-6 and 7.421E-6 respectively. As the length of damage increased from 4mm to 10mm, the magnitude of the difference in amplitude rose obviously. When damage equaled to 12-mm long, the cyan-blue solid line had the highest amplitude, namely 2.246 E-4.

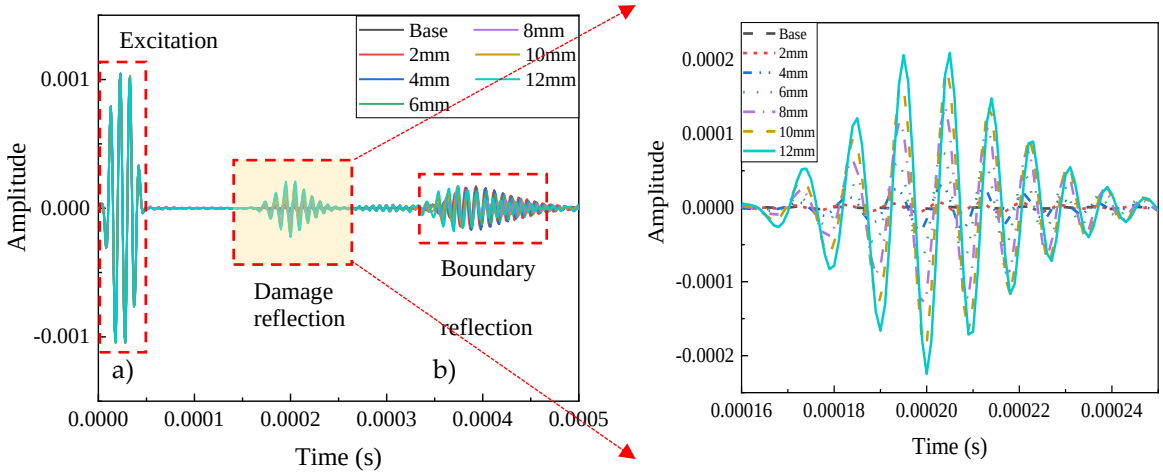

Figure 17. Received signals through Pitch-catch method.

As similar as the analysis of damage types, 6 wavelet coefficients were selected as the features under different noise levels. As clearly to illustrate in Figure 18(a) and (b), different colors and symbols were manifested the data belong to different states, which demonstrated the relationship between features and the classification of damage severities when the SNRs were equal to 100 dB and 90 dB respectively. In Figure 18(a), data were clustered into 7 groups. The black asterisk and red circular symbols indicated the data in base state and 2-mm long damage state. From the results, these two sets were partially crossed. With the damage length increasing, the distances between these groups became more farther, especially for the damage with 10-mm

and 12-mm long, which was easily to separate them into different states. However, the values of these features were divergent with the SNR decreasing, suggesting that the accuracy would be declining (shown in Figure 18(b)). The average deviation of these features was around 4E-10, which was much bigger than that of 100 *dB*, about 4E-11. Thus, it is hard to find thresholds to distinguish the data under base state, 2-mm long damage state and 4-mm long damage state due to apart of them mixed together. On the contrary, there was less effect for the larger damage state because of the greater distance between each one. Therefore, the features are extracted effectively and sensitively for classifying data.

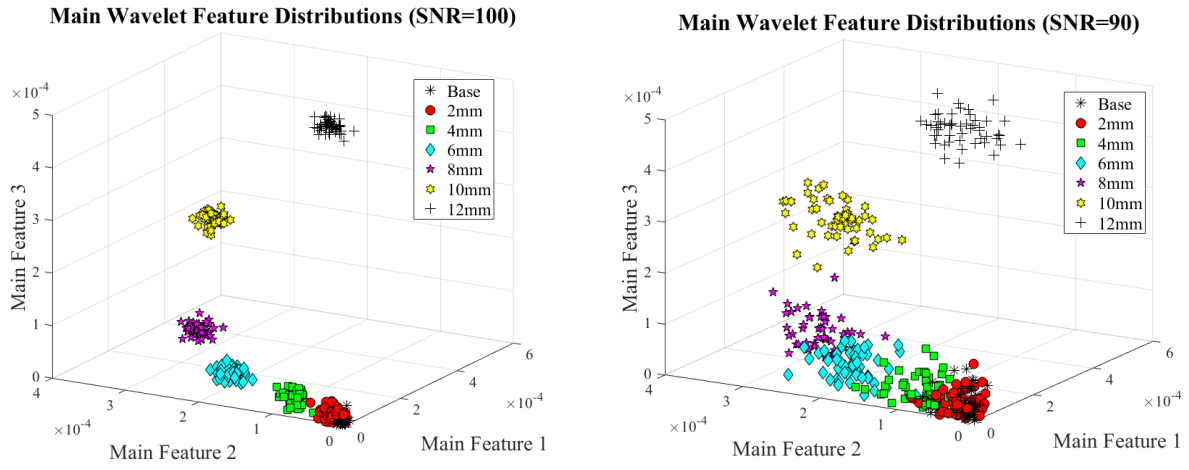

(a) Damage features distribution (SNR=100 *dB*) (b) Damage features distribution (SNR=90 *dB*)

Figure 18. Feature distribution under two different noise levels.

3.5.3. Effectiveness of Damage Type and Size to the Robustness of Feature Captured

SVM was used to classify the damage in 17 scenarios in terms of damage type, damage size and damage orientation. In each scenario, 50 sample data were randomly generated by the additive white Gaussian noise with the specific level where consists of 5 different levels as shown in Table 3. Under each noise level, 350 samples were involved in SVM model totally, which includes 50% of the data for training and the rest for testing. In Figure 19, confusion matrices which represented the accuracy of the prediction by SVM was shown when SNRs were 90*dB* and

80*dB* respectively. In Figure 19(a), the classification was 100% correct by SVM. With the noise increase, the accuracy of the prediction was drop down sharply which was only 77.6% in 80 *dB*. 16.7% of the circular-shaped damage was misjudged into diamond. Diamond-shaped damage and oval-shaped damage had lower accuracy as 71.4% and 62.9%, respectively, which means that they were much easier to misjudge to other shapes.

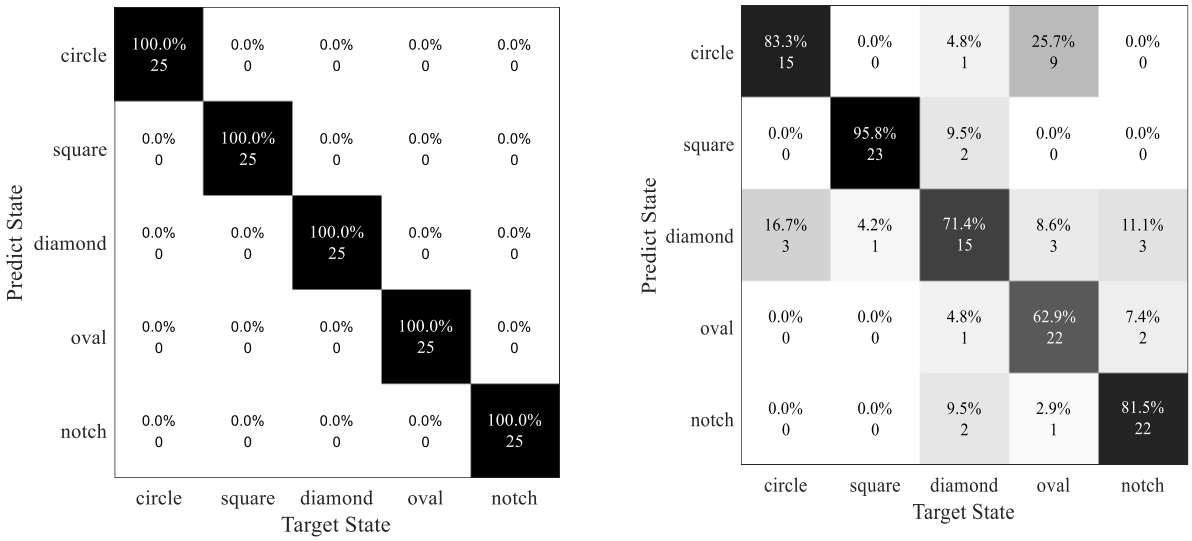

(a) SNR = 90 *dB*, accuracy = 100%

(b) SNR = 80 *dB*, accuracy = 77.6%

Figure 19. Classification of damage types under two noise levels.

In Figure 20, confusion matrices were used for representing the result of the classification by SVM as SNRs were set to 100 *dB* and 90 *dB* respectively. In these two matrices, the horizontal scale showed the target state of each data, and the vertical scale displayed the predict result of the data-driven method.

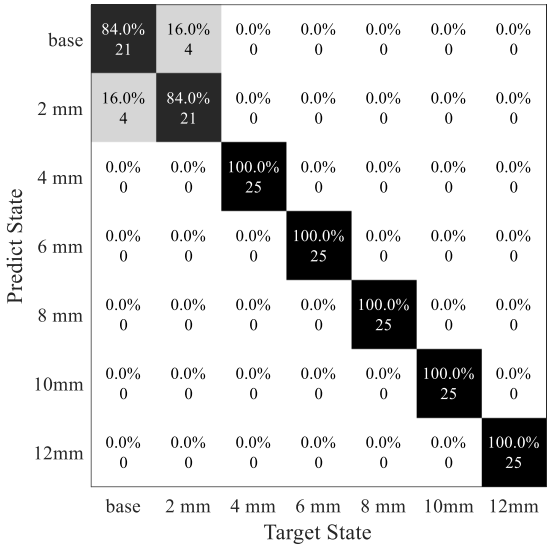

(a) SNR = 100 *dB*, accuracy = 95.4%

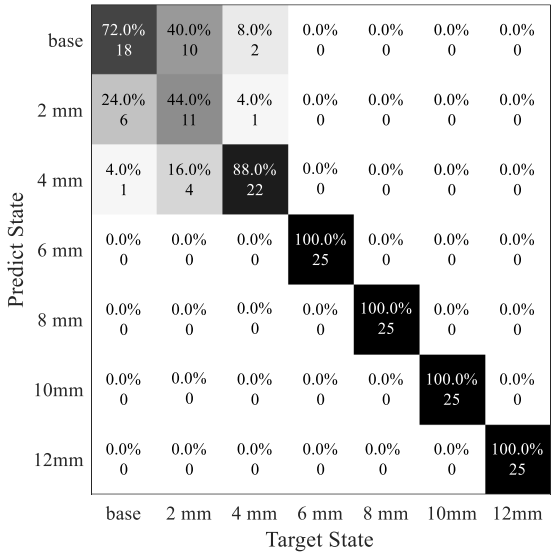

(b) SNR = 90 *dB*, accuracy = 86.3%

Figure 20. Classification of damage sizes under two noise levels.

In Figure 20(a), the average accuracy for classifying the damage severity was equal to 95.43% which means that the most data were discriminated into the correct classifications. However, 4 of the samples belonging to 2-mm long damage were distributed into base state. And 4 data points in 2-mm long damage were detect into base state. Increasing the noise level (SNR=90 *dB*), the average accuracy was decreased to 86.29% (see Figure 20(b)). The errors were happened at small damage, especially on base state and 2-mm long damage state. The target labels of the 25 samples were in base state, of which 6 samples were misled into 2-mm long damage state and 1 sample was misled into 4-mm long damage state. In damage condition of 2-mm long, 44% of the data was predicted as a true label, 40% sample was misinformed into base state and 16% of them was in 4-mm long damage state in false. Similarly, 2 samples with 4-mm long damage had misjudged as base state and one misled into 2-mm damage state. In addition, the rest of the data were detected into the correct labels.

Despite that the average accuracy of classification under specific noise level was high, the confusion between small damage and reference state occurred frequently. Hence, the ROC curves

in Figure 21 provided the reference for the accuracy of categorizing the base state and small damage states (2mm-long damage and 4mm-long damage state) under different noise levels. Figure 21(a) depicted the ROC curves only considering the base state and 2mm-long damage state when SNRs were from 80dB to 120 dB respectively. As usual, the more the ROC curve is tilted towards the left, the larger the AUC values are, where means that the result is much more acceptable. In 120dB level and 110dB level, the classifications were entirely correct which the AUCs were equal to 1. It dropped to 0.7856 while noise level changed to 100dB. The previous study(Fan, Upadhye et al. 2006) confirmed that the prediction is unacceptable if the AUC is lower than 0.75. Obviously, when noise level increased to 90dB and 80dB, the values of AUCs were 0.6496 and 0.4325, respectively, which fell in unacceptable zones. As shown in Figure 21(b), the results of comparing the base state with 4mm-long damage state were quite better than that the previous one. Specifically, the precise predictions were obtained when SNRs were from 120dB to 100dB. The AUC was equal to 0.9328 due to the noise level of SNR=90dB. And it is lower than the threshold of 0.75 at 80dB situation.

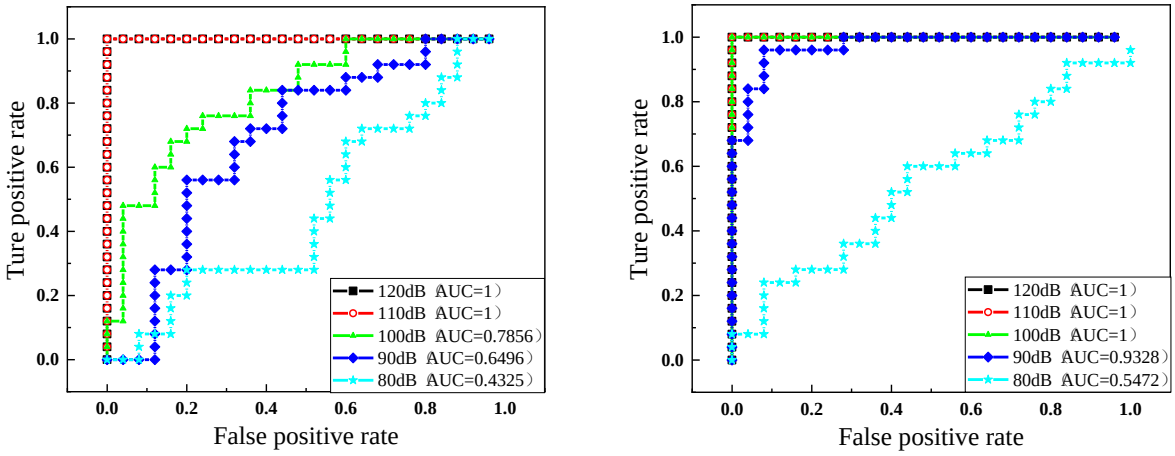

Figure 21. The ROC curves for multiclass: (a) Comparison between State #1 and #7; (b) Comparison between State #1 and #8.

3.5.4. Effectiveness of Damage Orientation to the Robustness of Feature Captured

Detecting the orientation of damage is also a significant and difficult issue in Lamb wave-based health monitoring. The 6-mm long notch-shaped damage was rotated 15-degree clockwise each time so that 7 different orientations were set up. The received signals from the finite element model were plotted in Figure 22. The second package brought the information about the damage, and the frequencies of the waves in this part are similar. Figure 22(b) showed the details of the signals which illustrated that the amplitudes of the signals were reduced from 7.439E-5 to 1.658E-5 as the angle of damage increasing from 0^o to 90^o because of the vertical projected area decreased. As the horizontal projection increased, the length of the wave packet was climbing. The black solid line represented the initial state (6mm-long damage without rotation) which had the highest peak value and the packet was from 0.00016s to 0.00026. As for the cyan-blue dotted line presenting the 6mm-long damage with 90-degree orientation, the amplitude was the smallest, but the packet length increased.

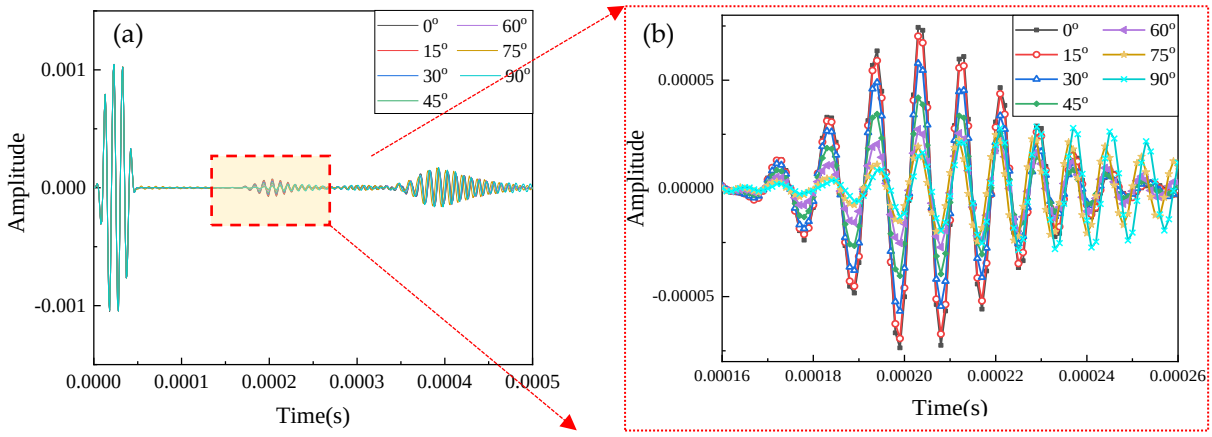

Figure 22. Received signals through Pitch-catch method.

Figure 23(a) showed the result of the feature distribution under 100 *dB*. Wavelet coefficient features clearly classified these data into seven different groups which distributions were quite different from the damage severity. The distances between each group were similar. The result of

the identification was shown in Figure 23(b). Different from the damage severity, the misleading might happen in any of the state. For instant, five of the base state samples were misled into the 15-degree rotation state, and 3 of the 15-degree rotation state data were misjudged as base state. At rest of the state, the most of predictions are allocated into the target state, except 2 misleading in 60-degree rotation, one misled in 75-degree rotation state. The accuracy of the SVM classification was 93.71%, which was a little lower than the classification in damage severity.

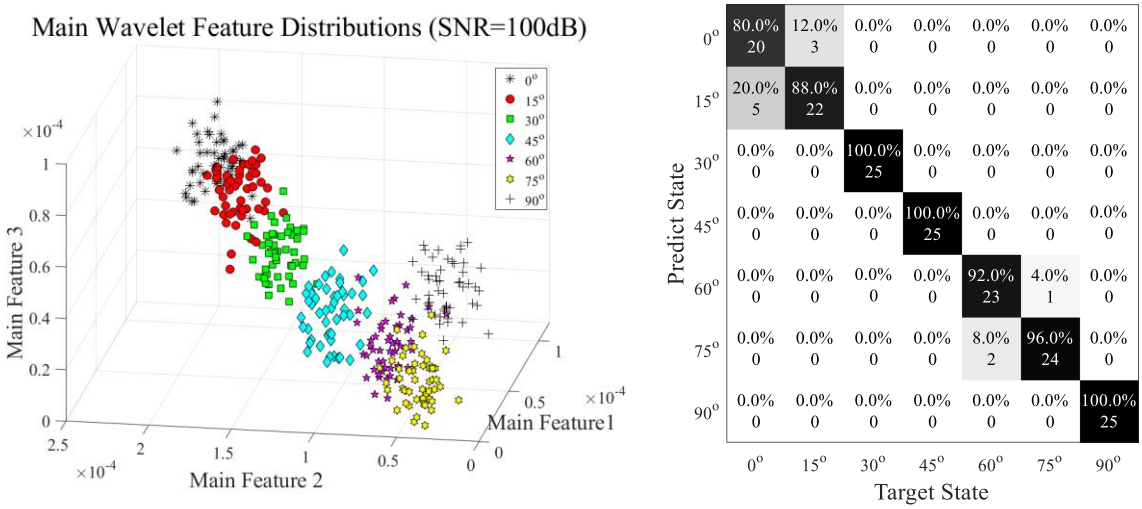

(a) Feature distribution

(b) Confusion matrix
(accuracy = 93.7%, SNR = 100 *dB*)

Figure 23. Damage identification results.

3.6. Discussion of Structural Uncertainty Related to Engineering Applications

3.6.1. Impacts of Structural Uncertainty Due to Noise Interferences to the Robustness of Data Classification

One of the greatest challenges in signal processing is uncertainty from noise (e.g., measuring noise from sensor systems and environmental noise) that usually interferes with raw data. State #1-17 were designed under 5 different noise levels which the SNRs were equal from 80 *dB* to 120 *dB* as listed in Table 3, to address how effectively and sensitively the features gained by feature extraction methods response under certain noise level.

Figure 24(a)-(c) showed the accuracies of the damage identification in different noise levels under four conditions. They all represented that when the SNR was higher, the accuracies of the classification were increased. In damage type prediction, the accuracy was reach to 100% when the SRN is higher than 90 *dB*. However, the accuracy was drop down dramatically at 80 *dB*. At the same level, only 52.57% of the data was distinguished into the target state when classified the different damage size. When the SNR was bigger than 105 *dB*, the accuracy was reached to 100%. At the orientation identification analysis, the value was lower than the damage size analysis, which just had 29.14% of the data classified into the target label at 80 *dB*. When the SNR increased, the accuracy was rising dramatically, which was 53% at 90 dB and 89.14% at 100 dB. The SNR arrived 100% at 110 dB. Therefore, the noise is a critical issue to affect the classification results directly. When SNR was 110 dB or above, the prediction is precise in all conditions. However, when SNR approached to 80~90 dB, the wave packet which carries the information of the damage would be overlapped by noise, so that it is hard to distinguish them into target state.

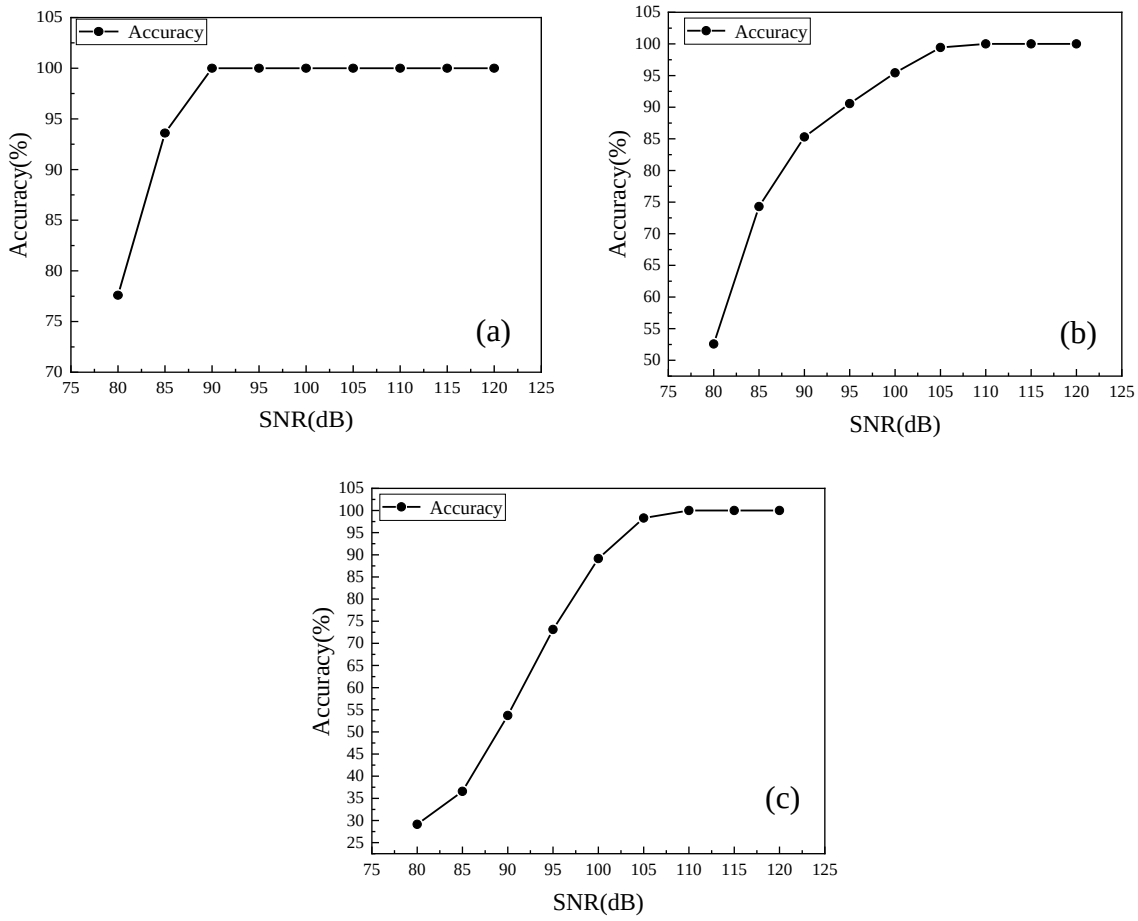

Figure 24. Damage identification to noise interference: (a) Damage type; (b) Damage size; (c) Damage orientation.

3.6.2. Impacts of Structural Uncertainty Due to Mixed Data Types to the Robustness of Data Classification

Collected data could be mixed in more complex conditions with different damage orientation, damage level, and damage types. Therefore, this section was to use trained models to classify the mixed data types with 325 data points in totally 13 states, including different levels of damage size and orientation together, as shown in Table 3.

Figure 25 (a) demonstrated the feature extraction in different states when SNR was equal to 100 dB, noticed that most of the data can be grouped by the wavelet coefficients. Specifically, the cluster of different damage orientations were situated between the 6mm-long damage group

and 2mm-long damage group which proved that the vertical projected area of the damage was the essential factor to determine the features' value. The feature of damages with 15-degree, 30-degree and 45-degree were placed between 6mm-long and 4mm-long damage, and 60-degree, 75-degree and 90-degree feature were located between 4mm-long and 2mm-long damage. Some overlaps appeared between adjacent clusters causing the accuracy of the classification reduced.

Figure 25(b) illustrated the SVM classification results among 13 different states under SNR equaling to 100 dB. The average accuracy was 89.54%. The misleading between base state and State #7 was still existed, which had 4% of the data belonging to the base state predicted into State #7 and 28% of the data should be State #7 predicted into the base state. Moreover, 8 of the 25 samples in 4 mm-long damage state were misled to wrong state, including 2 for 45-degree state and 4 for 60-degree state respectively. Similarly, 60-degree state was much easier to confuse with the 4mm-long damage state containing 5 wrong predictions. In addition, 6 mm-long damages were similar with the damage rotated 15-degree leading to 20% samples misjudged and in 15-degree damages data, 8% samples misjudged. Figure 25 (c) exhibited the accuracy of classification when having mixed damage size and orientation identification. Clearly, the similar trend was observed as stated in Figure 25 (a)-(c). When SNR was equal to 80 dB, only 28.62% of the data could be detect into the correct label. Increasing the SNR, the accuracy was ascended to 52.62% at 90 dB and 89.54% at 100 dB.

Although the accuracy of classification considering the damage size and orientation together is lower than that of the individual analysis of damage size or orientation, this method is enough to guide us to understand damages in detail.

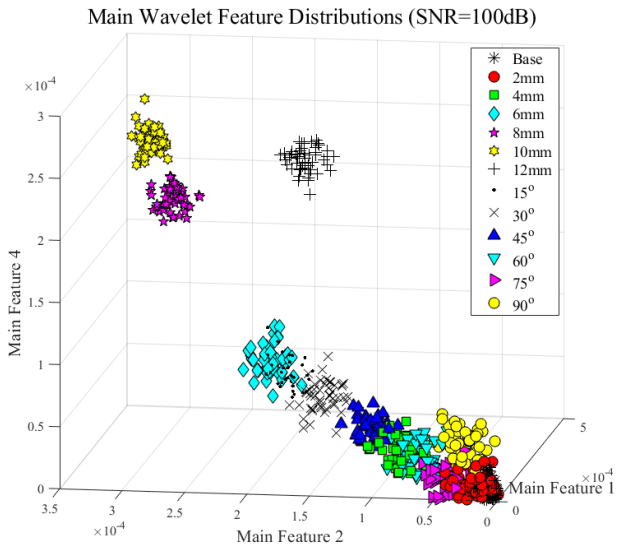

(a) Feature distribution

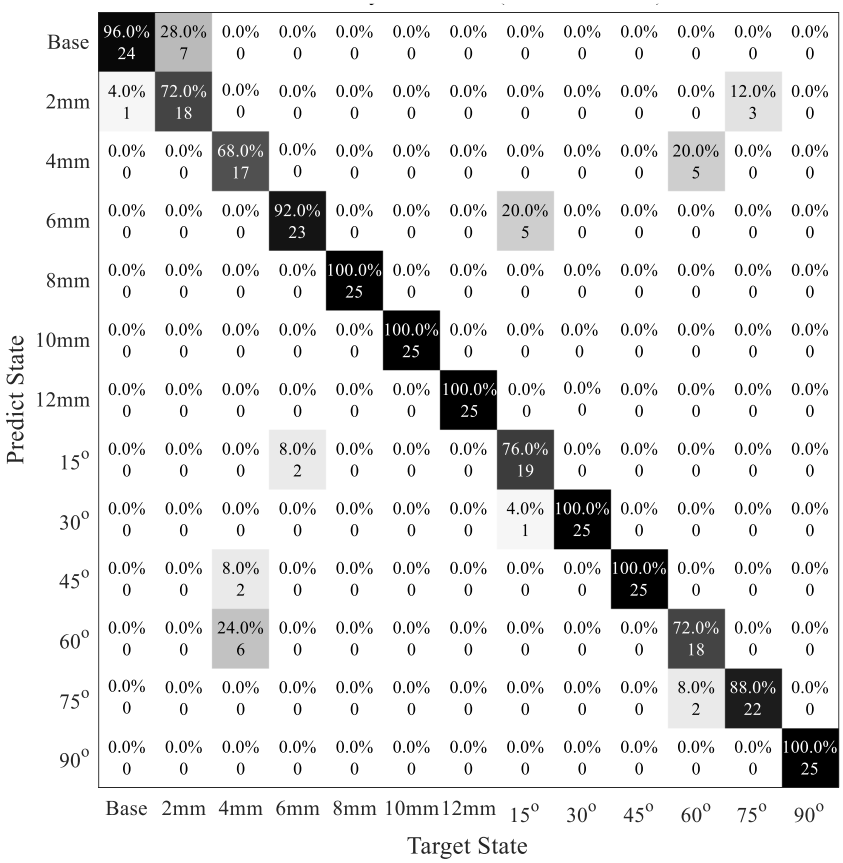

(b) Confusion matrix (accuracy = 89.54% SNR = 100 *dB*)

Figure 25. Data classification for mixed data types: (a)-(c).

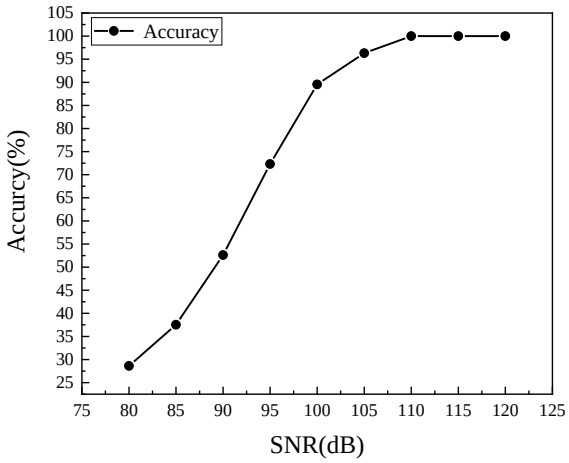

(c) Noise interference

Figure 25. Data classification for mixed data types: (a)-(c) (continued).

3.6.3. Impacts of Structural Uncertainty Due to Material Discontinuity from Weldment to the Robustness of Data Classification

Material discontinuity due to weldment creates more complexity for lamb wave signal process. This section was to discuss the effectiveness of the proposed method for classifying such structural uncertainty. To test the accuracy of this model, a new dataset was built by numerical simulation method. The identical plate, illustrated in Figure 26, was modified by adding a butt weldment at location of point B and a 6mm-long notch at location of point C, shown in Figure 26(a). The width of the weldment was 5 mm and the welding filler was Ti-6Al-4V. To enlarge the data, 175 signals were augmented using white Gaussian noise with different levels.

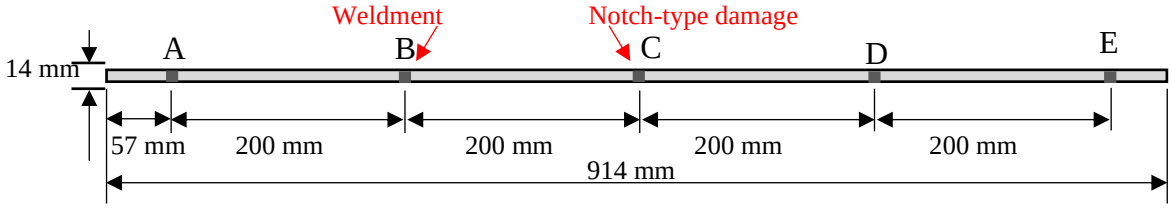

(a) Plate with a butt-welded joint at point B and a 6-mm long notch-type damage at point C.

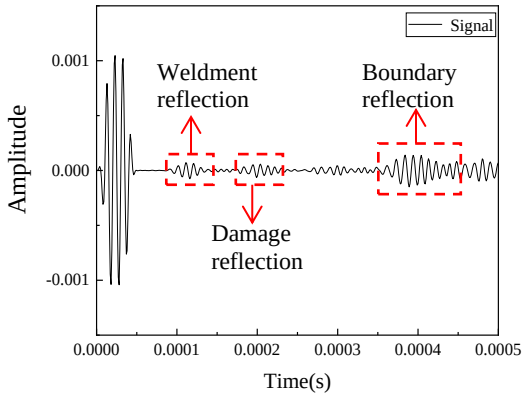

(b) Signal collected from point A

Figure 26. Plate with weldment and 6 mm-long notch-type damage (a)-(b).

With the interaction of the weldment, the received signal had more reflected packages than that of the previous one, shown in Figure 26(b). From the signal, the reflections came from the weldment, damage and the boundary. The label of each data was predicted by SVM which was trained in section 5. Table 6 showed the comparation of the predicted result in 6 mm-long damage and the one added the weldment. Clearly, the prediction of the damage with the weldment post challenge in classification as compared to cases without weldment. Specifically, in most of the case (shown in Figure 27), 6-mm long damage was classified accurately which was 100% expect the SNR equal to 80 dB. With the weldment appeared, it was interfered the signal and reduced the accuracy of the prediction. However, most of the damage could be test by this model. A total of 80% of damaged cases were classified into 6 mm-long damage group, and 20% of the damage was predicted as 4 mm-long at 100 dB. The misleading was increased to 26.9% when noise level approached 90 dB.

Table 6. Prediction.

Noise level	120 *dB*	110 *dB*	100 *dB*	90 *dB*	80 *dB*
Without weldment	100.00%	100.00%	100.00%	100.00%	56.4%
With weldment	100.00%	100.00%	80.00%	73.10%	65.71%

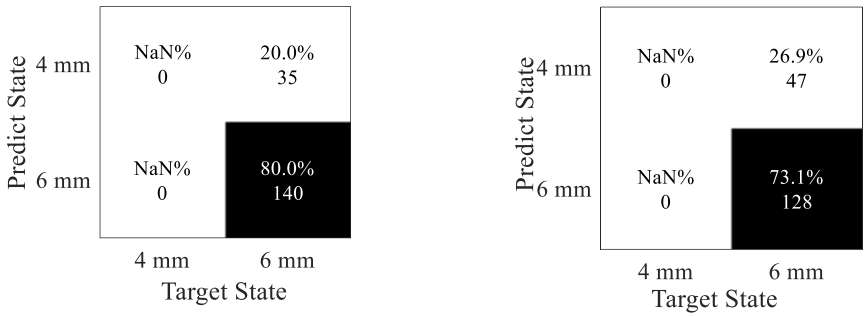

(a) SNR = 100 *dB*, accuracy = 80.0% (b) SNR = 90 *dB*, accuracy = 73.1%

Figure 27. Classification of damage sizes under two noise levels.

3.7. Summary

This study investigated Lamb wave-based damage detection method enriched by machine learning to accelerate classification associated with damage size and orientation. The dataset of Lamb wave propagation through the aluminum beam was generated using simulation. Different features under different domains were extract and evaluated using feature selection methods. Impacts of noise interference on the effectiveness of the methods were also addressed. Some conclusions can be drawn as follows:

a) The learning framework provided a workflow from dataset generation, to sensitive feature extraction, to prediction model for lamb-wave-based damage detection. Note that although SVM learning algorithms were designed for learning model training, deep learning could be deployed in future work.

b) Different features generated from different domains could provide various levels of sensitivity to damage. With the aid of feature selection, time-frequency features and

wavelet coefficients, exhibited the highest damage sensitivity, as compared to the features in either the time domain or frequency domain. These features that contained the information in btimestime-frequency domainsmains are also much more robust to noise.

c) The results in the case study demonstrate that the SVM method can effectively classify the damage type and damage size to certain noise levels, near 110 dB. With the increase of noise to 80 dB, the accuracy of the classification dramatically dropped to 57%.

d) The damage orientation can be classified using features of wavelet coefficients. The accuracy of the result was slightly lower than that of damage size, mainly because the signals generated by the finite element method were from one-dimensional propagation of the wave, and thus lacked the entire spatial information about the two-dimensional orientation. For further study, two-dimensional wave propagation could be used for more accurate spatial information about the damage.

e) Noise interference, mixed data types, and level, and material discontinuity from weldment was used to address structural uncertainty and their impacts tonthe effectiveness of the proposed methods. The findings revealed that the proposed methods were still effective for data classification. Further research will be carried out, as noise is still a big challenge when its level reached uhe ailar order as the signals were, while material discontinuity from weldment also posted complex situation for classification.

3.8. References

Ahmed, M. N. J. D. and T.-. Gradworks (2014). "A Study of Guided Ultrasonic Wave Propagation Characteristics in Thin Aluminum Plate for Damage Detection." *Dissertations & Theses - Gradworks*

Boswell, D. (2002). "Introduction to support vector machines." *Departement of Computer Science Engineering University of California San Diego*.

Burbidge, R. and B. Buxton (2001). "An introduction to support vector machines for data mining." *Keynote papers, young OR12*: 3-15.

Burges, C. J. (1998). "A tutorial on support vector machines for pattern recognition." *Data mining knowledge discovery* 2(2): 121-167.

Dibike, Y. B., S. Velickov, D. Solomatine and M. B. Abbott (2001). "Model induction with support vector machines: introduction and applications." *Journal of Computing in Civil Engineering* 15(3): 208-216.

Fan, J., S. Upadhye and A. Worster (2006). "Understanding receiver operating characteristic (ROC) curves." *Canadian Journal of Emergency Medicine* 8(1): 19-20.

Farrar, C. R. and K. Worden (2007). "An introduction to structural health monitoring." *Philos Trans A Math Phys Eng* 365(1851): 303-315.

Giurgiutiu, V., J. Bao and W. Zhao (2003). "Piezoelectric wafer active sensor embedded ultrasonics in beams and plates." *Experimental mechanics* 43(4): 428-449.

Gui, G., H. Pan, Z. Lin, Y. Li and Z. Yuan (2017). "Data-driven support vector machine with optimization techniques for structural health monitoring and damage detection." *KSCE Journal of Civil Engineering* 21(2): 523-534.

Han, S., C. Qubo and H. Meng (2012). *Parameter selection in SVM with RBF kernel function*. World Automation Congress 2012, IEEE.

HosseinAbadi, H. Z., R. Amirfattahi, B. Nazari, H. R. Mirdamadi and S. A. Atashipour (2014). "GUW-based structural damage detection using WPT statistical features and multiclass SVM." *Applied Acoustics* 86: 59-70.

Hsu, C.W., C.C. Chang and C.-J. Lin (2003). "A practical guide to support vector classification." *National Taiwan University*.

Kira, K. and L. A. Rendell (1992). *The feature selection problem: Traditional methods and a new algorithm*. AAAI Press.

Kononenko, I., E. Šimec and M. Robnik-Šikonja (1997). "Overcoming the myopia of inductive learning algorithms with RELIEFF." *Applied Intelligence* 7(1): 39-55.

Lin, Z., H. Pan, X. Wang and M. Li (2018). Data-Driven structural diagnosis and conditional assessment: from shallow to deep learning. *SPIE Smart Structures and Nondestructive Evaluation*. Denver, CL, USA.

Lin, Z., H. Pan, X. Wang and M. Li (2018). *Data-driven structural diagnosis and conditional assessment: From shallow to deep learning*. Sensors and Smart Structures Technologies for Civil, Mechanical, and Aerospace Systems 2018, International Society for Optics and Photonics.

Pan, H., M. Azimi, F. Yan and Z. Lin (2018). "Time-frequency-based data-driven structural diagnosis and damage detection for cable-stayed bridges." *Journal of Bridge Engineering* 23(6): 04018033.

Pan, H., Z. Lin and G. Gui (2019). "Enabling Damage Identification of Structures Using Time Series-Based Feature Extraction Algorithms." *Journal of Aerospace Engineering* 32(3): 04019014.04019011-04019014.04019015.

Santos, A., E. Figueiredo, M. Silva, C. Sales and J. Costa (2016). "Machine learning algorithms for damage detection: Kernel-based approaches." *Journal of sound and vibration.*363: 584-599.

Shah, M., D. Wang, C. Rubadue, D. Suster and A. Beck (2017). *Deep learning assessment of tumor proliferation in breast cancer histological images*. 2017 IEEE International Conference on Bioinformatics and Biomedicine (BIBM), IEEE.

Stief, A., J. R. Ottewill and J. Baranowski (2018). *Relief F-Based Feature Ranking and Feature Selection for Monitoring Induction Motors*. 2018 23rd International Conference on Methods & Models in Automation & Robotics (MMAR), IEEE.

Urbanowicz, R. J., M. Meeker, W. La Cava, R. S. Olson and J. H. Moore (2018). "Relief-based feature selection: introduction and review." *Journal of biomedical informatics* 85: 189-203.

Vapnik, V. (2013). *The nature of statistical learning theory*, Springer science & business media.

Wang, Z. (2018). "Deep learning-based intrusion detection with adversaries." *IEEE Access* 6: 38367-38384.

4. CONVOLUTIONAL NEURAL NETWORK BASED DAMAGE DIAGNOSIS OF STRUCTRES WITH WELDMENT BY ULTRASONIC GUIDED WAVE

4.1. Introduction

Welding is widely used in the connection of metallic structures, including welded joints in oil/gas metallic pipelines and other structures. Welding processes are vulnerable to in the clusion of different types of welding defects such as lack of penetration and undercut. These defects often initialize early-age cracking and induced corrosion. In addition, the occurrence of damage in structure is usually not single, but multiple, which increases the difficulty of damage detection. As such, identification of weldment defects and associated damages at their early stage are crucial to ensure structural integrity and avoid potential premature failure. The current strategies of damage identification are achieved using ultrasonic guided wave approaches that rely a on change of physical parameters of propagating waves to discriminate whether there exist damaged states or not. However, the inherent complex nature of weldment, the complication of damages interactions, and large-scale/long span structural components integrated with structure uncertainties post great challenge in data interpretation and making informed decision. Artificial intelligence and machine learning have recently become an emerging method for data fusion, great potential for structural signal processing through decoding ultrasonic guided waves. Therefore, this study aimed to employ the deep learning method, convolutional neural network (CNN), for better characterization of damage features in terms of welding defect type, severity, and locations of the cracks. The architecture of the CNN was set up to provide the effective classifier by parameters analysis. A total of 16 damage states were designed to generate data for training and testing the accuracy of the proposed method. In addition, the effectiveness of the CNN model was examined by noise interference to consider the structure uncertainties. The results certificated that the deep learning

method automatically extracted features of ultrasonic guided waves and obtained high-precision prediction for damage detection in complex situations, for instance, welding defect and crack combined. Moreover, signals were also classified correctly by the CNN in high noise level.

4.2. Databases Generation

Ultrasonic guided waves generated by piezoelectric actuators can propagate along the pipe and change when excited guided wave signals encounter defects or other material discontinuity. Different damage location and severity can cause the wave scattering in the form of mode conversion, reflection and transmission which makes the ultrasonic guided wave-based damage detection complicated. As a result, acquiring the knowledge of guided wave dispersive behavior, mode shapes, and suitable frequency range will make the damage detection susceptible to control.

4.2.1. Calibration of Simulation

This section attempted to calibrate the model set by finite element and indicate characteristics of guided wave propagating along a structure. The prototype was a 2000 mm long steel pipe in paper (Xu, Luo et al. 2019), the outside diameter was 76 mm and the inner diameter was 68 mm. Two notch-shaped damages were located symmetrically at 1400 mm away from the left side. The dimensions of the defects were 2 mm in axial width, 3mm depth and 35mm in circumferential length. The material density was 7850 kg/m^3, Youngs' modulus was 210 GPa, and Poisson's ratio was 0.28. Free triangular elements available in COMSOL were used to mesh the pipe. To ensure the calculation accuracy and consider the computational efficiency, the maximum element size is 5 mm, and the minimum element size is 2 mm. In addition, the maximum time increment should be less than 1/20 of the excitation frequency (Moser, Jacobs et al. 1999), thus, the simulation time step was defined as 0.1 μs. The boundary of the pipe was free. The excitations were different, which was a 120 kHz 10-cycle sinusoidal signal operated by Hanning window in

paper (Xu, Luo et al. 2019). Figure 28 illustrated the results comparation in paper (Xu, Luo et al. 2019) and the simulation model in this study, where showed the excitation traveled through the pipe, and reflected from the defects and the boundary. The first packet of each signal was represented the initial wave. Then, reflections of these two signals were similar located around 6e-4 s, and the third packets was located around 8e-4 s, suggesting the echoes from the damages and the boundary. The wave packets had the similar locations and shapes which represented the simulated model was certificated. Note that the different parameter of the excitation can cause the different amplitude of the signals and the multiple reflection of the wave on damage and boundaries can cause the superposition of waves, resulting in an increase of the cycles in the boundary wave packet. The comparison results verified the simulated model established in this study was proper for the guided wave simulation in pipes, thus, the further exploration was based on this simulation to generate data.

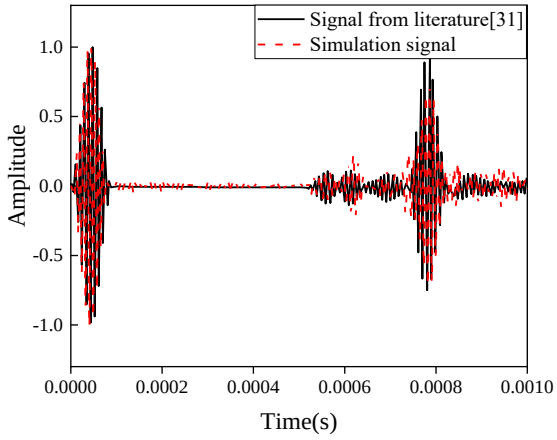

Figure 28. Comparison of the results.

In this section, a steel pipe model was established in FE method, which has been already verified by the literature and dispersion curve. The model in following research was derived on the basis of this model, which just changed the length, added weldment part and more damage states.

In order to gather more general results and reduce the influence from the geometric parameters, all the parameters were set as a multiple of the outer diameter of the pipeline, including the length of the pipe, the dimensions and the location of the defect. The outer and inner diameters, D_{out} and D_{in}, were 76 mm and 68 mm respectively. The length of the pipe was 1520 mm which was equal to 20 * D_{out}. Figure 29(a) and (b) were shown the details of the pipe, where the excitation nodes were set at the left side and four receivers were circumferentially symmetrical located at position A (15mm away from the left side). Notch-shaped damage and weldment were added on the pipe located at the point B and C respectively. The butt weldment was designed as a V-shape cross section, the weld width at outside and inside surface were 10 mm and 5 mm respectively, and the thickness was 4 mm higher than that of pipe, shown in Figure 29(c). The material welding filler was Ti-6Al-4V. In detailed, the density of this material is 4453 kg/m3, Young's modulus is 125.8 GPa, shear modulus is 40 GPa and Poisson's ration is 0.40. Due to the complicate damages, the excitation was 5-cycle sinusoidal signal operated by Hanning window in 100 kHz.

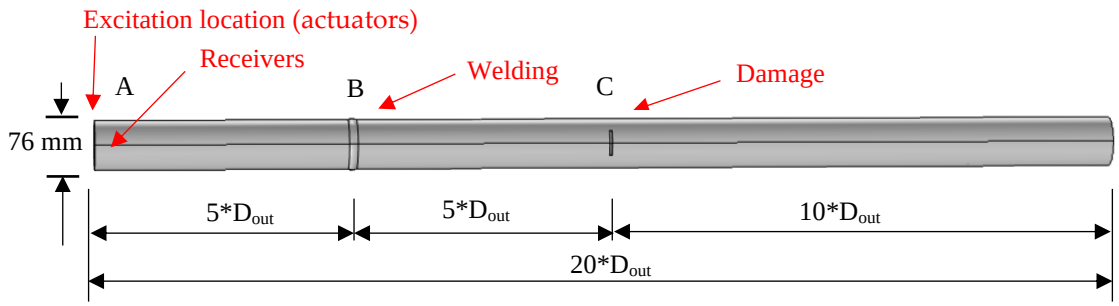

(a) Steel pipe

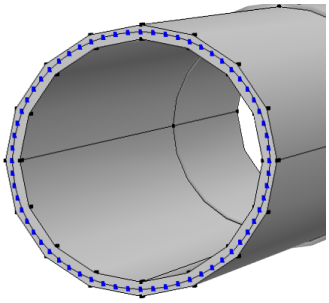

(b) Excitation nodes

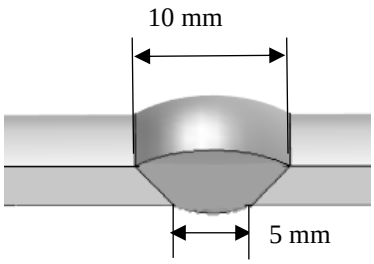

(c) V-shaped weldment

Figure 29. The pipeline model with notch-shaped damage and weldment.

The experiment was setup to verify the proposed finite element model, as shown in Figure 30. The digital excitation was generated from the wave generator. Piezoelectric actuators transferred electric signals into mechanical ones and the wave propagated though the pipeline. The echoes were collected by another sensor and displayed on signal collection machine.

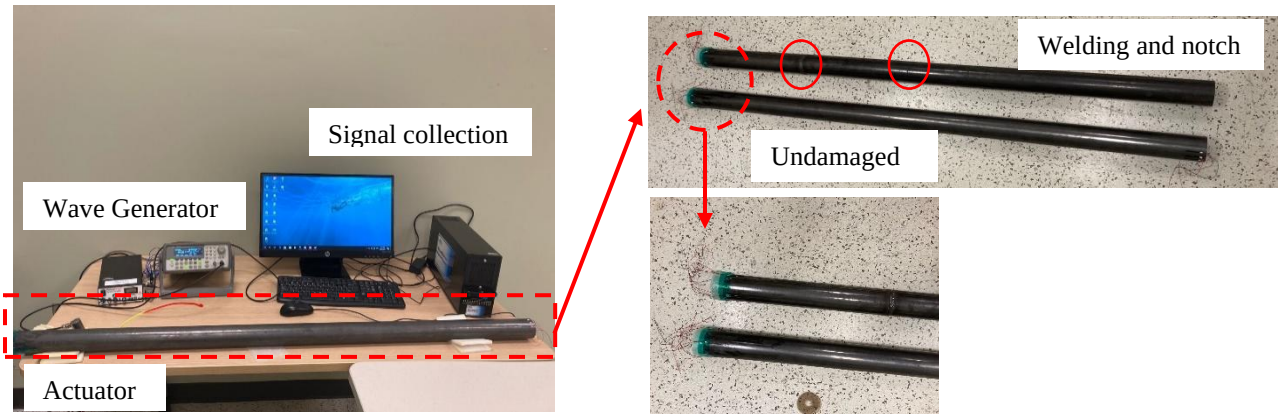

Figure 30. Experiment setup.

Figure 31 shows the comparison of the results in simulation and the experiment. Clearly, under undamaged state, two main wave packets represent excitation and boundary reflection, as shown in Figure 31(a). In the experimental result, the excitation signal has more wave numbers because several actuators work together to send signal into the pipe. However, the sticking position of sensors was not exactly same, resulting the original waves cannot be completely coincident and more scatters in the signals. The Figure 31(b) represents the pipe with welding and a notch damage. In detail, two echoes are clearly shown in the middle part of both signals. The reflection from the right boundary in simulation also has the similar location with the experiment. Note that the amplitude of the echoes is not same, the reason is that the energy of the signals is easier to dissipate due to external factors, such as the sensor bounding is not tight enough, and the glue absorbs part of the energy.

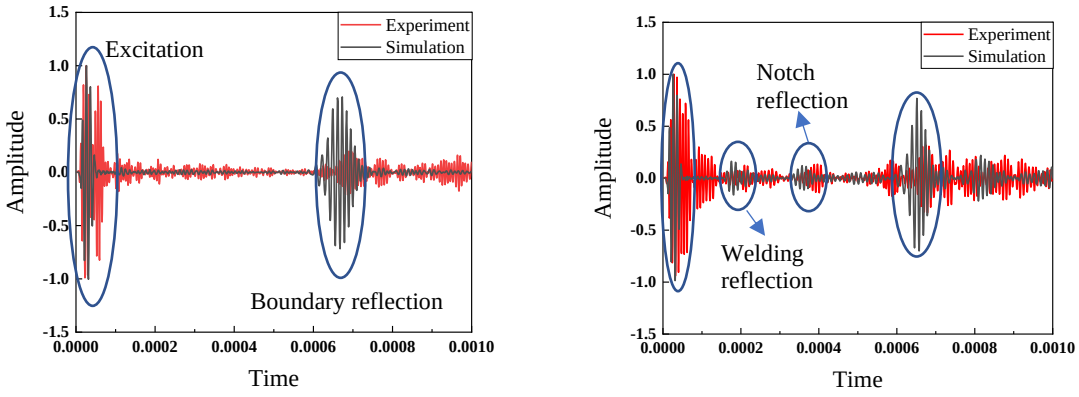

Figure 31. Calibration of experiment and simulation: (a) Pipeline with undamaged state; (b) Pipeline with welding and notch.

4.2.2. Characteristics of Ultrasonic Guided Waves

The signal characteristics of a pipe with and without weldment was displayed in Figure 32(a)-(d), where for a comparison, mechanical damage, such as cracking, was also included in a pipe. The excited ultrasonic waves that traveled through a pipe with and without weldment echoed when it reached discontinuity due to weldment or mechanical damage and boundary under

different scenarios. In order to clearly see the reflection packet, the envelop of the wave was plotted in red line as shown in Figure 32. As illustrated in Figure 32(a), an intact pipe only contained two main packets, where the first signal packet presented the excitation and the second packet collected represented the echoed wave from the boundary. With the wave speed and travel time, one could accurately determine the length of the pipe if needed. Differently, Figure 32(b)-(d) reveal enriched echoed waves within and outside of the boundary echo when a pipe experience certain structural nonlinearity or discontinuity.

Figure 32(b) exhibited the resulting waves of a pipe with a girth weld. Besides two dominant packets as identical to the intact pipe shown in Figure 32(a), one could also observe low-amplitude oscillations experienced within and outside of the boundary echo due to the weldment reflection. Such characteristics is often used for data classification.

Figure 32(c)-(d) exhibited the feature of the guided wave signals associated with varying types of mechanical damage or combined weldment with damage. These waves exhibit apparently non-stationary and nonlinear behavior. Figure 32(c)-(d) revealed that, with the more complicated scenarios, including mechanical damage or combined weldment with damage, the received signals came from the complicated scattering, reflection, and wave interaction.

Physics-based methods are based on physical characteristics of the guided waves that are often interpreted under frequency-, time-, or time-frequency-domains. In time domain, physics-based features play an important role in ultrasonic wave feature extraction. Amplitude, energy, and correlation coefficient are three features which can represent the wave characteristic. The amplitude was obtained by the peak value of the damage wave packet. The energy calculated by the root mean square of wave (RMS) in the damage part were defined as

$$\mathrm{RMS} = \sqrt{\frac{1}{n}\sum_{i=1}^{n} e_i^2} \tag{48}$$

where n is the number of data point and e_i is the signal. The correlation coefficient under the damage state was used to compare with that of the health state. In frequency domain, the amplitude was extracted as the features.

As stated in the literature, amplitude, frequency, or RMS that often result in good classification for signal characteristics may perform poorly, for example, when received signals after coupled scattering and reflection/refraction behaved highly nonlinearly, with high level of noise. Despite great efforts in physics-based methods on damage detection and classification, these methods could be hindered by high variance of structures due to uncertainty, measure noise, and other interferences. Thus, the data-driven methods, such as deep learning, was introduced to tackle this issue as presented in Section 4.3.

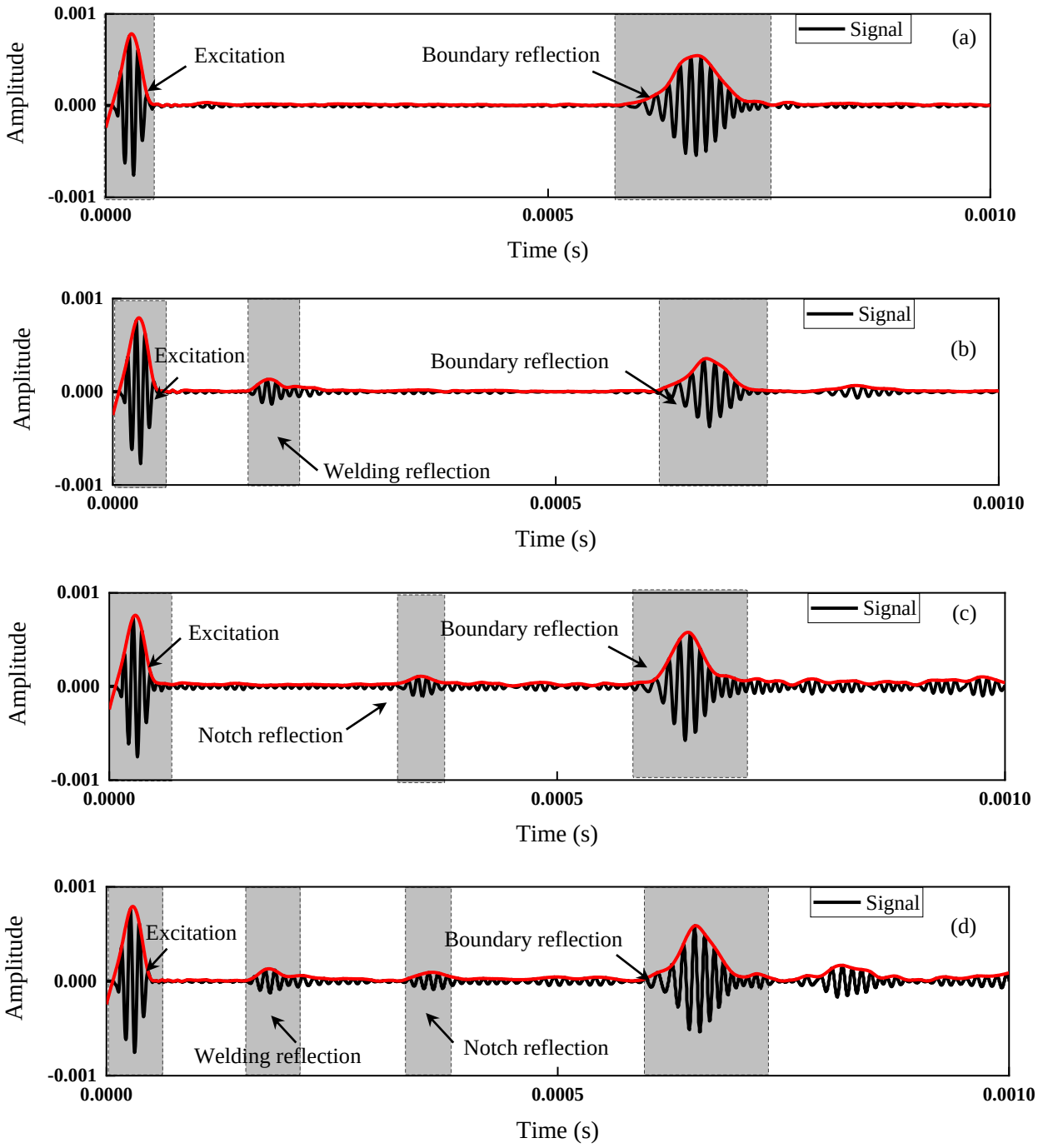

Figure 32. Signal characteristics under varying mechanical damage integrated with weldment: (a) intact pipe; (b) pipe with grith weld; (c) pipe with crack; and (d) pipe coupled with weldment and mechanical damage.

4.2.3. Design of Scenarios and Data Augmentation

4.2.3.1. Design of scenarios

The welding manufacturing process can cause the impurities leaving in steel structures, resulting in material discontinuity. Four main welding defects were designed in this research, including lack of fusion, cracks, undercut and lake of penetration, as Defect 1 to 4 shown in Figure 33. Contaminated surfaces prevent the welding bead from adhering and fusing with the base metal, resulting in lack of fusion defects in welds. Cracks occur if the weld metal shrinks as it solidifies. The undercut is the weld reduced the cross-sectional thickness of the base metal. When the filler material does not fully fill into the joint, lack of penetration defects appears (Alobaidi 2017). Three different severity levels were design for weld defects, accounting for 10%, 5% and 1% of the circumference, respectively.

In addition to the welding part, the pipeline itself was also suffered from load and environmental erosion. Hence, the notch-shaped damages of different positions were considered in the research, representing minute cracks with the width of around 10^{-4} m. The damage depth was 4mm and the length was $0.1*D_{out}$. The damage locations were ranged from $0.5*D_{out}$ to $10*D_{out}$.

A total of 25 different states were obtained, separating into 4 Cases to investigate the effectiveness of the proposed method. The reference state (State #1) was a pipe with a health welding and without damage. In Case 1, the crack location was detected in the pipeline with health welding (State #2-6). Case 2 was also identified the crack damage location in the pipeline with welding defect interference (State #7-11). The crack, a notch-shaped damage, was located at 5 different positions, including $0.5* D_{out,}$ $1* D_{out,}$ $2* D_{out,}$ $5* D_{out,}$ $10* D_{out}$. Case 3 (State #10, 12-14) was focused on identifying the 4 kinds of welding defects with the certain severity (1% of the circumference). The detection of welding defect severities was carried out in Case 4 (State #10,

15, 16) where had lack of fusion defects in the welding of the pipeline. In order to consider the noise inevitably mixed in the detection signals, all the states were interference by additive white Gaussian noise with the SNR equal to 60 dB to 100 dB. The detail information was demonstrated in Table 7.

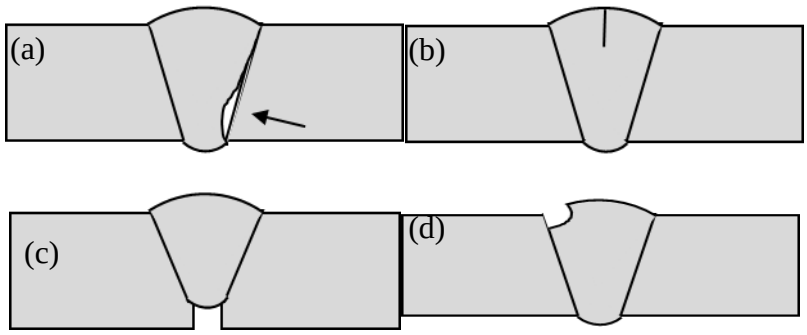

Figure 33. Welding defects (a) Lack of fusion; (b) Cracks; (c) Undercut; (d) Lack of penetration.

Table 7. Test matrix for computation modeling.

Case	State	Notch-shaped Damage location	Welding Defect type	Severity of welding defect	Noise Interference
Case 1	State #2-6	0.5* D_{out} ~10* D_{out}	/	/	60dB ~ 100dB
Case 2	State #7-11	0.5* D_{out} ~10* D_{out}	Defect 1	1%	
Case 3	State #10, 12-14	5* D_{out}	Defect 1~4	1%	
Case 4	State #10, 15, 16	5* D_{out}	Defect 1	1%, 5% 10%	

The results in Figure 34(a)-(f) were indicated the details of guided waves propagated and diffracted through the whole span of pipeline during different periods. Taking the State #5 as an example, the excitation wave was input from the left side and traveled to the right. When the signal interacted with the weldment at 1E-4 s, part of the wave was return, and the rest was continually moving forward. At 1.8E-4 s, the initial wave was interfaced by the notch-shaped damage, and on the other side, the echoed wave was arrived at the left boundary due to the same distance. On the

meanwhile, the echo was received by the actuators and keep propagating to the right. As the original wave traveled back to the left boundary (at 3.2E-4 s), the wave completes an entire propagation in the pipeline, experiencing the reflection from damage and weldment for several times. Therefore, the detection signal included multiple wave packets because the initial wave packet was experienced several times reflections and scattering.

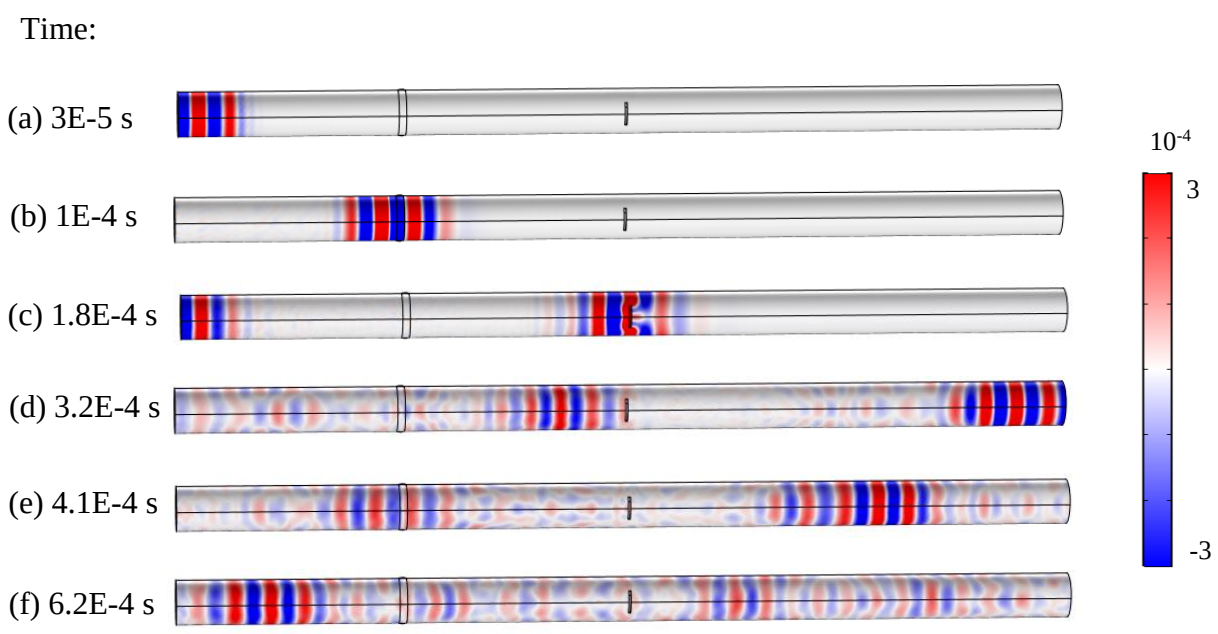

Figure 34. Wave propagation through the whole span. (a) ~ (f).

The data received by sensors was much easy to be contaminated by noise from the environment. As such, appropriate noise added to the collected signal could consider the real situation in the lab. Signal to noise ratio (SNR) represents the ratio of the signal strength to the background noise strength noise levels ranged from 100 dB to 60 dB have been added in State # 1-16 for forming multiple synthetic signals. Furthermore, classifying signals in different noise levels can check the sensitivity of the deep learning method to the uncertainty caused by noise. Taking the signal in State #5 as an example, Figure 35 represented the waves under different noise levels. Figure 35(a) showed the initial signal generated by numerical simulation. Clearly, several wave packets were representing the echoes from damage or boundary. With the SNR reduced, the

signals were contaminative seriously. Especially at 60 dB, the features of the signal were covered by noise.

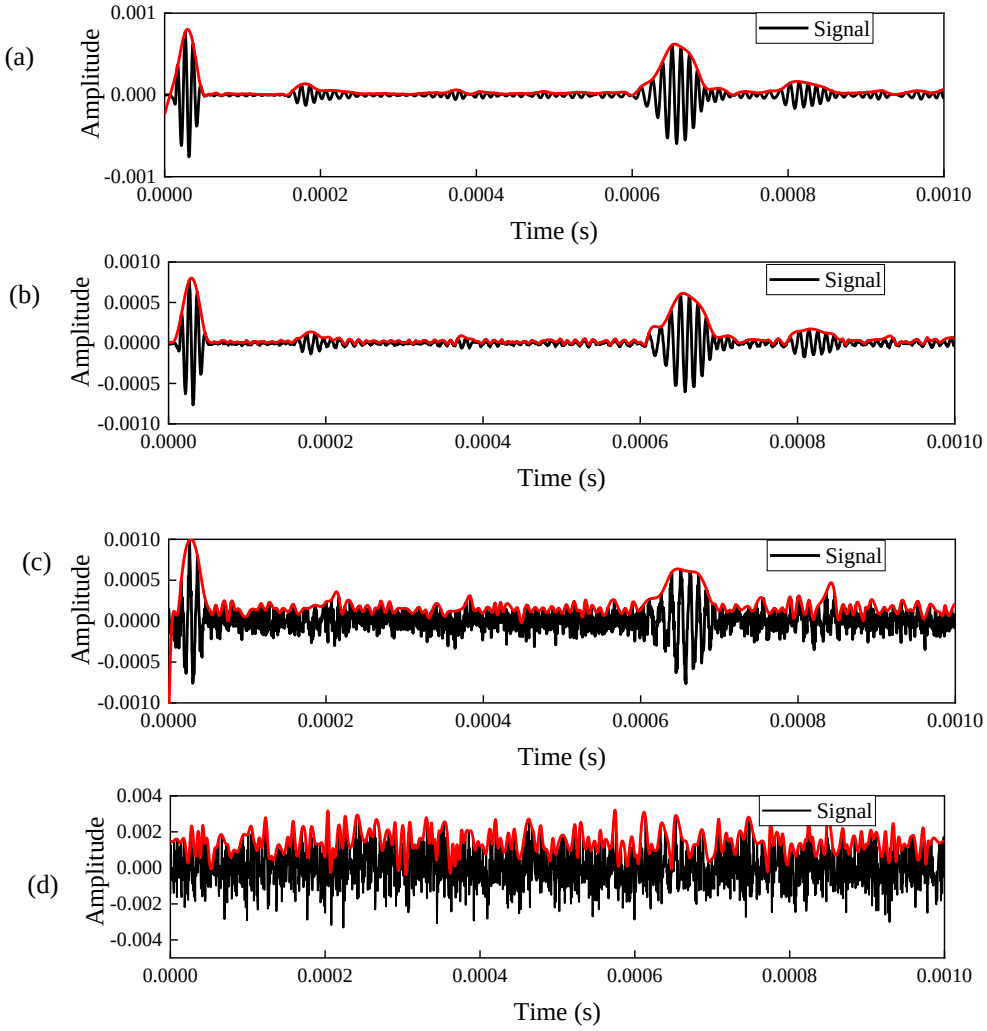

Figure 35. Signals with different noise levels. (a) Original signal; (b) SNR = 100 dB; (c) SNR = 80 dB; (d) SNR = 60 dB

4.3. Deep Learning-based Damage Detection

Convolutional neural network was involved to identify the damage in the pipe by guided wave. As illustrated in Figure 36, the learning framework was consisted by three main parts, including dataset collected by the simulation and data augmenting method, Training CNN models by training set and modifying by validation set, and predicting the testing data formed by CNN models. Specifically, the guided wave dataset simulated by finite element method was enlarged by

adding Gaussian white noise with different SNRs. The classification label was defined by the state that each guided wave belongs to. Then data partition was involved in this process, which 70% of the data for training, 15% for the validation and 15% used to test. The prepared training data was input into the CNN model to establish a classifier for identify the damage state of each signal. The CNN model was modified when the classifier operated on validation data. Training and validating were necessary parts for the CNN model to build and improve the sensitivity of feature learning and the performance of classification. Finally, the testing set was classified by the trained CNN model. Therefore, the damage state of each guided wave was predicted by CNN.

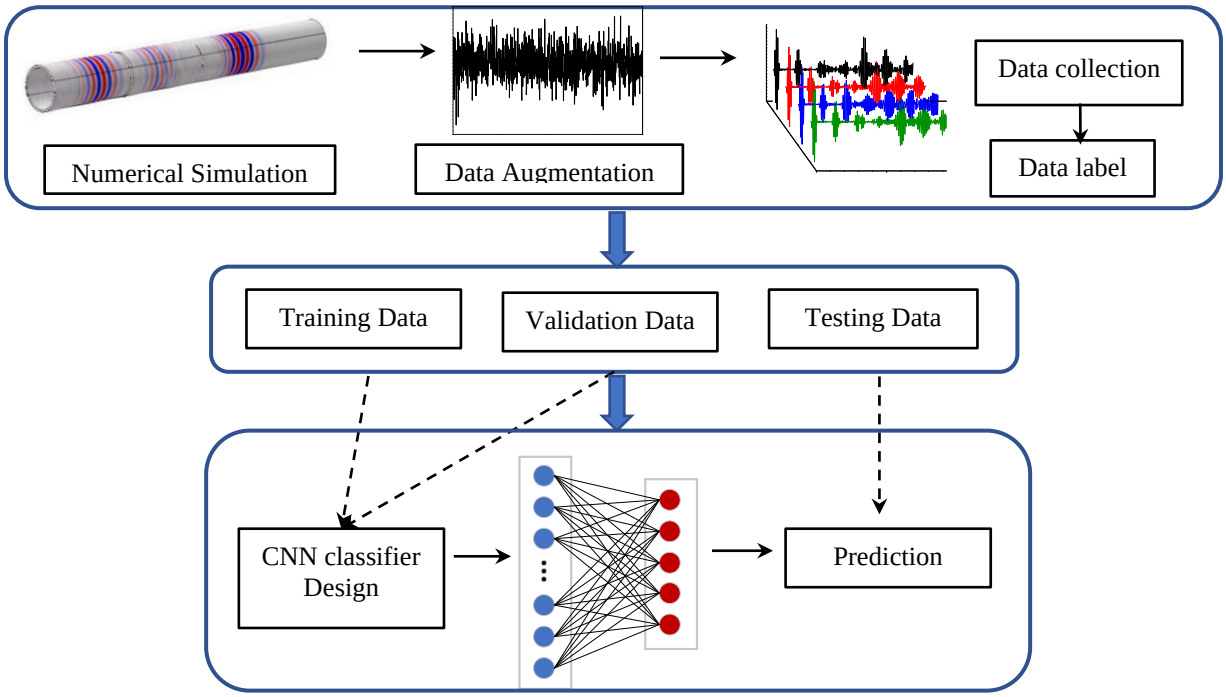

Figure 36 Flowchart for the damage detection by CNN.

4.3.1. CNN Architecture

CNNs compose of layers containing artificial neurons which are arranged in three dimensions including width, height and depth (Umakanth 2018). In this damage detection study, the input was consisted by 4 guided waves, which is a two-dimensional matrix sized 2000×4.

Stepping through each layer of the CNN, the matrix is converted into a one-dimensional vector corresponding to the category. Figure 37 illustrated the whole process of CNN. Three main layers were involved in CNN architectures, including the convolution layers, pooling layer and the fully connected layer.

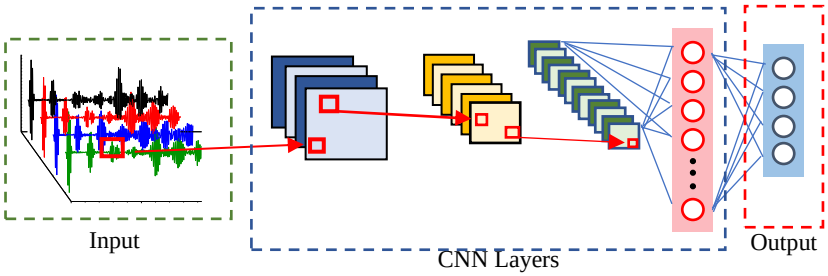

Figure 37. Flowchart for the damage detection by CNN.

4.3.2. Convolutional Layer

Convolutional layer is the main part in CNN. Each convolutional block was contained the learnable parameters such as weights (filters) and biases. Comparing with the input, the width and height of the filter is spatially smaller, but the depth is the same. The feature maps from previous layer were convolved with filters and formed the output through the activation function. The formula of the convolutional layer for a pixel is

$$C_{xy} = \sigma(\sum_{i=1}^{h}\sum_{j=1}^{w}\sum_{k=1}^{d} f_{ijk} * \boldsymbol{X}_{x+i,y+j-1,k} + b) \quad (49)$$

where h and w are the size of filter and d is the number of channels of the input, b is the bias vector, σ is the activation function, and $\boldsymbol{f}$ is the weight matrix.

Figure 38 showed the convolution operation on a 4×4 matrix. A 3×3 matrix was acted as the filter which was generated randomly at initial state and updated from the model by the backward propagation algorithm. The stride is equal to 1, thus four subarrays, having the same size as the filter, were generated by sliding along the width and height of the input matrix. Each subarray multiplied with the filter matrix element by element. Then, the output value was formed

by the sum of the multiplied values and the bias. The size of the output was smaller than the previous layer because of the stride.

After the convolution layer, a nonlinear activation function was followed, which was used for introducing non-linearity into the network. Two of the most commonly activation functions used in neural networks are rectifier linear unit (ReLU) and softmax. The function of ReLU and Softmax are expressed as follow

$$f(x) = \max(0, x) \tag{50}$$

$$f(x)_i = \frac{e^{xi}}{\sum_{j=1}^{K} e^{xj}} \tag{51}$$

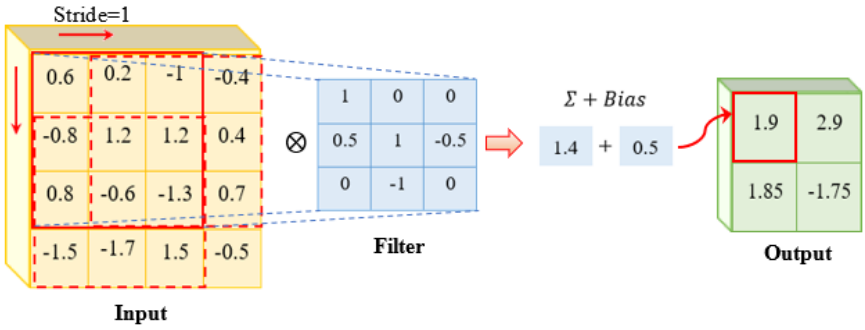

Figure 38. Convolutional layer.

4.3.3. Pooling Layer

The pooling layer was used to reduce the spatial size of the feature maps to speed up the computation and increase the robustness of feature detection. The most common way were max pooling and average pooling. In max pooing, the maximum value in filter area was chosen as the output, shown in Figure 39. In detail, the input layer, a 4×4 matrix, was operated by the max pooling filter which sized 2×2. The stride was designed as 2 which means the next filter should move two elements to the right or down. Then, dimension of the output was declined into 2×2, and the value was the maximum elements in the response field. As the average pooling, it took the average value in filter area.

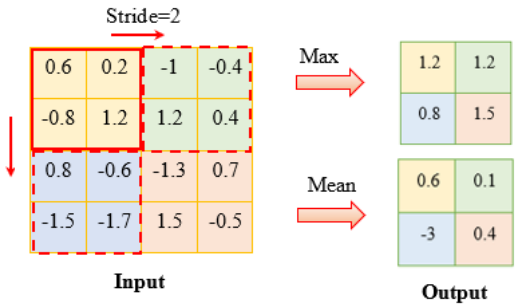

Figure 39. Pooling layer.

4.3.4. Fully Connected Layer

Fully connected layer is the one before the output layer of the whole network. In this layer, all the neurons are connected with the features generated by the previous layer. And weights and biases in this layer converted the feature into the correspondent categories. The equation of the output y^l is shown

$$y^l = \sigma(y^{l-1} * \boldsymbol{w} + \boldsymbol{b}) \tag{52}$$

where, $\boldsymbol{\sigma}$ is the activation function; $\boldsymbol{w}$ and $\boldsymbol{b}$ represent the weights and bias vectors in this layer.

4.3.5. Analyses of CNN Parameters

The 8-layer CNN architectures derived from LeNet (LeCun, Bottou et al. 1998) were proposed in this section. In detail, 8-layer CNN configurations for guided wave-based damage detection included 3 convolution layers, 2 max pooling layers, one full connected layer, rectified linear unit (ReLU) and sigmoid function (Softmax). The important parameters of the CNN architecture were discussed in this section, including the convolutional filter size, number of convolution filters and the parameters of pooling layers. The networks were trained by the guided wave collected from State #2, 12-15 in Table 7 to classify the 6 different damage location in pipe. An overall of 3000 data was enlarged by adding Gaussian white noise with 500 in each state. The size of each wave was 2000×4. The whole samples were split into training set (60%), validation set (20%) and testing set (20%).

4.3.5.1. Size of convolutional filters

The convolutional filters represent the local features of the input signals. The appropriate size (the width and the height) of the filters can represent the typical features of signals and improve the efficiency of CNN. Since the width of the example signals were small, only the heights of the filters in the first two convolutional layer were considered, setting from 5 to 45.

Table 8 reported the results of the training under different noise level. When SNR was equal to 70 dB, the classification was 100% correct by these 5 groups. With the noise increase, the accuracy of the prediction was drop down. As the size of the first two filters increased, the testing error was decreased to 0.83% at Group 3 and then increased under 65 dB. The similar situation was happened at SNR equal to 60 dB, which the lowest testing error was emerged at Group 3 (about 17%). As such, the filter sizes shown in Group 3 was used in convolutional layers for further study. Figure 40 illustrated the weights of the third convolutional layer from Group 1 to 5 at 60 dB. The channel represented the number of filters and the dimension was the length of the filter. After training by two convolutional layers, the third one could better reflect the features learned from the input. Obviously, in 5 distinct groups, the fluctuations of each feature vector were gradually changed. The weight distributions in Group 1 and 2 were uniform, thus the features were hard to extracted. In Group 3 to 5, the distributions of weights were different, however, Group 3 showed the most notable features which means the architecture made this network well trained.

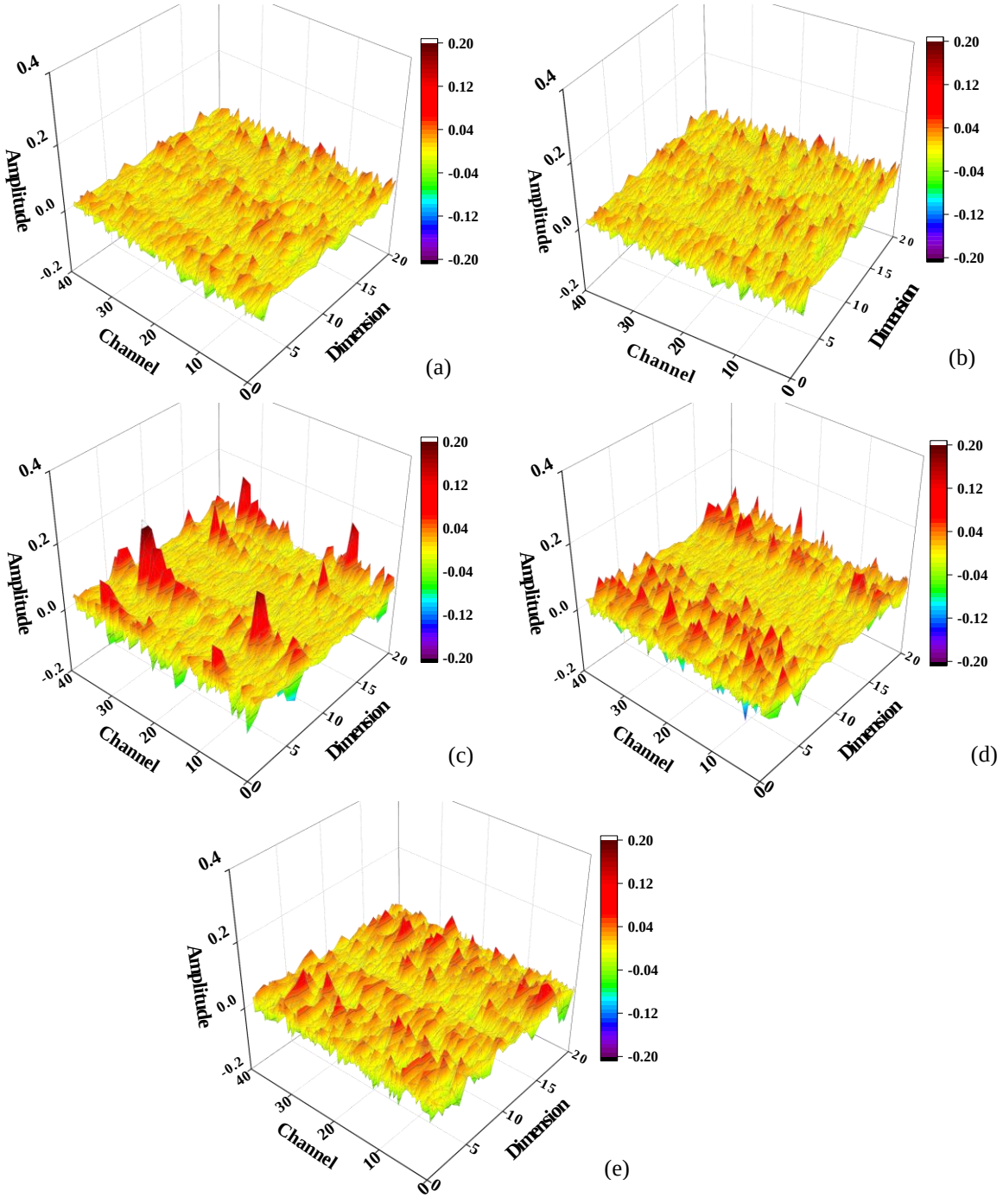

Figure 40. Weights of the third convolutional layer at 60 dB.

Table 8. Results of different filter sizes.

	Filter size of the first convolutional layer	Filter size of the second convolutional layer	Filter size of the third convolutional layer	Testing (70 dB)	Testing (65 dB)	Testing (60 dB)
Group 1	5*2	5*3	5*1	100%	95.33%	61.00%
Group 2	15*2	15*3	5*1	100%	94.83%	75.33%
Group 3	25*2	25*3	5*1	100%	**99.17%**	**82.83%**
Group 4	35*2	35*3	5*1	100%	98.67%	78.17%
Group 5	45*2	45*3	5*1	100%	97.67%	79.83%

4.3.5.2. Number of convolutional filters

The number of the filters determined the quantity of the feature map generated in this layer which made it possible to extracted features much more fully. As the network deepened, the length and width of the feature map shrank, indicating that the features extracted in this layer were much more representative. Obviously, too few filters cannot achieve the demand of feature extraction, and too many filters lead to time wasting. The classification results were listed in the Table 9. The classification in 5 groups were compared under different noise levels. Under lower noise level, the number of filters in each layer had less impact on classification accuracy. However, when noise level increased, the filter number proposed in Group 3 showed better results, achieving 99.17% and 82.83% under 65 dB and 60 dB respectively.

Table 9. Results of different filter numbers.

	Number of the first convolutional layer	Number of the second convolutional layer	Number of the third convolutional layer	Testing (70 dB)	Testing (65 dB)	Testing (60 dB)
Group 1	10	20	10	100%	96.67%	74.83%
Group 2	15	30	15	100%	92.17%	73.50%
Group 3	20	40	20	100%	**99.17%**	**82.83%**
Group 4	25	50	25	100%	98.00%	81.50%
Group 5	30	60	30	100%	98.00%	78.67%

4.3.5.3. Parameters in pooling layer

The pooling layer, also known as the downsampling layer, aims to reduce the dimension of the feature maps, while remaining the most representative information in the region. In addition, the pooling layer also prevents overfitting to some extent. Larger size can cause the feature loss; however, smaller size lost the properties of dimensionality reduction. Besides, the type of pooling layer should be designed before building the entire structure of CNN. Two pooling layers were involved in the CNN architecture. 6 distinct combinations including different sizes and types were designed inhere attempting to explore the relationship between pooling layer and the accuracy of prediction. From the results shown in Table 10, the predictions using max pooling were better than that of mean pooling for this dataset. Meanwhile, the parameters of two pooling layers set as Group 3 could achieve better results, at 15 and 8 for the first and second pooling layer respectively.

Therefore, the detail information of the proposed CNN framework was shown in Table 11. The adopted network had an input layer which the 4 received signals (sized 2000) were combined and directly sent into the framework. Then the first convolutional layer which the filter size was 25×2 and max pooling layer were operated the signals into 393×3. Following was the second

convolutional layer with 40 filters sized 25×3 and max pooling layer which reduced the signal into just one dimension (73×1). The third convolutional layer which the filter size change into 5×1, then the full connected layer and softmax layer worked together to map the result into a 4×1 matrix. Totally, nearly 5000 parameters were generated in this network.

Table 10. Results of different Pooling sizes.

	Size of the first pooling layer	Size of the second pooling layer	Type of pooling layer	Testing (65db)
Group 1	10	5	max	98.67%
Group 2	10	5	average	91.00%
Group 3	15	8	max	**99.17%**
Group 4	15	8	average	98.00%
Group 5	20	10	max	93.5%
Group 6	20	10	average	68.5%

Table 11. Detail of the proposed CNN.

Name	Filters	Filter size	Stride	Bias	Output layer size
Input layer	--	--	--	--	2000×4
Convolutional layer (C_1)	20	25×2	1	20	1976×3
Max pooling layer (P_1)	20	15×1	5	--	393×3
Convolutional layer (C_2)	40	25×3	1	40	369×1
Max pooling layer (P_1)	40	8×1	5	--	73×1
Convolutional layer (C_3)	20	5×1	1	20	69×1
ReLU	--	--	--	--	69×1
Full connected layer (F_1)	4	69*1	1	4	4
Softmax	--	--	--	--	4

4.4. Results and Discussions

4.4.1. Classification Performance for Case 1 and 2: Detection of Notch-shaped Damage Location

4.4.1.1. Training and validation results of notch-shaped damage location

The 8-layer CNN proposed in this paper was used to identify the location of damage on the pipeline, which was trained by 3000 records of guided wave signals collected from State#2-6. The pipeline was excited by the 100kHZ 5-circle sinusoidal signal modulated by Hanning window. Gaussian white noise with 5 specific levels were added to the signals to investigate the sensitivity and effectiveness of the method interfered by noise. The dataset was partitioned into training, validation and test set with 60%, 20% and 20% respectively. Figure 41 demonstrated six categories' feature maps obtained from the last convolutional layer of CNN model in 100 dB and 60 dB. The dimension was the length of the output and each line illustrated the channel of the output. Specifically, from visual demonstrations of the output, the shape of feature maps was more obvious to distinguish the status of the pipeline when SNR was 100 dB. For instance, in the first label, there main wave peaks were revealed after 6 layer's training. In the second label, 4 main wave peaks occurred with different values. Analogously, the six labels substantial display the characteristic of themselves which become susceptible to passing through the last fully connection layer and obtaining the final probability of each category. However, in 60 dB, the feature maps became messy, representing the model was hard to extract the sensitive features from the detection signals in this condition. Although this was not the final result of the classification, the fully connection layer was difficult to achieve the reasonable ratios of each category. As a result, the accuracy of CNN classifier would be lower when noise level was higher.

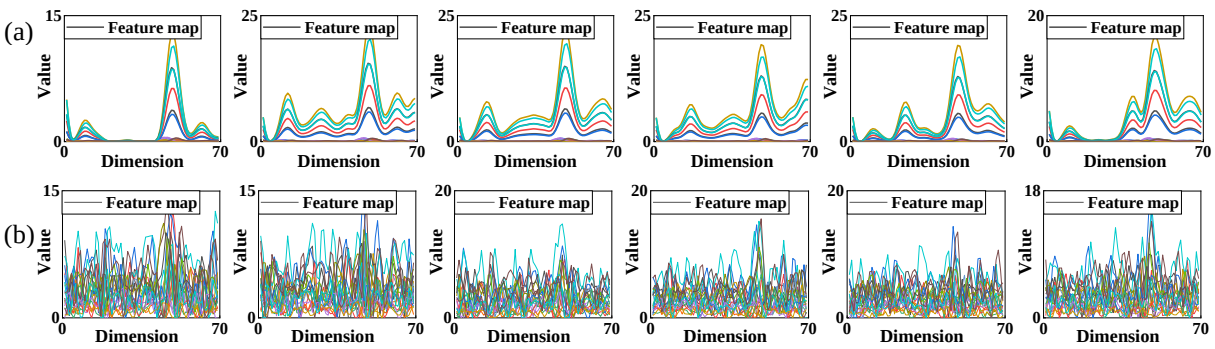

Figure 41. Feature maps. (a) SNR = 100 dB; (b) SNR = 60 dB.

The training and validation errors under 80 dB ,70 dB and 60 dB were plotted in Figure 42. In Figure 42(a), the model extracted the information rapidly at 80 dB, which error rates were changing from 0.85 to 0 after 10 epochs. With the noise level increased, the accuracy of classification was decreased. When SNR was 70 dB level (shown as Figure 42(b)), the training error was changed slightly at the first 10 epochs time, and then the error rate dropped sharply spent 20 epochs of training from 0.8 to 0.02. At the 23rd epoch, the training error was tent to 0, which took more than 2 times computation comparing with the situation in 80 dB. Meanwhile, the tendency of the validation error was similar as the training error, except that the rate converged to 0.12 not 0 after 20 epochs training. It means the classification model could not entirely identify the damage location correctly under this noise level. In 60 dB, the classification was deteriorated where the validation value was just close to 0.7 after 100th epoch, demonstrated in Figure 42(c). It has been confirmed that noise interference had a great effect on the CNN classifier when it identified the damage location.

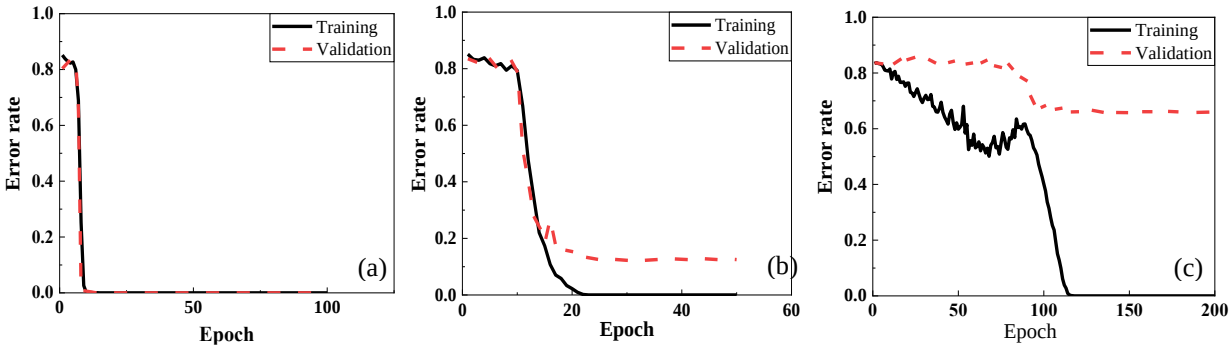

Figure 42. Training and validation results: (a) SNR = 80 dB; (b) SNR = 70 dB; (c) SNR = 60 dB.

When the weld damage and material discontinuous were happened at the same time, the detection by ultrasonic guided waves was become complicated, especially distinguished by traditional way. Six different damage states (Case 2) in Table 7. Test matrix for computation modeling were consisted as the training dataset which contained 3000 data points. When the noise level higher than 70 dB, CNN model trained 100% correctly in 10 epochs from the training and validation sets. At 70 dB, the error rates were declined dramatically in 10 epochs time, then, training error was closed to zero and validation error was equal to 0.04 after 15 epochs' learning, as shown in Figure 43(a). With the noise level increased to 60 dB, CNN classifier spent 100 epochs time to reduce the training error rates from 0.83 to 0, taking 10 times longer than that of 70 dB, while the validation part only converged to 0.32. The main reason for this should be the input data was hard to identify because of the high noise.

(a)

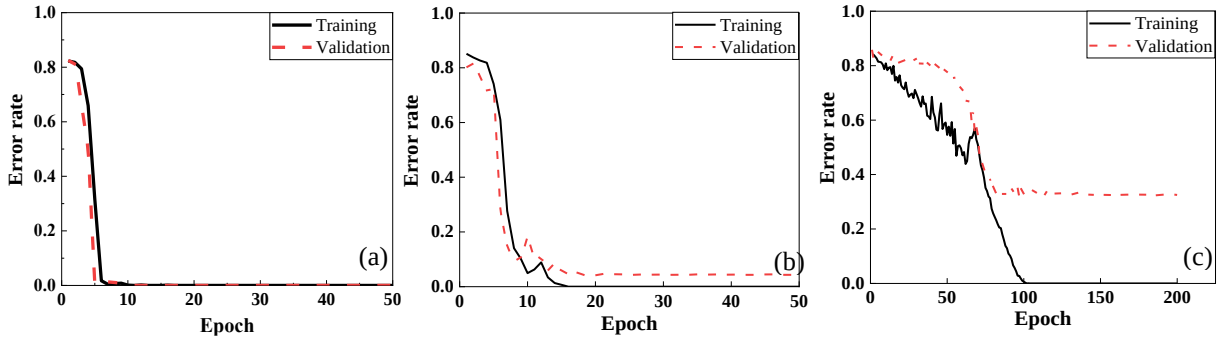

Figure 43. Training and validation results: (a) SNR = 80 dB; (b) SNR = 70 dB, (c) SNR = 60 dB.

4.4.1.2. Testing results of notch-shaped damage locations

Validating the classification model by testing data, the result of notch-shaped damage position detection in Case 1 (State #2-6) were illustrated in Figure 44. 600 signals were input into the pretrained model, and the prediction result of each data was directly obtained. Obviously, the CNN method trained by a part of the signals could accurately identify the damage location in most situations, which acquired 100% classification under noise level of 100 dB to 80 dB. Figure 44(a) showed confusion matrix of the testing result in 80 dB. However, the special case was happened at 70 dB, which the accuracy of the test was decreased dramatically to 92.33%. The data in each category was misled into other categories to some extent. Specifically, 2 of the signals whose damage was located at 0.5 D_{out} from the weldment were misclassified as group 1 D and 1 of them was misled into 5 D_{out}. 11 of the samples in 1 D group were predict wrongly into other groups. The accuracy of the fifth class was only 86%, which means the prediction of 14 test signals in this class were failed. The reason of the low accuracy was that the high level of noise added to the signals replaced the most of original features with the noise features. Therefore, the classification method was ineffective when the training data was indistinguishable.

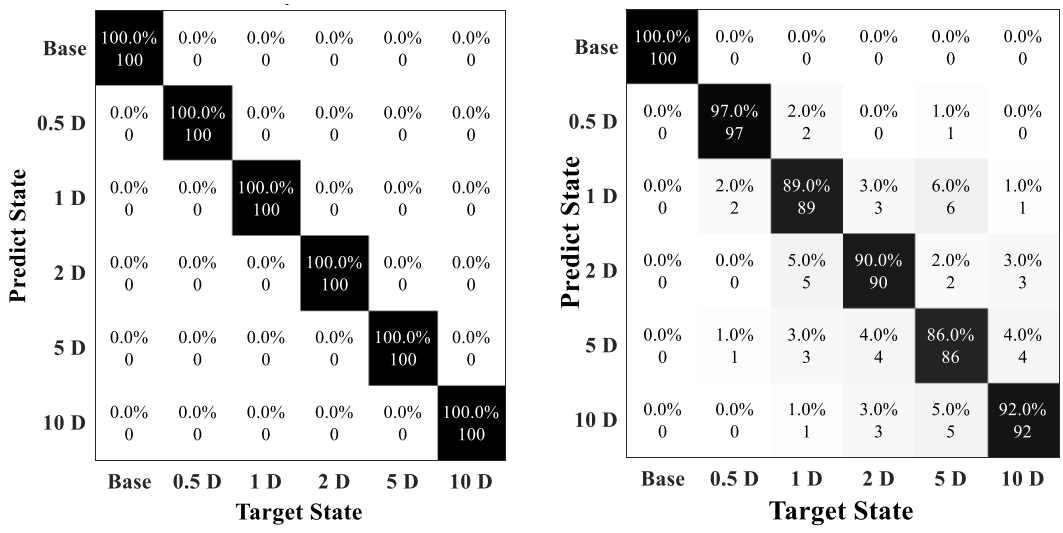

Figure 44. Testing results: (a) SNR = 80 dB (100%); (b) SNR = 70 dB (92.33%).

As the weld defect was considered to interference the identification of damage locations, the testing results was shown in Figure 45. The classification was 100% correctly when SNR was larger than 70 dB. At 70 dB, 95% of the data could be predicted into right labels which the misleading was mainly happened in position 5 D and 10 D, as 88% and 84% respectively. As noise level increased to 60 dB, the accuracy only reached to 68%, which the worse cases were the damage located at 5 D and 10 D away from the welding defect, with 54% and 40% respectively. In base state, the prediction was 92% and when notch-shaped damage located in 0.5 D, 1 D and 2D, the predictions were 75%, 71%, and 76% respectively. More misclassifications occurred under this noise level. For instance, 31 data points in 10D group were classified into 5D, and 29 data points were classified into 0.5 D, 1 D and 2D. Due to the multiple relationship between notch-shape defect and weld position, the waves were much easier to interact which made it more difficult to extract features. In addition, noise is one of critical factors affecting the accuracy of prognosis.

The accuracies of classification in each category under different noise level were illustrated in Figure 46. Comparing these two conditions (classifying the notch-shaped damage location without or with the welding defect existed), the predictions could entirely classify the categories under 80 dB, 90 dB and 100 dB. The misclassifications appeared at 70 dB and 60 dB. Note that the classification between damage and undamaged state were 100% in the first situation, as shown in Figure 46(a). Clearly, the addition of the welding defect did not affect the efficiency of the classifier, instead, the result is slightly better, because the additional of weld defect increases the complexity of the signal and allows more features to be extracted.

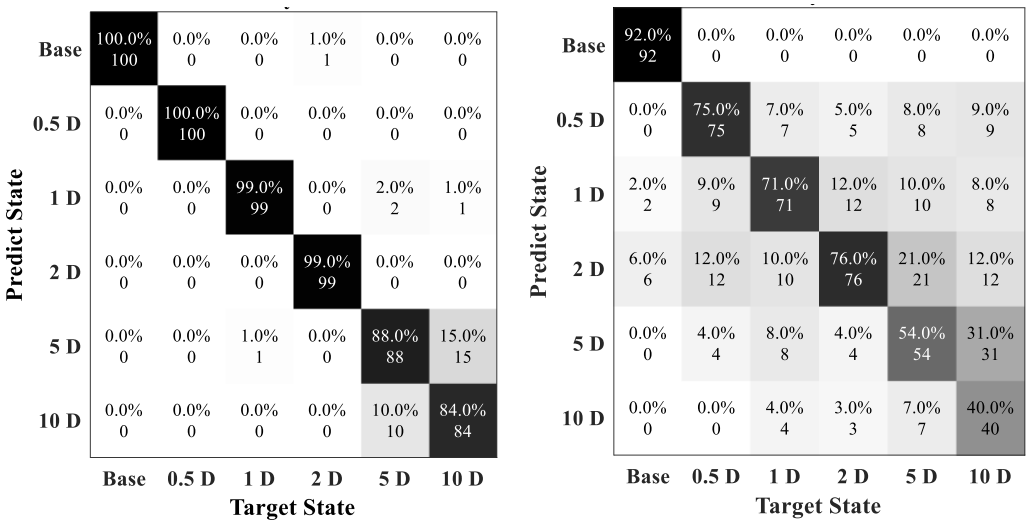

Figure 45. Testing results: (a) SNR = 70 dB (95%), (b) SNR = 60 dB (68%).

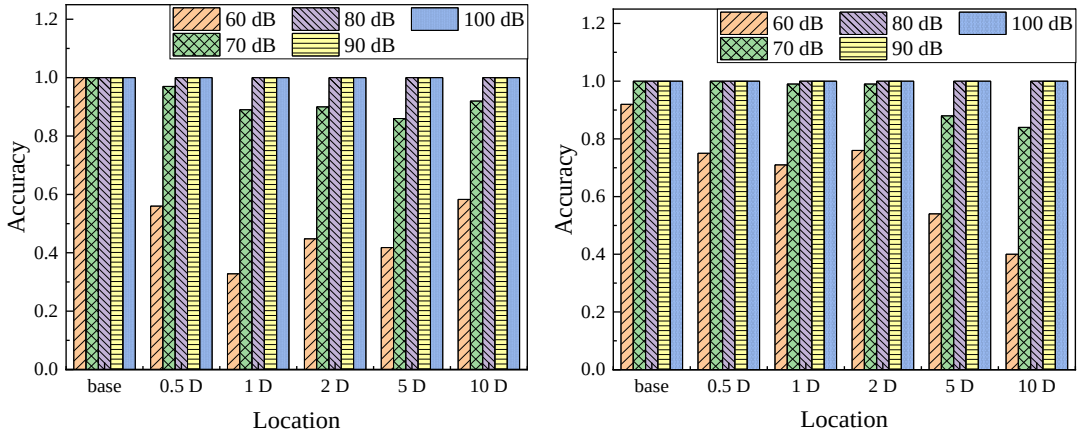

(a) Location detects without welding defect. (b) Location detects with welding defect.

Figure 46. Location identification in pipeline.

4.4.2. Classification Performance for Case 3: Detection of Weld Defect Types

4.4.2.1. Training and validation results of weld defect types

Welding defects detection is useful in various industrial applications due to the quality of the weldment plays an important role in the structure. Several defects such as lack of fusion, cracks, undercut and lake of penetration are easily formed during the manufacturing process. 4 different welding defects shown in Table 1 (State #19, 21~ 23) and the reference state (State #1) were

composed as the training set when the SNR were from 100 dB to 60 dB. The severity of the welding defects was 1% of the circumference and a notch-shaped damage was located at 5 D away from the weld. The results were illustrated in Figure 47, in which represented the training and validation accuracies under 70 dB and 60 dB. Analogously, when SNR higher than 70 dB, CNN model could learn faster and more accurate. At 70 dB, approximately 50 epochs time was cost to convert the ratios into zero. The validation ratio was equal to 0.006 after 200 epochs training. The results got worse at 60 dB, where the error curves were dropped slowly and trembled violently. Specifically, the training error had a slight decline from 0.8 to 0.5 during 40 epochs, then reached to zero after learning for 100 epochs time. The validation rate was only close to 0.21 that 21% data would be predicted into wrong categories.

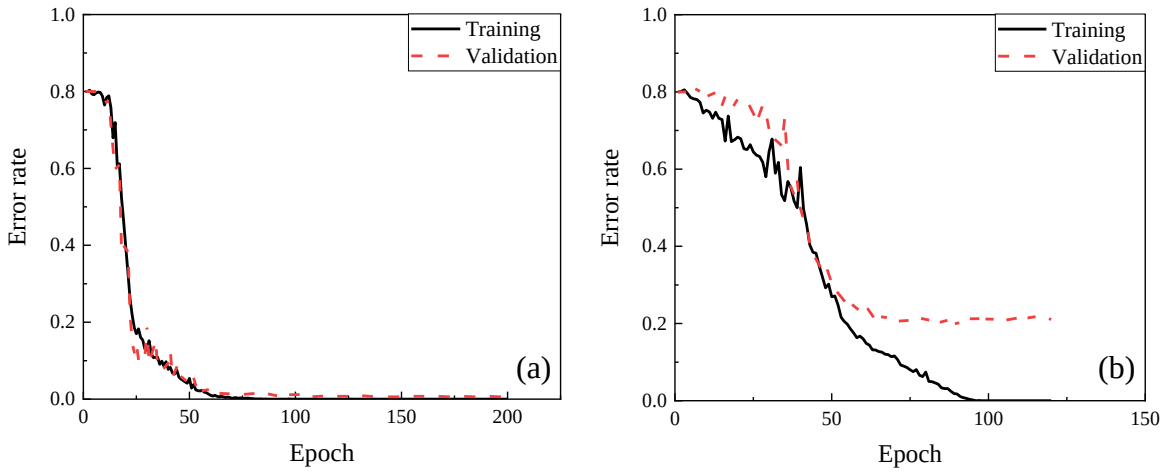

Figure 47. Training and validation results: (a) SNR = 70 dB; (b) SNR = 60 dB.

4.4.2.2. Testing results of weld defect types

The results of the damage type classification were shown in Figure 48. The confusion matrices were illustrated the situation of the prediction in each state. In 70 dB, the testing rate was 99.4%, including 3% of the data in defect 4 misled into defect 3. The error was fewer at 60 dB which the total accuracy was only 75.4%, in which the mainly error was the distinction of defect 3 and 4. The misjudgments in these two categories were higher than 50% which means the

characteristic of the defects were hard to extract. As shown in Figure 48, defect 3 and 4 (undercut and lake of penetration) are the lack of material at outer or inner surface which makes the reflections similar after the wave traveled through the defects. Therefore, under high noise level, more misleading happened.

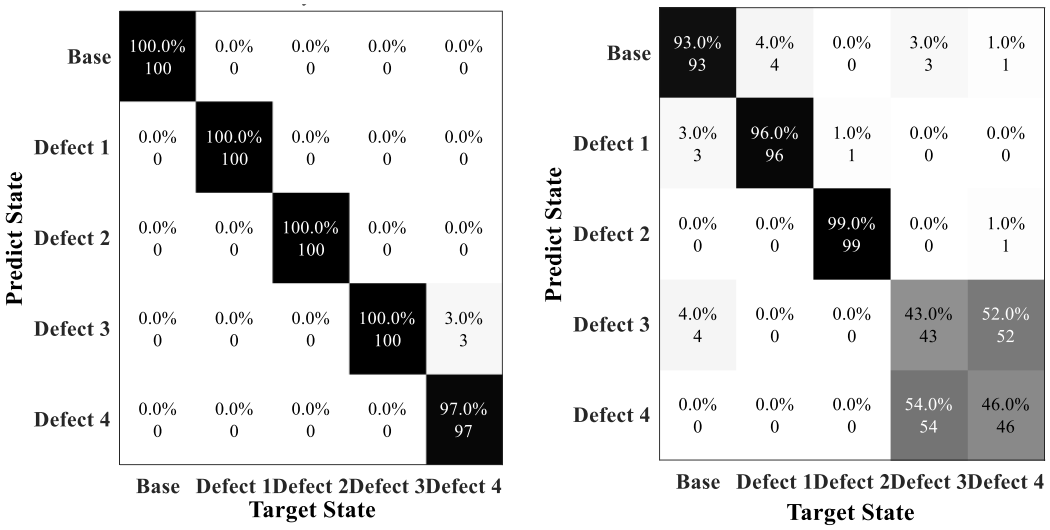

Figure 48. Testing results: (a) SNR = 70 dB (99.4%); (b) SNR = 60 dB (75.4%).

4.4.3. Classification Performance for Case 4: Detection of Damage Severities

4.4.3.1. Training and validation results of damage severities

Detecting the severity of damage is also a significant and difficult issue in ultrasonic guided wave-based health monitoring. The severity of welding defects determines the maintenance in pipeline. Therefore, the dataset consisted of three different severities of weld defect (State #10, #15, #16), and one state as the reference (State #1). Each scenario included 500 datasets generated and thus a total of 2000 data were involved in this learning. The training results of classification by CNN framework was shown in Figure 49 when SNRs were 80 db and 70 dB. In 80 dB, the error rates were arrived at zero after the 18 epochs training. In 70 dB, 120 epochs time was used training the data error reaching to zero which was more than 6 times comparing with the situation in 80 dB. In addition, the validation was equal to 0.095.

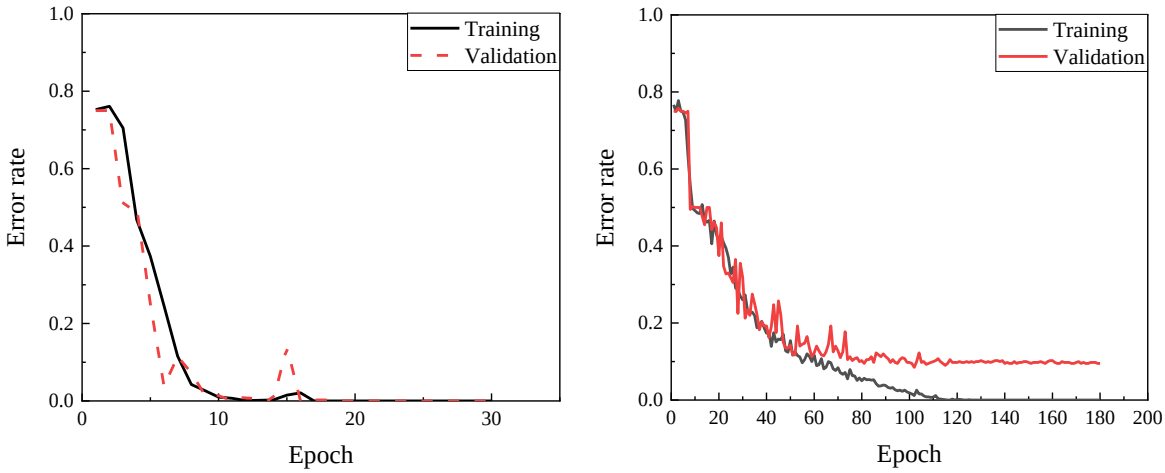

Figure 49. Training and validation results: (a) SNR = 80 dB; (b) SNR = 70 dB.

4.4.3.2. Testing results of damage severities

The damage severity results were shown in Figure 50 which represented the accuracies in 4 categories. In CNN model, the accuracies were equal to 100% and 88.75% in 80 dB and 70 dB respectively. The prediction reached to 100% when SNRs higher than 70 dB. However, in 70dB, 96% of the data labeled 10% was classified in correct, with 4% misled into label 5%. The prediction in 5% was 85% with 7 data points misclassified into 10% and 8 was in 1%. The lowest accuracy was the defect with a length of 1% in circumference where 26% data was misclassified. More errors happened when the length of the defect become smaller, and the accuracies were reduced dramatically when SNR was 60 dB.

Detailed results of the accuracy in each label were shown in Figure 51. In general, the classifier could identify the severity of the defects with high accuracy except the situations in 70 dB and 60 dB. Clearly, base condition could be much easier to be distinguished with the damage states. In 60 dB, data labeled in 1% had the lowest accuracy as only about 0.35. Meanwhile, the classification in label 5% and 10% were a little higher which closed to 0.6.

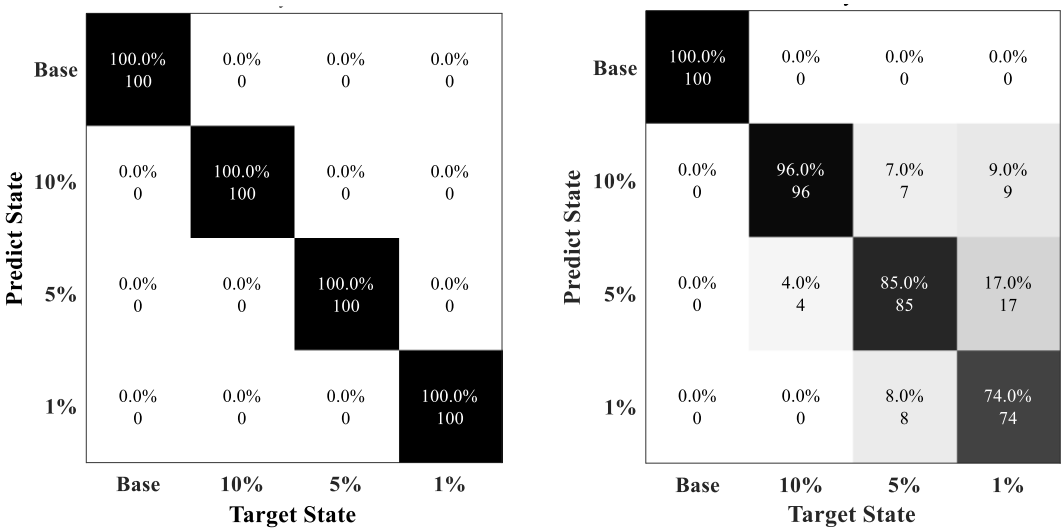

Figure 50. Testing results: (a) SNR = 80 dB (100%); (b) SNR = 60 dB (88.75%).

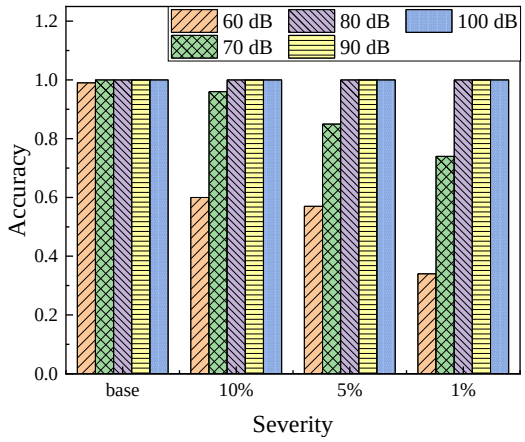

Figure 51. Locations defect in pipeline.

4.5. Summary

This section investigated a deep learning model-based damage evaluation method for pipelines using ultrasonic guided wave. Welding defects and material discontinued damages were detected by the ultrasonic guided wave and identified by 8-layer CNN models with high accuracy successfully. The dataset of ultrasonic guided wave traveled through the pipeline was generated by the simulation. The detection results were associated with classification classes in which each class represented a condition scenario of the pipeline structures, including damage types, positions,

and severities. Damage interaction was considered in this study. The effectiveness of the methods interference by noise was examined. Some conclusions can be drawn as follows:

a) The proposed deep learning networks were workable for the dataset of ultrasonic guided waves by appropriate filter sizes and parameters. Note that the networks can automatically extract the sensitivity features and effectively classify signals.

b) The position of the notch-shaped damage in the pipeline with weldment can be accurately classified by the CNN model. The interaction of damages and weldment did not affect the efficiency of the classifier. The prediction was 100% correctly in the certain noise levels, 80dB or higher. With the noise level increased to 60 dB, more misclassifications were appeared.

c) When welding defects and notch-shaped damage appeared at the same time, the CNN model could still identify the damage location correctly, especially when noise level lower than 70 dB. The interaction with two different damage did not reduce the ability of classifier.

d) Weld defect types and severities can be detected effectively by CNN model at low noise levels (higher than 70 dB). The accuracy of the result was dropped sharply when SNR was 60 dB, where the predictions were 75.4% and 62.5% respectively.

e) Mixing damage types and noise interference with different level were used to address structural uncertainty and the effectiveness of the proposed models. The result proved that the CNN models were still workable for these complex situations, except that some misjudgments appeared at high noise levels, near 60 dB.

4.6. Reference

Alobaidi, W. M. (2017). Application of Microwave and Ultrasonic Techniques for Defect Detection in Pipes, University of Arkansas at Little Rock.

LeCun, Y., L. Bottou, Y. Bengio and P. Haffner (1998). "Gradient-based learning applied to document recognition." *Proceedings of the IEEE* 86(11): 2278-2324.

Moser, F., L. J. Jacobs, and J. Qu (1999). "Modeling elastic wave propagation in waveguides with the finite element method." *NDT & E International* 32(4): 225-234.

Umakanth, S. (2018). Deep Learning Convolutional Neural Network Applications in Image Analysis to Identify Defects. *University of Illinois at Chicago*, Chicago, IL, USA,

Xu, Y., M. Luo, Q. Liu, G. Du and G. Song (2019). "PZT transducer array enabled pipeline defect locating based on time-reversal method and matching pursuit de-noising." *Smart Materials Structures* 28(7): 075019.

5. DEEP LEARNING BASED CORROSION DETECTION OF METALLIC STRUCTURES

5.1. Introduction

Corrosion is a major safety and economic issues for metal structures which causes the failure of structures and even catastrophic consequences. Lots of effort spent on inspection, repair, and rehabilitation. Comparing to traditional non-destructive testing techniques, ultrasonic guide waves could provide a fast, efficient, and accurate solution to monitor and assess the health state of corrosion metal structures.

5.2. Corrosion Measurement for Metal Structure

5.2.1. Mass Loss

The value of corrosion rate can be calculated by mass loss measurement (Cetin and Aksu 2009). The coupons were taken out, cleaned and weighted. Each of the values is measured three times and take the average value. The corrosion rate is expressed as follow (Sail and Benbrahim 2019):

$$Cr = \frac{M_1 - M_2}{S * t} \tag{53}$$

where M_1 corresponds to the initial weight of the sample, M_2 is the current weight of the sample after corrosion happened. S represents the corrosion area, and t represents the corrosion hours. When gather the weight of the sample, it should be performed under the condition with a nearly constant temperature of 25°C and low humidity (Cheng, Tao et al. 2016). The weight of the corroded sample is measured after removing the corrosion product.

5.2.2. Electrochemical Impedance Spectroscopy

The corrosion rate of normal steel samples can be present by mass loss measurement, however, the steel samples with coating protecting is difficult to measure the value of mass loss.

Electrochemical impedance spectroscopy (EIS) (Net, Ravenscroft et al.) (Jenot, Ouaftouh et al. 2001) and open circuit potential (OCP) techniques have been used widely to estimate the corrosion situation of steel under the coating. EIS is to apply a small amplitude AC signal with different frequencies to the electrochemical system, and measure the ratio of system impedance, that is the ratio of voltage to current. Therefore, relevant information associated with the electrochemical behavior can be gathered though the analysis of the EIS spectra. The impedance parameters, such as coating capacitance, resistance coating and charge transfer resistance of coatings, can be extracted by analyzing the equivalent electric circuits (Shehadeh, Steel et al. 2006, Kim and Lee 2009, Ahadi and Bakhtiar 2010, Li, Song et al. 2017).

Gamry equipment was used for EIS test to assess the corrosion of the steel with coating. 1.0% NaCL solution was filled into an 30mm-diameter glass tube with a silicon joint. The tube was clamped on the test steel plate. The measurements were proceeded in a room temperature. Then the EIS curve was carried out which was the relationship between logarithm of the impedance modulus |Z| and different frequency. The curve was also converted into phase angle with different frequency (Shehadeh, Steel et al. 2006, Ahn, Kim et al. 2018).

The equivalent electric circuits models (Ahn, Kim et al. 2018, Nair, Cai et al. 2019) in different immersion time were shown in Figure 52. In the models, Rs was the solution resistance, R_c is coating resistance, C_c is the coating capacitance, and Z_w represented the electrochemical corrosion process at the metal interface. At the first period of immersion, the coating was integrity, which acted as a barrier layer. The model was shown in Figure 52(a). The NaCL had a solution resistance R_s, and the coating can be equivalent to the coating resistance R_c and the capacitance Cc with a parallel relationship. The model was satisfied when the sample just immersed in the NaCl solution for a few hours. With the time increased, the size of capacitive loop declines that

demonstrated the water gradually penetrated into the coating layer. The protective properties of the coating were decreased at this period. However, the medium could not reach to the interface of coating and steel panel. The model for this temporary character was shown in Figure 52 (b). For a long-time immersion, the equivalent electric circuits changed due to the medium was easy to penetrate and arrive at metal substrate layer. The corrosion reaction process is mainly manifested as charge transfer. The model in Figure 52 (c) was a series with a solution resistance R_s, a coating resistance R_c in parallel with a pure capacitance C_c and a Warburg impedance element. Then, Figure 52 (d) is described the severe corrosion damage happened in coating, resulting the electrochemical reaction site generated at the interface of metal and electrolyte.

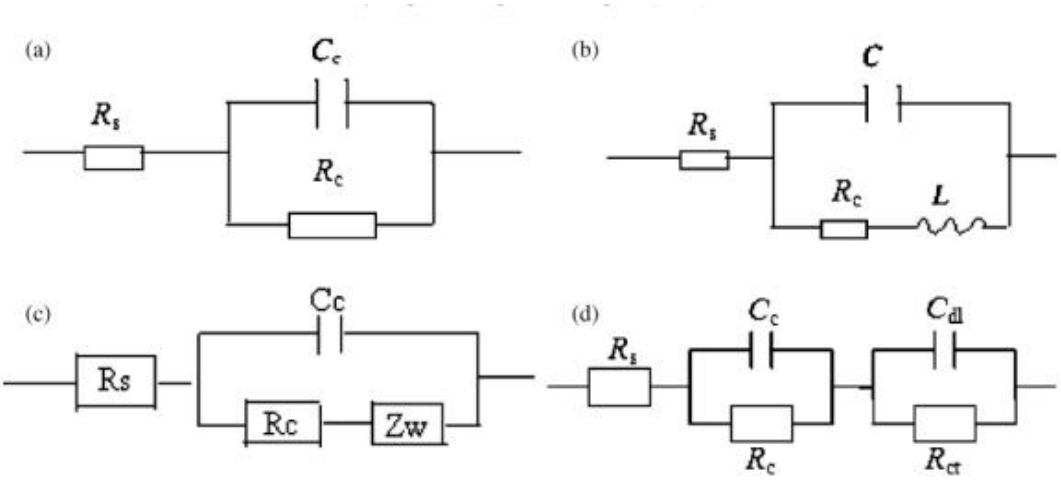

Figure 52. Equivalent electric circuit models (Nair, Cai et al. 2019).

5.3. Experiment of Pipeline Corrosion Process

5.3.1. Uncoated Pipes

In most cases, pipelines are much easier to be corroded during it service time, especially for uncoated pipes. Corrosion is a difficult issue for pipeline damage detection. In this study, ultrasonic guided wave-based corrosion damage detection is applied to estimate the corrosion stage of pipes. Four pipes with different states were designed, as shown in Table 12, considering the

welding and corrosion types (uniformed corrosion and pitting corrosion). Pipes were placed in a salt fog chamber for a period to accelerate the corrosion process. Since the size of the chamber is limited, pipes should not be too large. Thus, the diameter of pipes is equal to 76.2 mm (3 inches), the thickness is 3.175 mm (0.125 inch), and the length is 863.6 mm (34 inches). The material of the pipe is A36 steel without coating but has a film at the outside. To calculate the corrosion rate, mass loss is required for each test that the corrosion product on the pipe surface should be removed. However, this process might affect the subsequence of following corrosion. Thus, several steel plates are added here to corrode together with pipes. The mass loss of steel plates is instead of the value of the corresponding pipe. Piezoelectric actuators, which can transfer the electrical signals into mechanical ones, are glued on the left side of the pipe sample to excite initial waves. To avoid sensors from falling off or being damaged, the left side was wrapped by transparent tape which could stopped the water and air entering. Considering the case of uniform corrosion, the ends of pipes are sealed by tape to prevent internal corrosion. As for the pitting corrosion, the entire pipe is wrapped except for the corrosion part. The samples are shown in Figure 53.

Table 12. Test matrix for pipes.

Case	Label	Diameter	Length	Welding condition
Uniform corrosion	State #1	76.2 mm	863.6 mm	\
	State #2	76.2 mm	863.6 mm	Weld
Pitting corrosion	State #3	76.2 mm	863.6 mm	\
	State #4	76.2 mm	863.6 mm	Weld

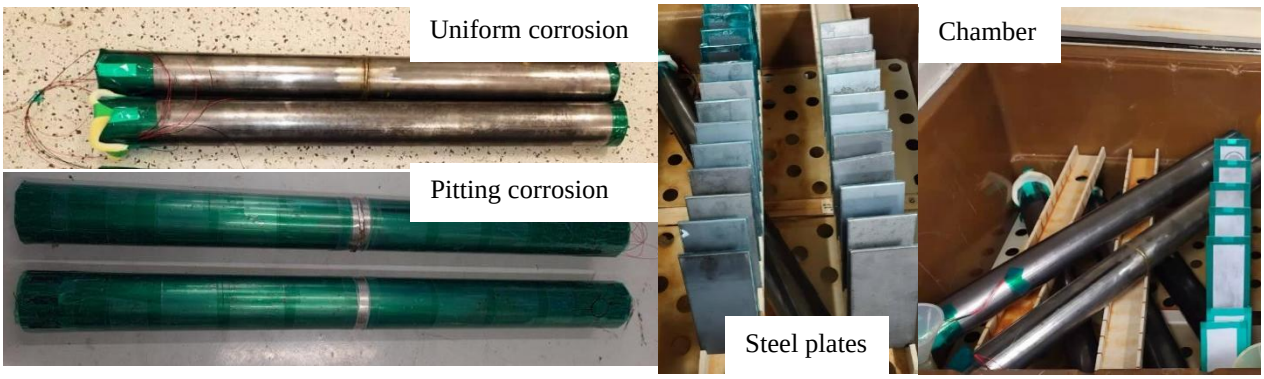

Figure 53. Experiment set up.

5.3.2. Coated Pipes

Coating is widespread used for protecting the pipeline system to avoid the corrosion. It is critical to study the experiment of the coated pipeline corroded in harsh environment. In this study, two different coating, epoxy resin and the graphene loaded epoxy resins were used to protect pipes. The parameters of pipes are same with the sample in section 7.3.1. Four states were designed including welding condition and coating types, as shown in Table 13. Steel plates were also involved in this experiment to assess the corrosion rate. All pipes and plates were put into the chamber. Due to the same material and the same environment, the EIS results of steel plates are instead the results of pipes. The reason is the EIS test is hard to operate on a curved surface. The samples were shown in Figure 54.

Table 13. Test matrix for pipes.

Case	Label	Diameter	Welding condition	coating
Variance due to coating and welding	State #1	3 inches	\	Epoxy resin
	State #2	3 inches	Weld	Epoxy resin
	State #3	3 inches	\	Epoxy resin with graphene
	State #4	3 inches	Weld	Epoxy resin with graphene

Figure 54. Experiment samples.

5.4. Numerical Simulation

This section attempted to calibrate the model set by finite element and indicate characteristics of guided wave propagating along a structure with corrosion defects. The prototype was a 34 inches long steel pipe as described in section 5.3.1. Simulating the uniform corrosion is a tough problem. Some researchers construct numerous round holes to instead the corrosion damage. The depth of the hole represented the severity of the corrosion (Jin, Chang et al. 2016, Yang, Lee et al. 2016). Thus, in this model, plenty of circular pits were constructed on the out surface of the pipe from 5 inches to 30 inches. Due to left and right boundaries were wrapped by tapes to protect the sensors for ultrasonic guided waves test. Totally, 6 different states were discussed in this part, as listed in Table 14. The material density is 7850 kg/m^3, Youngs' modulus is 210 GPa, and Poisson's ratio is 0.28. Free triangular elements available in COMSOL were used

to mesh the pipe. To ensure the calculation accuracy and consider the computational efficiency, the maximum element size is 5 mm, and the minimum element size is 2 mm. In addition, the simulation time step is set to be 0.5 μs. The excitation is a 100 kHz 5-cycle sinusoidal signal operated by Hanning window. The models established in COMSOL are shown in Figure 55. Figure 55 (a) represents the normal pipe without any damage or material discontinuity. Figure 55 (b) is the steel pipe with a butt weldment located at middle. Figure 55 (c) shows the steel pipe with initial uniform corrosion at the outside surface. To simulate the serious corrosion damage, pits on the pipeline surface were set much bigger, deeper and more than the slight one. The model is shown in Figure 55 (d). Figure 55 (e) and (f) are pipes with girth weld.

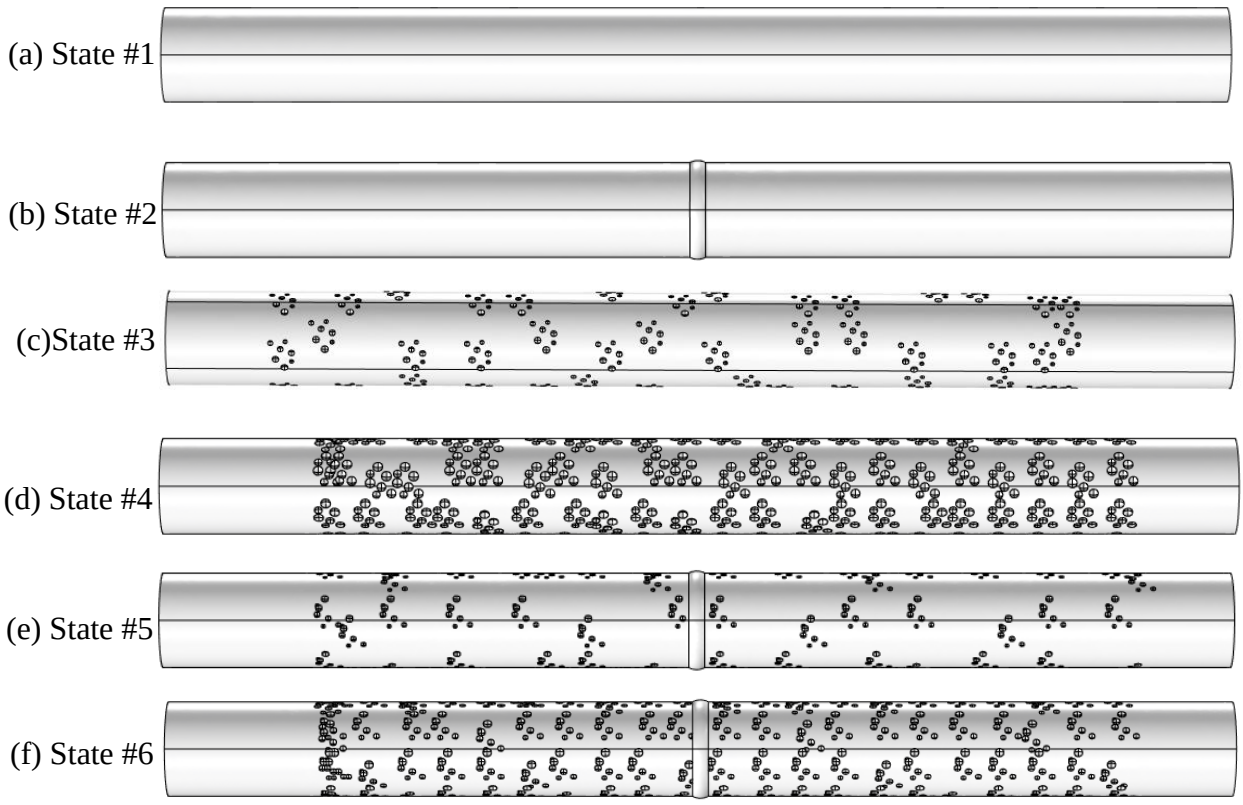

Figure 55. Model of pipes with and without weldment in different aging states.

Table 14. Test matrix for pipe models.

Case	Label	Diameter	Weldment	Damage
Reference	State #1	3 inches	\	\
	State #2	3 inches	With girth weld	\
Variance due to aging effects	State #3	3 inches	\	Uniform Corrosion (slight)
	State #4	3 inches	\	Uniform Corrosion (serous)
	State #5	3 inches	With girth weld	Uniform Corrosion (slight)
	State #6	3 inches	With girth weld	Uniform Corrosion (serous)

Calibrated the simulation model, the result was shown in Figure 56. The signals from experiment and the simulation were normalized to ensure the amplitude of the data was close. The prototype was an undamaged pipeline excited by guided waves with 100 kHz. The black line was the wave collected from experiment, and the red dash line represented the simulation result. Clearly, two signals had similar excitation. Due to the experiment used several sensors worked together to excite the pipe, thus the front part overlapped by several signals. In simulation, 32 points were work together so that the initial signal was much clearer. With the signal propagated through the pipe, some reflections appeared in experiment signal. The middle part of the simulation signal was not pretty flat. The last part was boundary reflection. The location was close, but the boundary reflection was a little different due to the manufacturing errors or material errors happened in experiment pipe. Overall, the simulated model built in finite element software could represented the experiment result for further study.

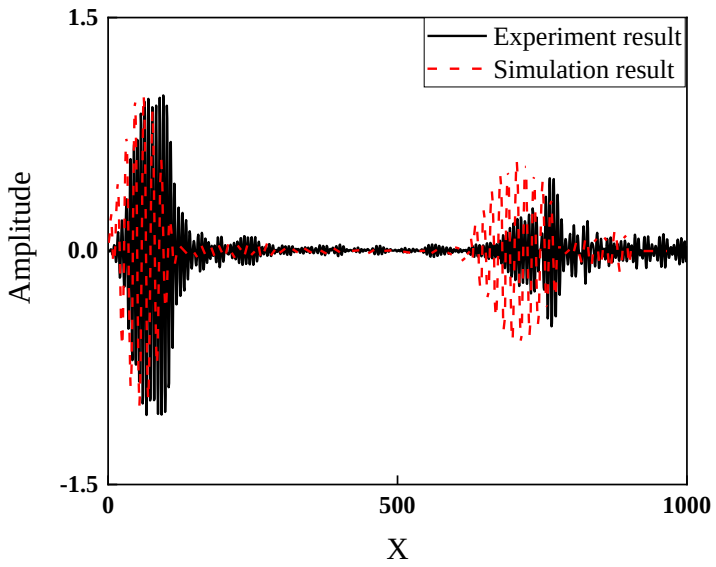

Figure 56. Calibration of numerical simulation.

The entire procedure of guided waves propagation in the pipeline is clearly shown in Figure 57. Without damage, the waves had less reflection. The energy of the excitation had less attenuated during propagating. The waves spent about 4E-4 s to be received by the sensors.

The process of guided waves propagating through the pipe in State #3 were shown in Figure 58. The excitation was sent into the pipe from the left side. The wave propagated from the left side to the right. In 5E-5 s, Waves met the damage and echo was appeared. As waves traveled forward, more corrosion pits made the reflection and the scattering increase. At 2E-4 s, the waves arrived the right boundary and returned to the left side. The main waves with the dark color were still propagating, meanwhile, the derived waves were distributed to the whole pipe. At around 4E-4, the main waves were finished one round trip in the pipeline. Compared with the ordinary steel pipe, the pipe undergoing corrosion produced more reflected waves during the propagation, while the energy of the main waves was significantly reduced.

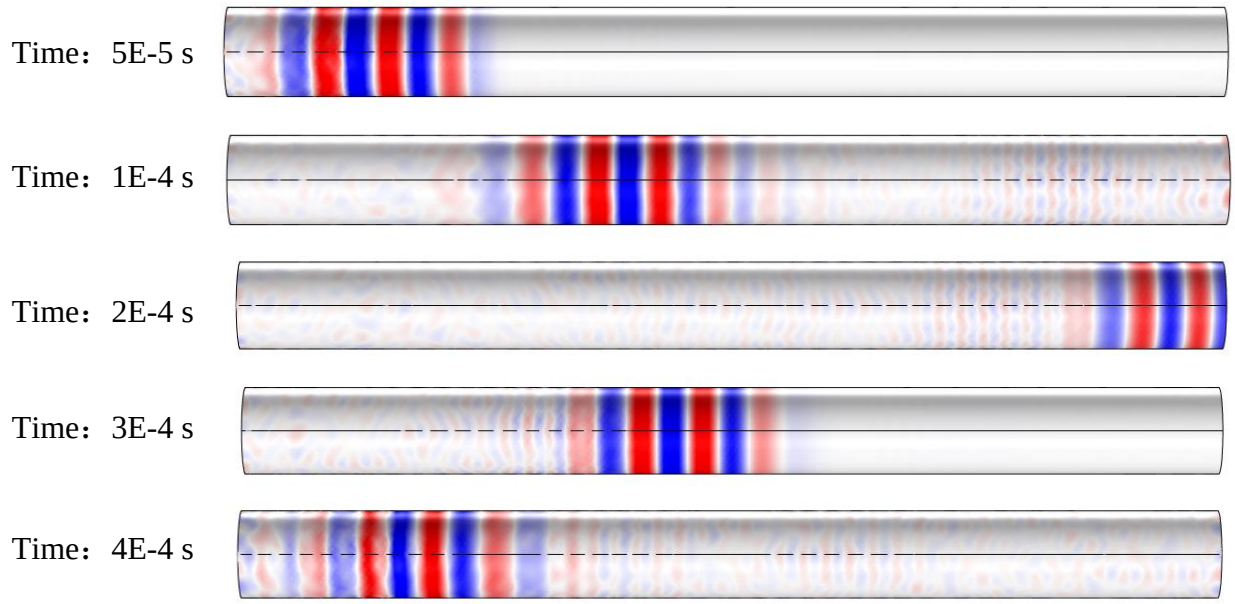

Figure 57. Guided waves propagated through the pipe.

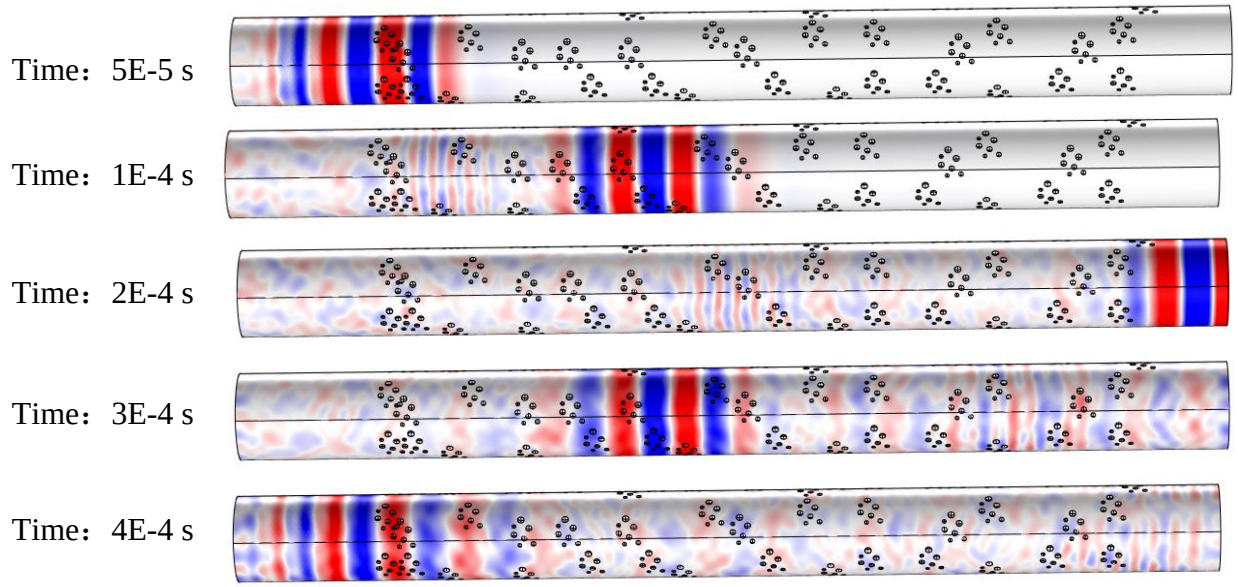

Figure 58. Guided waves propagated through the corroded pipe.

Figure 59 represents the signals collected from different pipe states. Clearly, in State #1 shown in Figure 59 (a), only two main packets into reflection, including an initial input signal and an echo one from right boundary. For State #2, the welding echo was clearly shown at around 0.0002 s. Figure 59 (c) represented the received signal from corrosion pipe. Slight corrosion

distributed the entire pipeline, which appeared as some pits on the surface. When guided waves met these pits, some of them was scattering and reflecting. Part of the excitation energy were taken away by the refection, the other waves kept moving forward. Subsequently, some low-amplitude oscillations appeared between the initial wave and the boundary echo, which is from the corrosion damage. Figure 59 (d) illustrated the result of a pipe with serious corrosion. Specifically, the reflections from corrosion damage were larger than waves in State #3. With the corrosion becoming seriously, the amplitudes of the echoes were increased. Figure 59 (e) was the corroded pipe with butt weld at middle. From the receive signal, the reflected wave from weld was clearly represented at around 2E-4 s and the corrosion reflection was also existed. Figure 59 (f) showed the signal in State #6. Compared with the State #5, the corrosion was more serious, the amplitude of the right boundary reflection were smaller, and more derivative waves from the corrosion pits. The reflection of the weldment was still at the around 0.0002 s, but a little hard to separate it with the corrosion damage.

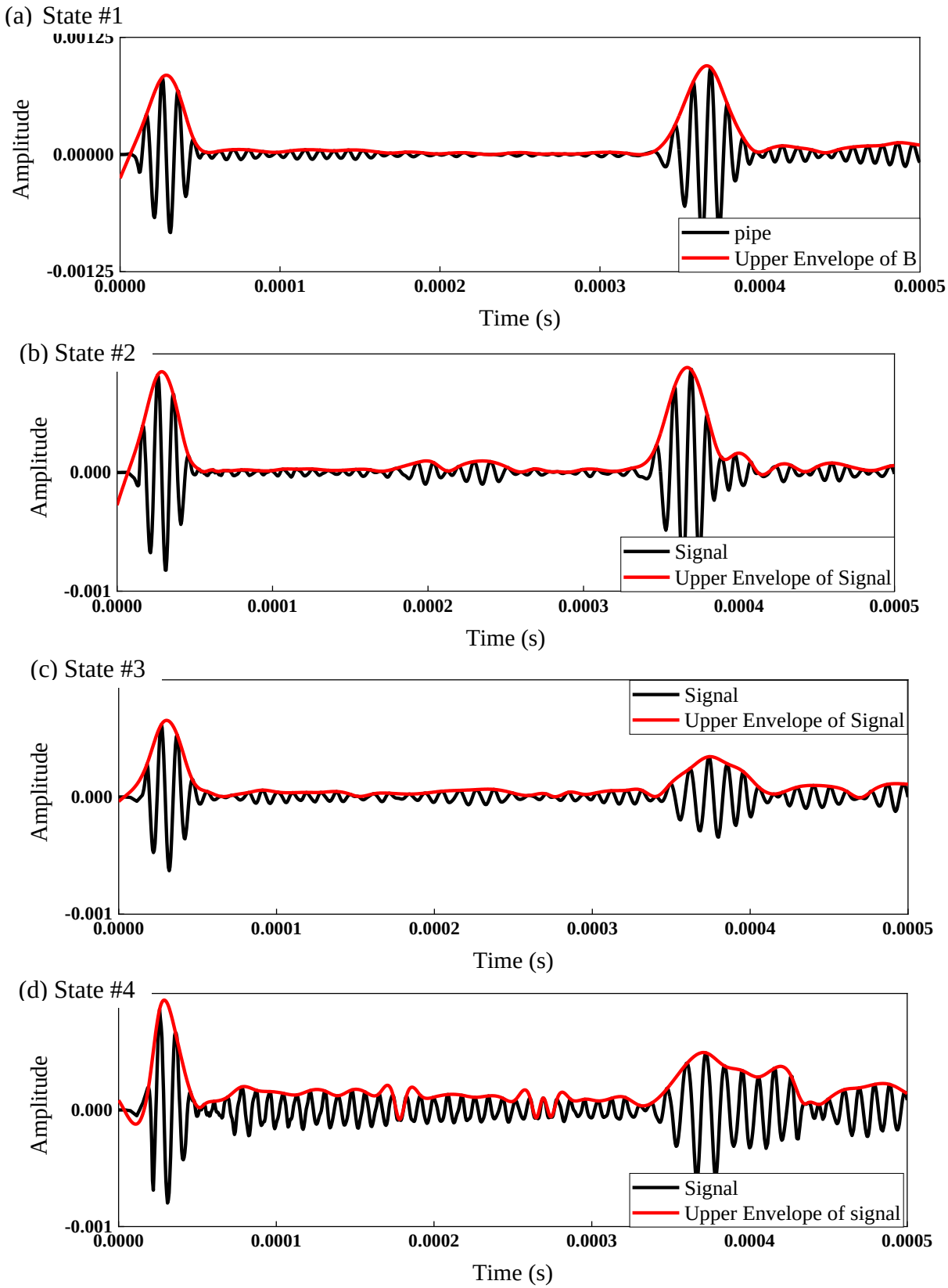

Figure 59. Signals from different states (a)-(f).

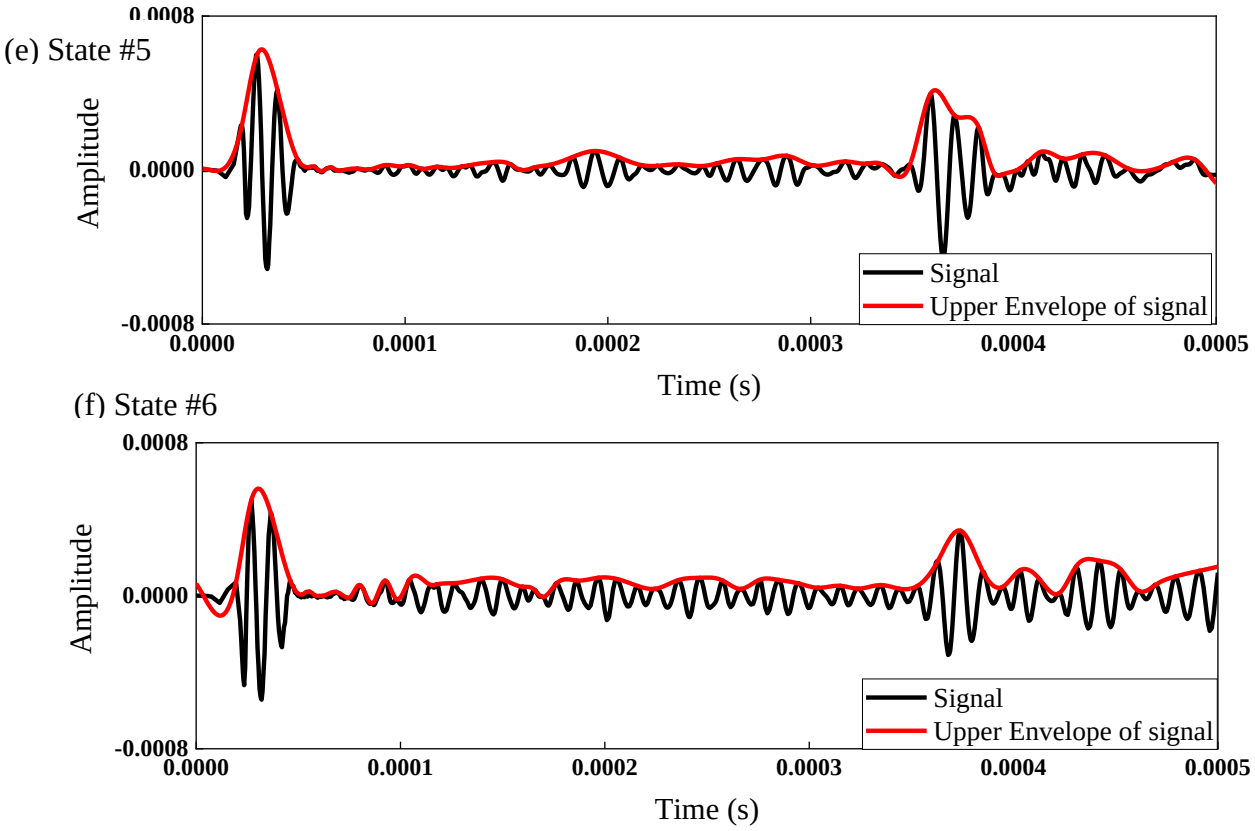

Figure 59. Signals from different states (a)-(f) (continued).

5.5. Results and Discussion

5.5.1. Results of Uncoated Pipe

The received signals are more susceptible to be contaminated by environment noise and equipment noise during the inspection. Thus, the data from simulation was enlarged by adding Gaussian white noise to consider the noise from testing. The 6 states of the uncoated pipe simulated with finite element software were divided into 3 groups, undamaged state (State #1, 2), slight corrosion (State #3, 5), and serious corrosion (State #4, 6). 1500 data samples were generated randomly as the input dataset. The noise levels were set from 60 dB to 100 dB. The increase of the noise weakened the characteristics of the signal and increase the complexity of the signal, which made the signal identification and feature extraction more difficult. The whole data were separated

into 3 groups, training dataset, validation dataset and test dataset, accounting for 60%, 20% and 20% respectively.

The training and validation results are shown in Figure 60. 6 error curves represent the training and validation performance under different noise levels. All the curves start around 0.7 and fall close to 0 during a period studying. The bule solid line and dash line show the training and validation results in 100 dB. Under this situation, the model has high performance which the error rates were equal to zero after experienced three epochs. With the noise level increased, the model needed more time and iterations to training the data, where spent nearly 5 epochs to perfect the model. However, at 60 dB, the training curve converged to 0 at the 13th epoch. In addition, some errors were appeared during validation, resulting the error equal to 0.07 after 13 epochs. Obviously, the noise was affecting the accuracy of the CNN model to some extent.

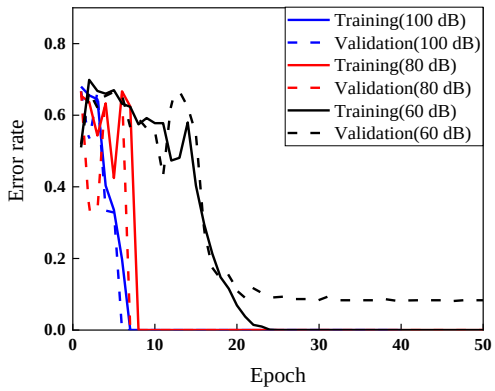

Figure 60. Training and validation results.

The test results were shown in Figure 61. A total number of 300 signals are input into the pretrained CNN model, and the prediction of each data is obtained. In most case, the CNN model can accurately predict the result. Specifically, the accuracies are equal to 100% when noise levels are from 100 dB and 70 dB as shown in Figure 61(a). When noise level increases to 60 dB, the total accurate was 93%, which means 21 data points are misled into wrong categories. The confusion matrix in Figure 61(b) illustrated the specific results. Obviously, 95% of the data in

State #1 and 2 (Undamaged group) is predict correctly, except 2 signals are misclassified into slight corrosion state, and 3 data are misclassified in serious corrosion state. 7% of the data in slight corrosion are failed identification, with 5 points misclassified into undamaged state and 2 in serious corrosion state. The accuracy of serious group is 91%, including 8 points mislead into slight corrosion and one points into undamaged state. The results showed that CNN could identify the signals accurately and efficiently.

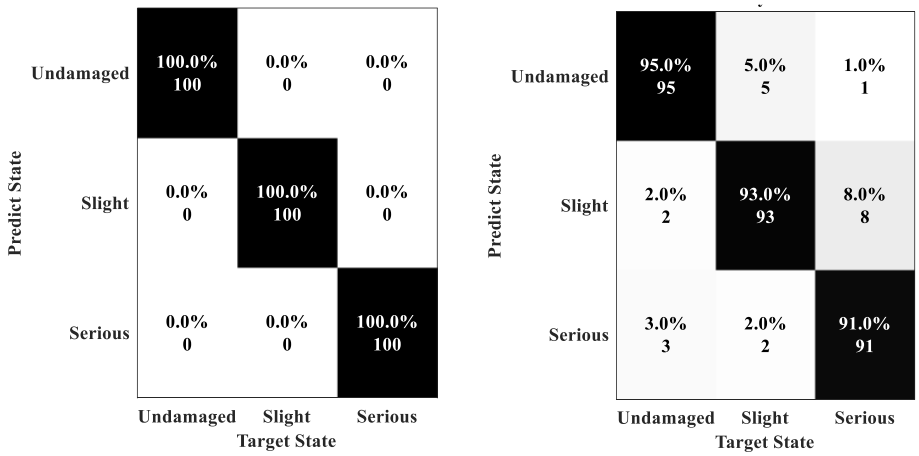

Figure 61. Testing results: (a) SNR = 100 dB, accuracy = 100%; (b) SNR = 60 dB, accuracy = 93%.

Then, the experiment results collected by the receivers are put into the CNN model trained under the noise level equal to 100 dB. The results, as shown in Table 15, demonstrate that the initial signals are marked as the undamaged state, the signals collected after the pipe experienced in the chamber for 24 hours and 48 hours are marked as slight corrosion state, and the data collected after 144 hours, 432 hours and 864 hours are marked as serious corrosion state.

Table 15. Experience results.

Hours	0	24	48	144	432	864
state	Undamaged	Slight	Slight	Serious	Serious	Serious

5.5.2. Results of Coated Pipe

All these received signals are identified by CNN classifier. The data divide into 2 groups, undamaged state and corrosion state, since the pipe is slightly corroded under the protection of coating. 1000 data points are generated in different states by adding noise. The performance of the classifier is illustrated in error curves in Figure 62. At 100 dB, 10 epochs are used to train the model and decrease the error rate into 0. With noise level increased, the model needed more data to learning the features, which spent 13 epochs to improve the prediction accuracy into 100%. The situation becomes worse at 60 dB, where the CNN is trained well at 32nd epoch, but the validation rate could not converge to 0 (at around 0.05). It is because the increased noise covered some important features. Thus, noise is a critical issue to affect the accuracy of CNN classification. Figure 63 shows the confusion matrixes of test results when SNRs were 100 dB and 60 dB. From the results, the classifier gets good results when noise levels higher than 70 dB. All the test data can be predicted into right categories. At 60 dB, the accuracy of the trained CNN is 93.5%. The confusion matrix showed the specific result of each data. Clearly, 10 data points in undamaged state were misled into corrosion state, and 1 data in corrosion state was predicted failure.

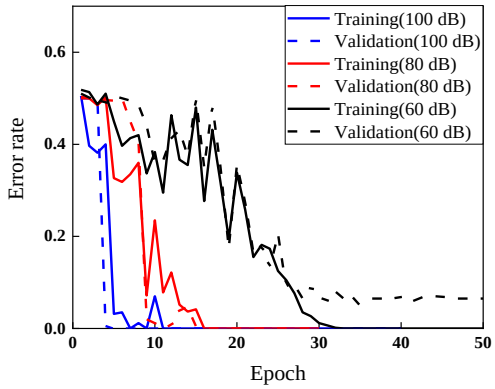

Figure 62. Training and validation results.

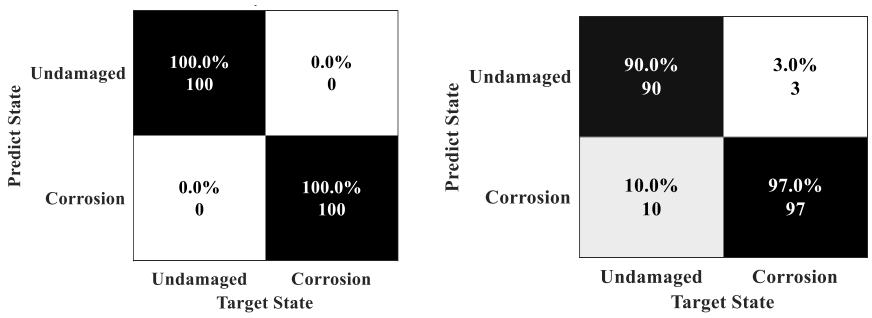

Figure 63. Testing results: (a) SNR = 100 dB, accuracy = 100%; (b) SNR = 60 dB, accuracy = 93.5%.

The EIS test, as shown in Figure 64, is used to measure the corrosion rate of the pipe. 1% NaCL was pour into the glass tube and remained open to the air. Then, the EIS curve can be obtained under the ambient temperature(20^{o}C). The steel plate in EIS test was put into the chamber with the pipes, thus, the corrosion rate of the plate is same with the pipe. The pipes and the plates experienced the salt fog to accelerate the corrosion in the chamber. The ultrasonic guided wave and EIS test were executed each period. The results were shown in Figure 66. The damage indexes are shown in Figure 67. Clearly after 48 hours experienced in chamber, the corrosion is serious.

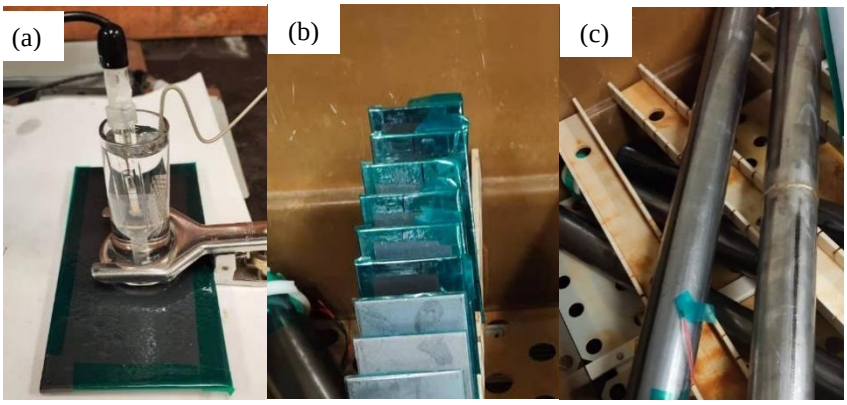

Figure 64. EIS test and the materials in chamber.

Figure 65. Experiment results.

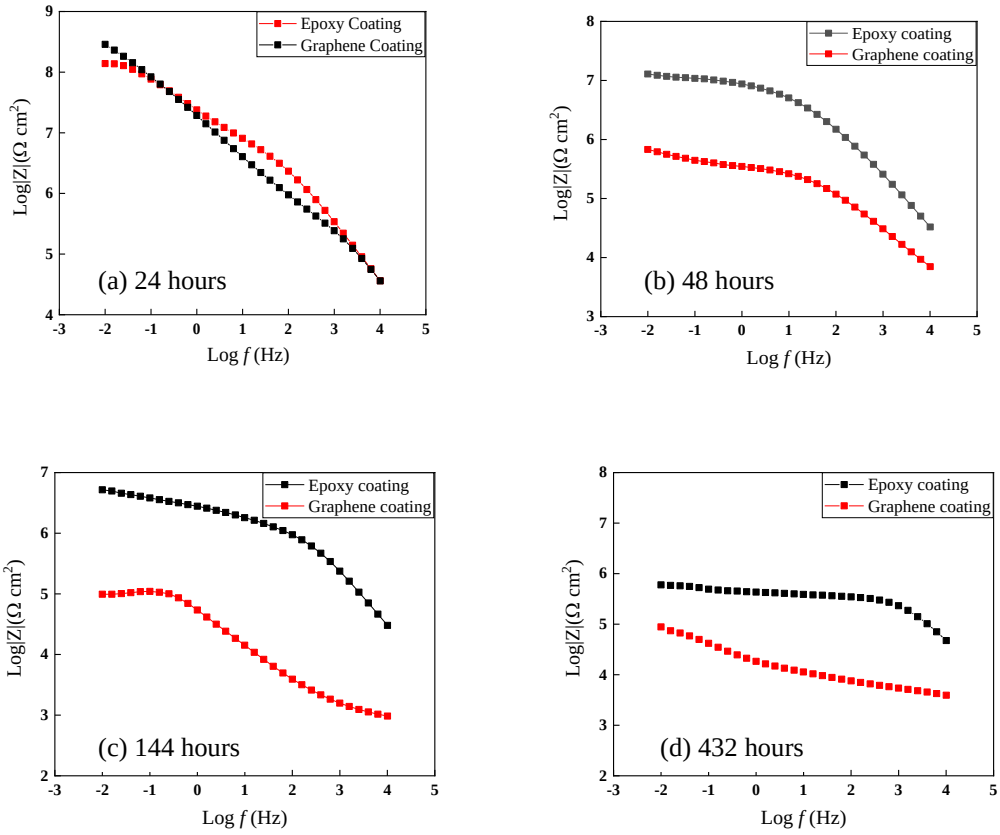

Figure 66. EIS results.

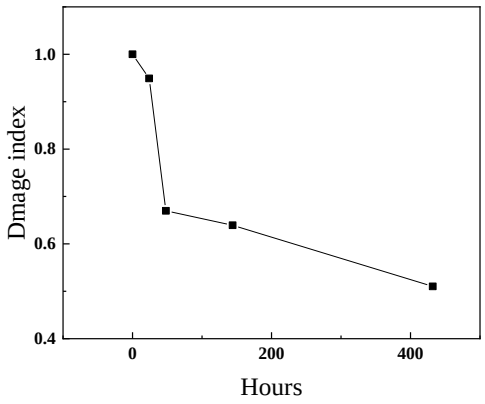

Figure 67. Damage index.

Using the ultrasonic guided wave to test the pipes, the received signals was classified by pretrained CNN model. The results are shown in Table 16. In detail, the initial signals and signals collected after the pipe experienced in the chamber for 24 hours are marked as the undamaged state, and the data collected after 48 hours, 144 hours, and 432 hours are marked as corrosion state.

Table 16. Experience results.

Hours	0	24	48	144	432
state	Undamaged	Undamaged	Corrosion	Corrosion	Corrosion

5.6. Summary

This study investigated the deep learning based guided wave process for corrosion prediction of uncoated and coated pipes. The CNN model was established for automatically encoding the hidden information from complex signals that accounted for the impacts of different noise levels and embedded grout materials. Some conclusions can be listed as follows:

a) Deep learning method effectively encoded the guided waves under complex uncertainties and identify structures in different corrosion level.

b) The deep learning approach also exhibited high accuracy and robustness for data with high noise interference. The CNN classification for most cases could reach up to 100%, when the

noise levels were lower (70 dB – 100 dB). However, when the noise increased to a much higher level (60 dB), all the signals were totally contaminated, which was the reason why the effectiveness of the classification dropped.

5.7. Reference

Ahadi, M. and M. S. Bakhtiar (2010). "Leak detection in water-filled plastic pipes through the application of tuned wavelet transforms to Acoustic Emission signals." *Applied Acoustics* 71(7): 634-639.

Ahn, B., J. Kim and B. Choi (2018). "Artificial Intelligence-based Machine Learning considering Flow and Temperature of the Pipeline for Leak Early Detection using Acoustic Emission." *Engineering Fracture Mechanics*: S0013794417312742.

Cetin, D. and M. L. Aksu (2009). "Corrosion behavior of low-alloy steel in the presence of Desulfotomaculum sp." *Corrosion Science* 51(8): 1584-1588.

Cheng, Q., B. Tao, L. Song, W. Zhang, X. Liu, W. Li, B. Hou and Q. Liu (2016). "Corrosion behaviour of Q235B carbon steel in sediment water from crude oil." *Corrosion Science* 111(oct.): 61-71.

Jenot, F., M. Ouaftouh, M. Duquennoy and M. Ourak (2001). "Corrosion Thickness Gauging in Plates Using Lamb Wave Group Velocity Measurements." *Meas. Sci. Technol* 12(8): 1287–1293.

Jin, H. Z., D. L. Chang and Y. Yang (2016). The Effect of General Corrosion on the Guided Wave Inspection of the Pipeline. *MATEC Web of Conferences*. **63:** 01036.

Kim, M. S. and S. K. Lee (2009). "Detection of leak acoustic signal in buried gas pipe based on the time–frequency analysis." *Journal of Loss Prevention in the Process Industries* 22(6): 990-994.

Li, S., Y. Song and G. Zhou (2017). "Leak detection of water distribution pipeline subject to failure of socket joint based on acoustic emission and pattern recognition." *Measurement*: S0263224117306498.

Nair, A., C. Cai and X. Kong (2019). "Acoustic emission pattern recognition in CFRP retrofitted RC beams for failure mode identification." *Composites Part B: Engineering* 161: 691-701.

Net, N., F. Ravenscroft, R. Hill, C. Duffill and D. Buttle (1998). "CHIME- A New Ultrasonic Method for Rapid Screening of Pipe, Plate and Inaccessible Geometries." *Plate and Inaccessible Geometries*.

Sail, L. and A. Benbrahim (2019). "Comparative behavior study of steel corrosion inhibition kinetics by three phosphate inhibitors with mass loss measurements." *Journal of Adhesion ence and Technology* 34(1): 48-66.

Shehadeh, M., J. A. Steel and R. L. Reuben (2006). "Acoustic Emission Source Location for Steel Pipe and Pipeline Applications: The Role of Arrival Time Estimation." *ARCHIVE Proceedings of the Institution of Mechanical Engineers Part E Journal of Process Mechanical Engineering* 220(2): 121-133.

Yang, S. K., P. H. Lee and J. W. Cheng (2016). "Evaluation of general corrosion on pipes using the guided wave technique." *Journal of the Chinese Institute of Engineers* 39(4): 1-11.

6. CNN BASED STRESS LEVEL PREDICTION OF STRUCTURES BY ULTRASONIC GUIDED WAVE

6.1. Introduction

By introducing pre-compression/inverse moment through prestressing tendons or rods, prestressed concrete (PC) structures could overcome conventional concrete weakness in tension and thus they are widely accepted in a variety of large-scale, long-span structures. Unfortunately, prestressing tendons or rods embedded in concrete are vulnerable to degradation due to corrosion. These embedded members are mostly inaccessible for visual or direct destructive assessments, which in turn posts great challenges in determining prestressing level and any corrosion-induced damage. As such, the ultrasonic guided waves, as one of non-destructive examination methods, could provide a solution to monitor and assess the health state of embedded prestressing tendons or rods. Complexity of the guided wave propagation and scattering in nature as well as high variances stemmed from structural uncertainty and noise interference as PC structures may experience under complicated operational and harsh environmental conditions often make traditional physics-based methods invalid. Alternatively, the recent emerging machine learning approaches are great potentials for processing the guided wave signals with better capability of decoding structural uncertainty and noise. Therefore, this study aimed to tackle stress level prediction and the rod embedded conditions of prestressed rods in PC structures through the guided waves. The deep learning approach, convolutional neural network (CNN), was used to process the guided wave dataset. A total of fifteen scenarios were designed to address the effectiveness of the stress level prediction under different noise levels and grout materials. The results demonstrated that the deep learning approaches exhibited the high accuracy for prestressing level prediction under structural uncertainty due to the varying surrounding grout materials. Moreover, the t-

distributed stochastic neighbor embedding technology was utilized to visualize the feature maps obtained by the CNN and illustrated the correlation among different categories. The results also revealed that the proposed CNN model still exhibited the robustness with the high accuracy for processing the data with high noise interference.

6.2. Numerical Simulation

6.2.1. Calibration of the FE Analysis of the Ultrasonic Guided Waves through the Rod

To ensure proper parameters used for the rod simulation and calibrate the effectiveness of FE based simulation for capturing the characteristics of the wave propagation along prestressed rods. One case of the characterization of ultrasonic guided waves along an anchor rod was selected from the literature (Beard and Lowe 2003, M., Beard et al. 2003), in which the rod had a diameter of 21 mm and 2.3 m in length, and was embedded in a concrete block with a cross section of 1.0 m by 1.0 m and a depth of 2.0 m, as shown in FE meshed model in Figure 68(a). The excitation of the ultrasonic guided waves was a 6-cycle toneburst with frequency of 35 kHz. The comparison results were shown in Figure 68(b), where signals in the literature were marked in the red lines and the black ones were generated from this study, and three wave packets as circled denote the excitation signals, 1st right boundary reflection, and 2nd right boundary reflection, respectively. As clearly shown in Figure 68(b), the simulated guided waves matched well with the experimental data in the literature in most cases, where three wave packets were captured well. The 1st boundary wave reflections from simulated signals occurred at 0.001 s, identical to the experimental data with comparable amplitudes. Note that some deviations occurred after the excitation, and the potential reason could partially result from the attenuation of concrete block where the simulation did not capture well. However, the entire trend and amplitudes in most cases were in well agreement with

the literature, suggesting that the simulation used in this study was proper to ensure capturing the characteristics of the ultrasonic guided waves through the rods.

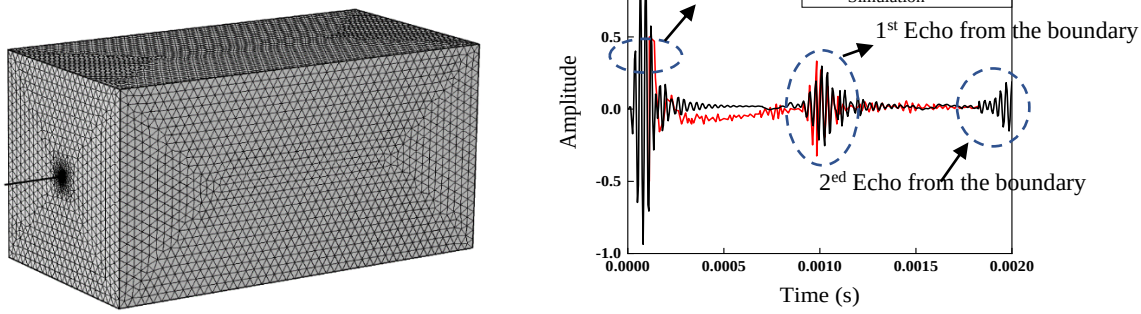

(a) Meshing of the rod embedded in concrete. (b) Comparison of signals with the literature.

Figure 68. Calibration of the FE model.

6.2.2. Design of Scenarios

The rod (Haskins 2015) was 31.75 mm in diameter with a length of 3657.6 mm. The density of the steel rod was 7800 kg/m^3, the Young's modulus was 2e^5 MPa, and the Poisson ratio was 0.3. A clamp served as the anchorage of the rod, which was located at 50.8 mm away from the free end. Besides the reference where the rod had no grout, two grout materials, the use of grease and cement, were selected to unveil their effects on the effectiveness of the proposed methods. The density of the cement was 1440 kg/m^3, the Young's modulus was 2.5E4 MPa, and the Poisson ratio was 0.25. The density of the grease was 2600 kg/m^3. The detail information of rod models was shown in Figure 69. The entire rod with the clamp was illustrated in Figure 69(a). Note that meshing figure is a schematic diagram, the actual meshing unit is much smaller), and the embedded rod was shown in Figure 69(b). Specifically, the rod passed through the plastic pipe and then added grease and cement to fill the gap between the pipe and the rod. The outer diameter of the plastic pipe was 52.07 mm, and the thickness was 2.54 mm. In finite element studies, meshing was one of critical parts in simulation. Free triangular element was selected in this model. Guided wave

simulation required high quality meshing system to minimize the propagation error of guided wave. Thus, a wavelength needs to contain at least 8 elements. In this study, the maximum element size in the model was 2 mm and time steps were 5E-6 s. Guided wave could be excited in the rod by adding displacement loads in all nodes of left boundary in the model. The excitation waves were 35 kHz 5-cycle sinusoidal waves modulated by Hanning window. 4 points, as received points, distributed the circumferential surface of the rod. Positions of received nodes were 5 mm away from the left side. Received signals were time series data, which intercept the first 1000 data points as results for further study.

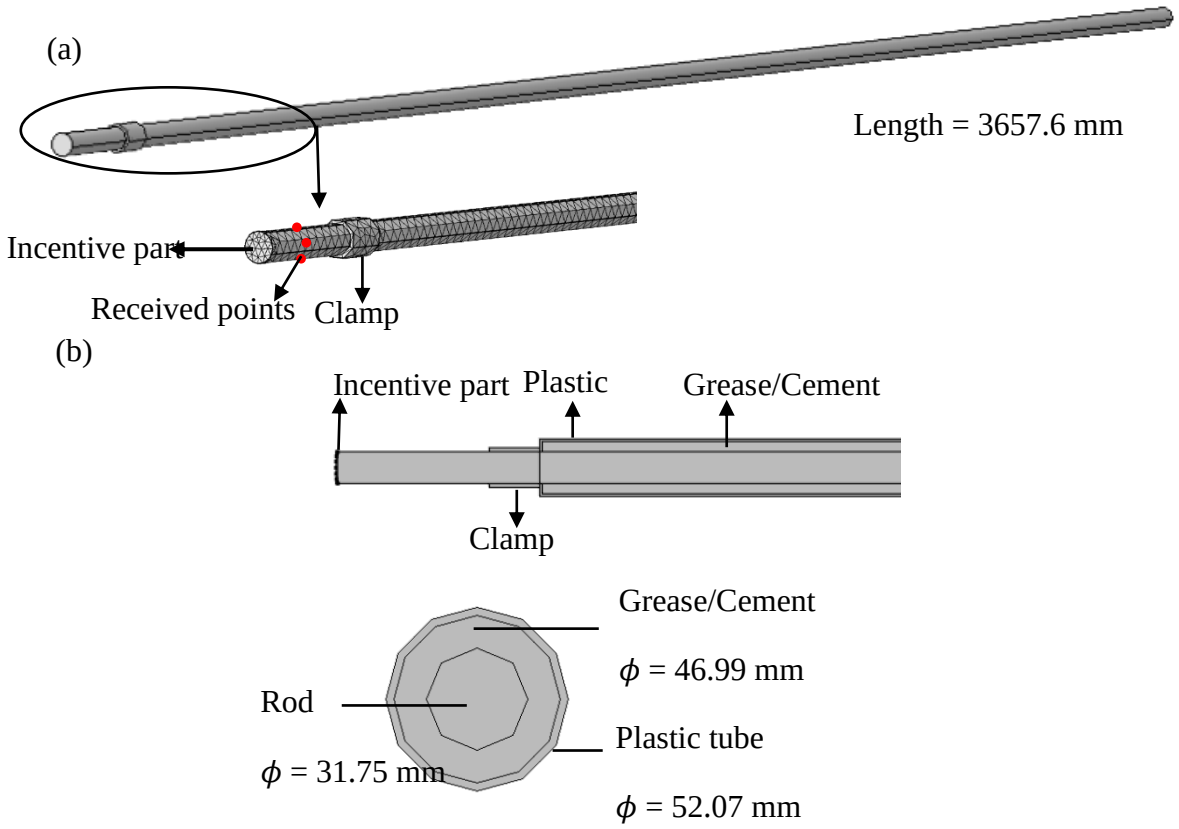

Figure 69. Rod models.

To simulate the stress reduction in prestressed components, 5 different pressure levels were loaded into each rod, including no prestress (State #1), 20% ultimate tensile strength (UTS) (State #2), 40% UTS (State #3), 60% UTS (State #4) and 80% UTS (State #5). Totally, 15 cases were designed in this section which were shown in Table *17***Error! Not a valid bookmark self-reference.**. Noise was added into the data to increase the uncertainty of the dataset.

Table 17. Test matrix for computation modeling.

Case	State	Prestressing level (UTS)	Grout material	Noise level
1 (no grout)	# 1	zero	\	100 dB – 60 dB
	# 2	20%	\	
	# 3	40%	\	
	# 4	60%	\	
	# 5	80%	\	
2 (grease)	# 6	zero	Grease	
	# 7	20%	Grease	
	# 8	40%	Grease	
	# 9	60%	Grease	
	# 10	80%	Grease	
3 (cement)	# 11	zero	Cement	
	# 12	20%	Cement	
	# 13	40%	Cement	
	# 14	60%	Cement	
	# 15	80%	Cement	

6.2.3. Data Collection and Augmentation

Figure 70 showed the time records with 5 different prestress levels derived from the finite element simulation in Case 1 from Table 1. The received point was located at 5 mm away from the left side of the rod. To ensure the input wave had similar energy, all the received signals were normalized, which the maximum amplitude of the first packet was equal to 1. The time series were

from 0 s to 0.005 s that the guided wave can propagate and reflect at least twice throughout the rod. Figure 70(a)-(e) illustrated received signals of the steel with prestress levels equal to 0% UTS, 20% UTS, 40% UTS, 60% UTS and 80% UTS respectively. Specifically, at low prestress level states (0 - 40% UTS), results clearly exhibited three main wave packets that represented the initial excitation, the first and second reflections from the boundary. Followed the first packet, fluctuations with small amplitude were echoes from the clamp. With the stress level increased, the amplitude of this part was smaller, and it was hard to detect at 80% UTS. In addition, the velocity of guided waves reduced with increasing the stress of the rod. Clearly, the first reflection from the right boundary was around 0.0018 s in Base state. The value was raised to 0.0019 s and 0.002 s when stresses were 40% UTS and 80% UTS. At 60% and 80% UTS (shown in Figure 70(d)-(e)), only two main packets were existed in the signals, where one was initial input waves, and the other was the boundary reflection. Clearly, the energy of guided waves was dissipated when waves propagated at the second cycle. Thus, it was difficult to detect the second echo from the boundary.

As clearly illustrated in Figure 71, the collected guided waves of the rod exhibited different patterns resulting from different grout materials. Figure 71 illustrated signals collected from states #1, #6, #11 (without stress) in time domain and frequency domain, respectively. It was observed from the time domain that with long distance propagation, the energy of reflection waves was reduced progressively. However, comparing with these three states, the rod embedded in cement had highest attenuation, where the peak value of reflections was reduced from 0.2588 to 0.1075. After propagating to the second cycle, the peak value of the second boundary echo was reduced to 0.0897 in unembedded state, and the value of the rod in cement was lowest, which was 0.0113. On the contrary, grease had less effect on guided waves. With 1463.04 mm of propagation, the peak value of reflected waves was 0.0455 which was close to unembedded state. In frequency domain,

it was clearly that the main frequency of waves was 35kHz. Some weak peaks occurred at the low frequency and the high frequency due to reflections from the clamp and the boundary.

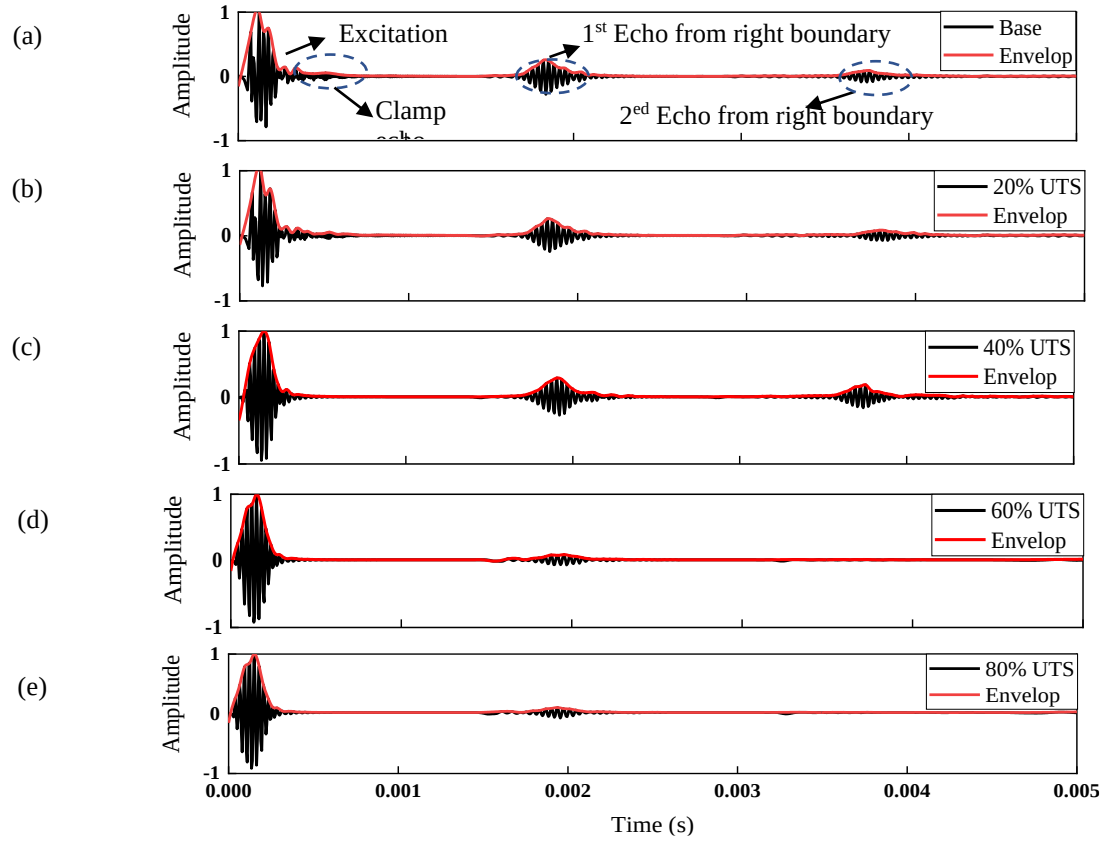

Figure 70. Received signals in different stress levels. (a) zero; (b) 20% UST; (c) 40% UTS; (d) 60% UTS; (e) 80% UTS.

A total of 15 states were designed to simulate the actual situation of the rod in the project. In each state, 4 received nodes were distributed around the circumference where were located at 5 mm to the left side. Since the received waves were much easily contaminated by noise, 5 noise levels based on signal to noise ratio (SNR) were added into the received signals. In addition, noise involved in the signals could increase the uncertainties of the data, attempted to investigate the robustness of the deep learning methods. Specifically, Figure 72 illustrated the collected signal in 5 different noise levels. Clearly, when SNR exceeded 80 dB, the interference from noise was

obvious and covered some original features of the initial signals. Especially in 60 dB, the amplitude of the noise was greater than the signal amplitude, which was not conductive for further study.

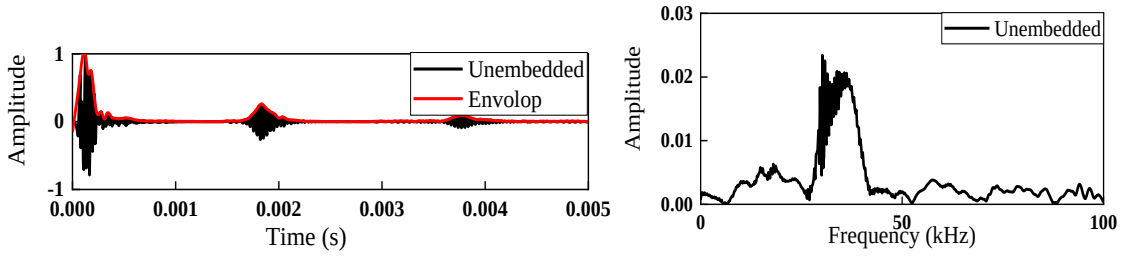

(a)

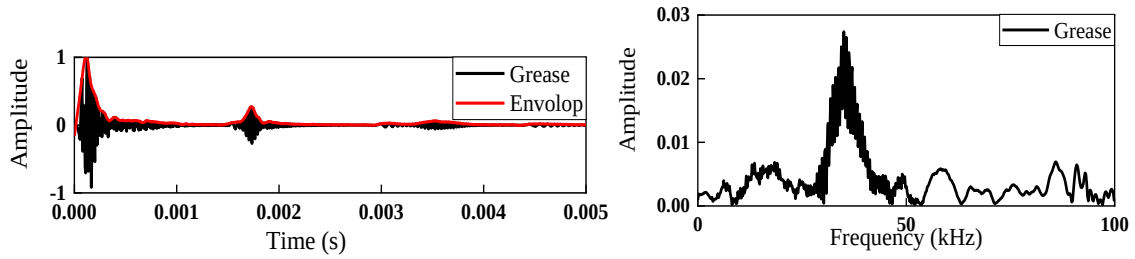

(b)

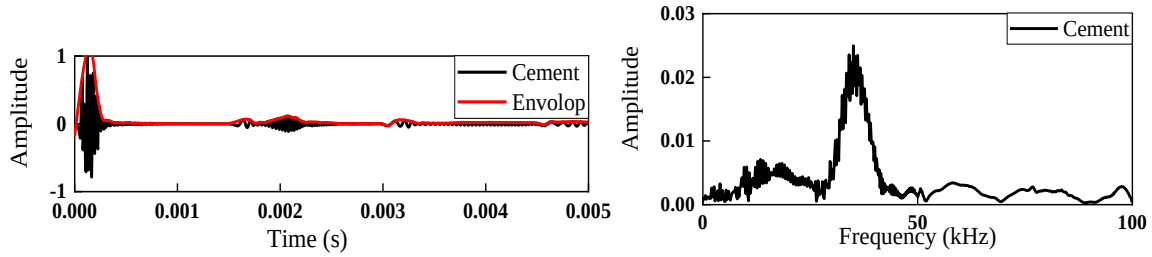

(c)

Figure 71. Received signals for rods with different grout methods. (a) no grout; (b) grease; (c) cement.

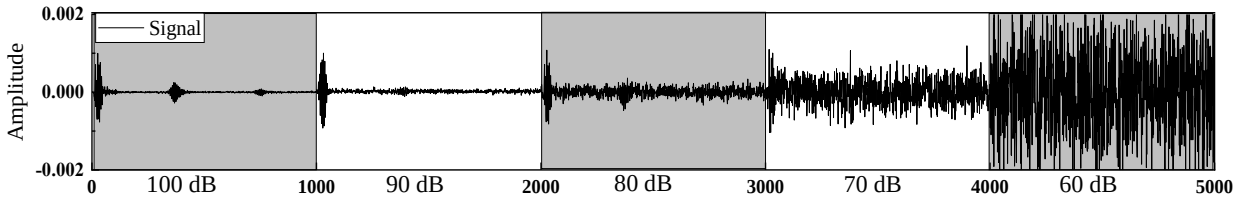

Figure 72. Received signal in different noise level.

6.3. Deep Learning Framework

CNN has been widespread adopted in many application domains, such as image classification and segmentation, speech recognition, and computer vision tasks. The CNN framework contains multi-layers, which includes convolutional layer, pooling layer, full connect layer and ReLU layer. These layers help to decode the input data into high-dimensional slices, extract the intricate features, and then encode into the target values. In this study, CNN was used to identify the complicate guided wave signals. The architecture of the CNN trained by guided wave signals was described. The model of the CNN was changed from LeNet-5. After several layers' cooperation, the initial data is changed into a series of feature maps, and the size is deformed. To transfer these feature maps into its own category, a fully connected layer is necessary. The result of this layer was the probability that the data belongs to each label. The entire process was shown in Figure 73.

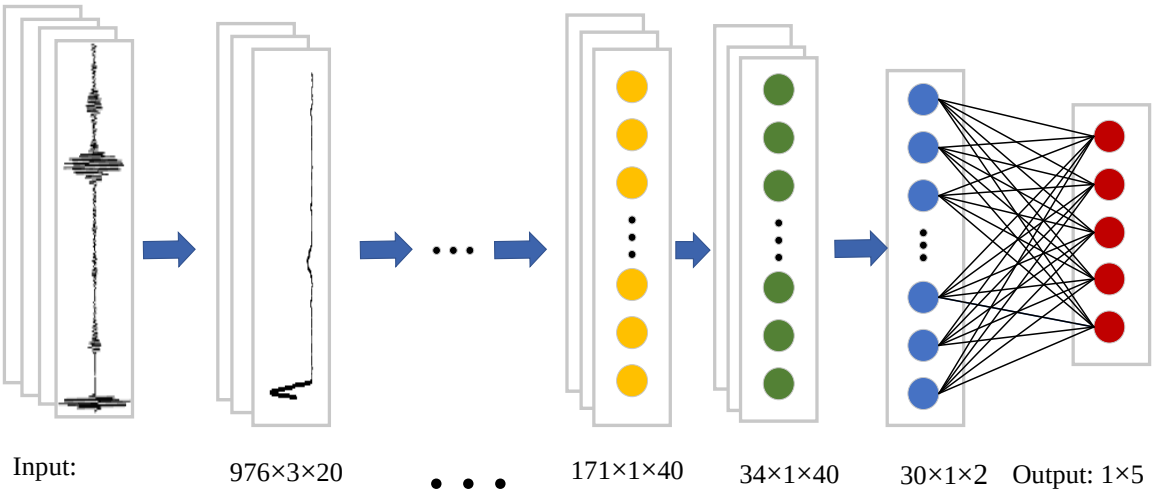

Figure 73. Flow chart of CNN.

6.3.1. CNN Architecture

The proposed CNN in this study was an 8-layer network, including 3 convolutional layers, two max pooling layers, a ReLU layer, a full connected layer and a softmax layer. The detail information of each CNN layer was shown in Table 18.

The input data was a matrix sized 1000×4, representing 4 collected signals in a rod sample. 1000 data points was intercepted from received signals in which included the excitation, and the reflection from the right boundary. 4 means the number of received signals. In the first convolutional layer, 20 filters sized 25×2 were generated and operated the input data into 976×3×20. The following was a max pooling layer with the stride equal to 5. The layer captured the maximum value in the response field and significantly cut down the size of the input. After that, the output of the data was 195×3×20. Then, the data experienced another pair of cooperation from convolutional layer and max pooling layer, where 40 filters involved in, and the pooling size was 5×1. At this moment, the output was 34×1, which had a dramatically declined comparing with the initial input. The third convolutional layer had small size with 5×1, and then a ReLU was implemented to increase the nonlinearity. Finally, the full connected layer and Softmax layer transferred the data into several probabilities in each label.

Table 18. Details of the proposed CNN.

Name	Filters	Filter size	Stride	Bias	Output layer size
Input layer	--	--	--	--	1000×4
Convolutional layer (C_1)	20	25×2	1	20	976×3
Max pooling layer (P_1)	20	5×1	5	--	195×3
Convolutional layer (C_2)	40	25×3	1	40	171×1
Max pooling layer (P_1)	40	5×1	5	--	34×1
Convolutional layer (C_3)	20	5×1	1	20	30×1
ReLU	--	--	--	--	30×1
Full connected layer (F_1)	5	30*1	1	5	5
Softmax	--	--	--	--	5

6.3.2. Feature Visualization with T-SNE

CNN classifier has been achieved quite better performance since the automatically extracted features form the training data. It expands the data into high dimensional matrices by multiple filters. Thus, these features are usually high-dimensional, which is not conductive to understanding. However, stochastic neighbor embedding (SNE) was introduced to reduce the dimension of the feature, which becomes susceptible to visualizing the feature. It aims to convert the high dimensional Euclidean distance between data samples into conditional probabilities. The t-distributed stochastic neighbor embedding (*t*-SNE) (Maaten and Hinton 2008) proposed by Maaten and Hinton, which transforms a high-dimensional dataset into a pairwise similarity matrix and minimize the gap between the distribution in two space. Most recently, this method is popular for feature visualization in machine learning algorithm.

6.4. Results and Discussion

6.4.1. Feature Visualization

In this study, 500 data in each state was emerged by adding white Gaussian noise, including 60% data for training, 20% for validation and 20% for testing. The CNN model was well trained after studying the features from training data. The feature maps can estimate the efficiency of the proposed method. The following figures indicated the high-dimensional feature maps into two-dimensional space by *t*-SNE.

Figure 74 depicted the features in Case 1, where the prestress level of the unembedded rod was classified in 80 dB. States #1 to 5 were represented the rod with the prestress level equal to 0% (base state), 20% UTS, 40% UTS, 60% UTS and 80% UTS. Specifically, 2500 samples were consisted the dataset, where 1500 of them were used to train the model, 500 for validation and the rest 500 data for test. Figure 74(a) displayed the feature maps of the test set after the first convolutional layer. Through the distribution of features, it obvious that data labeled in 40% UTS (green upper triangle) was isolated from the entire data. This represents that the features in this label were much easier to be separated to others. However, the clusters in red diamond (Base state) and yellow circle (20% UTS) located at the right side were overlapped. At least 1/4 data was mixed and difficult to separate. In addition, the rod samples prestressed in 60% UTS (blue lower triangle) and 80% UTS (purple star) were tangled together. Figure 74(b) represented the feature maps from the last layer of CNN. Clearly, after 8 layers' processing, most of the sample were separated expect one outlier in base class and a small overlap between the samples in 60% UTS and 80% UTS. Results demonstrated that features became more sensitive after operating the whole CNN process.

The CNN model sliced input signals into several small pieces which enlarged the sensitive features and cut off the excess. Figure 75 plotted the feature maps from 5 different prestress levels

after three convolutional layers. The data are signals from 5 different prestress levels in Case 1 when SNR is equal to 100 dB. The differences among 5 figures were clearly. The shape and peak values of lines character signals from different groups. However, with the noise level increase, extracting features became harder.

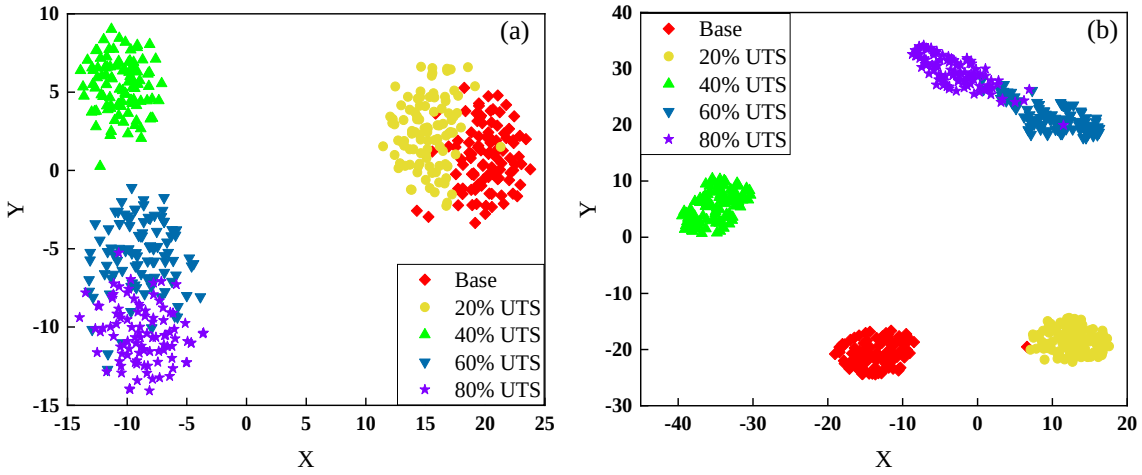

Figure 74. Feature visualization by t-SNE. (a) Feature maps in first convolutional layer; (b) Feature maps in the last layer.

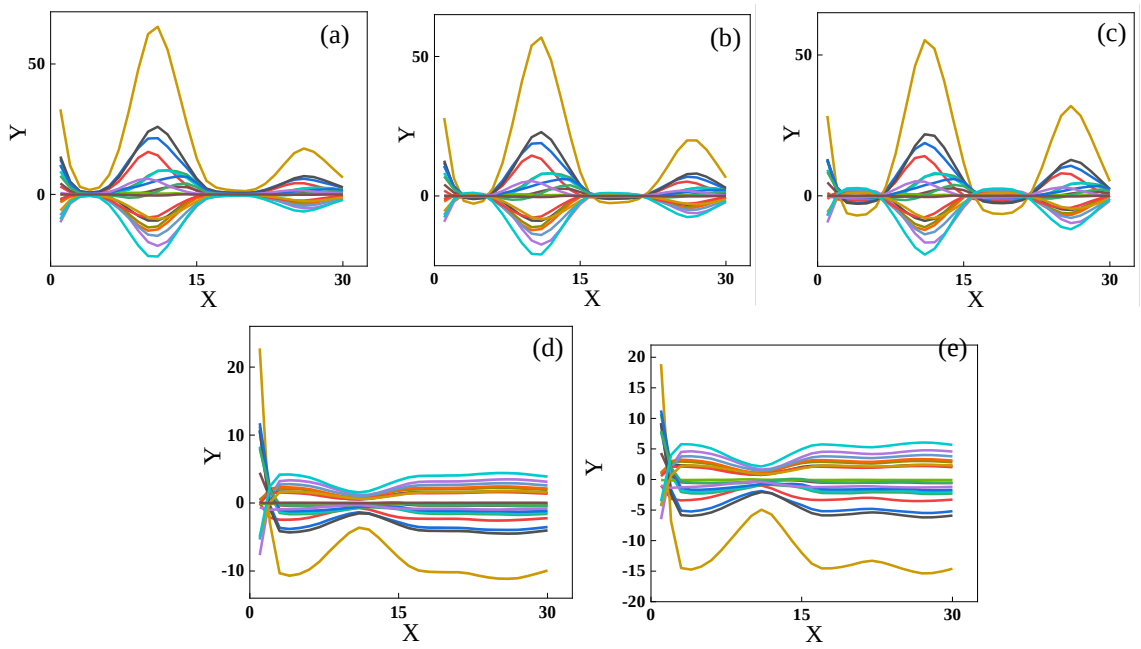

Figure 75. Feature maps: (a) 0% UTS; (b) 20% UTS; (c) 40% UTS; (d) 60% UTS; (e) 80% UTS.

Figure 76 illustrated the feature visualization in Case 1 when SNRs were equal to 100 dB, 70 dB and 60 dB. In 100 dB (in Figure 76(a)), the 5 clusters were far away from each other, and each cluster of data is relatively concentrated with an average standard deviation close to 2.53. With the noise level increased to 80 dB (shown in Figure 76(b)), a small overlap appeared between the 60% UTS and 80% UTS data, but the other three groups were clearly separated. The standard deviation in this situation was large to 2.83. However, when SNR lower than 80 dB, the distributions of features were changed dramatically. In 70 dB, features in either Base state and 20% UTS, or 60% UTS and 80% UTS were blend into each other, and only the data in green upper triangle were independently located below the graph, demonstrated in Figure 76(b). In Figure 76(c), feature maps in 60 dB had the worse situation that all the data interwove together entirely. It is hard to get the boundaries of each group. Therefore, it proved that noise had an adverse effect on the feature extraction of CNN.

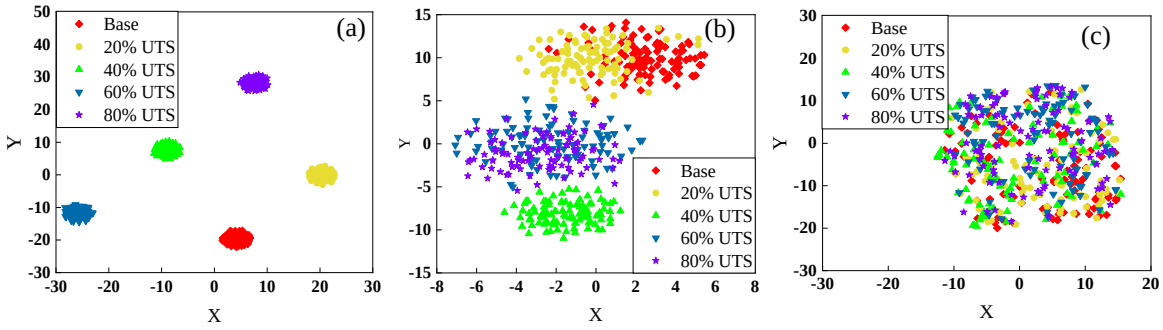

Figure 76. Feature visualization by t-SNE: (a) SNR = 100 dB; (b) SNR = 70 dB; (c) SNR = 60 dB.

6.4.2. Classification for Prestress Levels of the Rod by CNN

The performance of CNN trained by the data under various noise levels was shown in Figure 77, which classified the prestress levels of the rod in Case 1. 1500 of the 2500 data were used for training the CNN model and the training curves were illustrated in Figure 77(a). Specifically, these training curves were started near 20%, and then converged to 100%. When the

noise level was 100 dB, the model only spent 7 epochs to improve the accuracy equal to 100%. That epoch number was enlarged to 25 in 90 dB. With SNR increased, more epochs were spent on converging, where the error reduced to 0 at 34 epochs in 80 dB. The slope of training curves from 100 dB to 80 dB were much larger than the curves in 70 dB and 60 dB. In detail, the accuracy of classification was raised from 20% to 31% by 15 epochs in 60 dB and then close to 100% after the 30th epoch. The validation set included 500 data points for modifying the parameters in CNN. The validation curves for 40 epochs showed that the accuracy of CNN stated at 20% and increased with the epochs. In 100 dB and 90 dB, the accuracies reached to 100% after 6 and 20 epochs' training, respectively. When SNR was 80 dB, the curve was close to 0.98 after the 28th epoch and would not improve as the epoch increased. However, the accuracies were lower at 70 dB and 60 dB, where the curve converged to 0.78 and 0.34 after 40 epochs' training. It reported that 32% of the data would be misjudged as the incorrect category in 70 dB. The situation in 60 dB was much worse that most of the data could not be classified into right category.

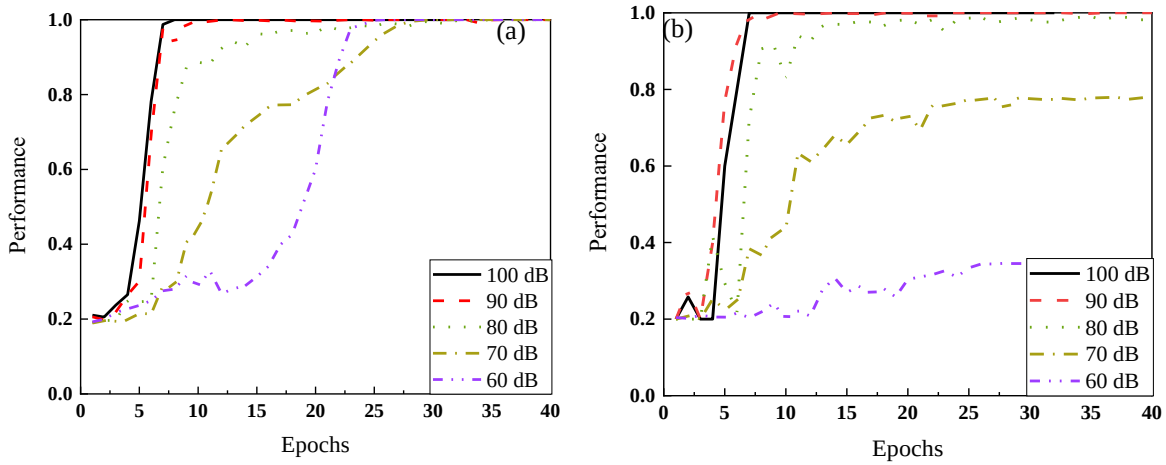

Figure 77. Learning result of CNN at various noise levels: (a) Training curve; (b) Test curve.

The test results in various noise levels were shown in Table 19. When SNR no less than 90 dB, the CNN model was classified the test data correctly into the corresponding category because the training curves and the validation curves reach to 100% after training. In 80 dB, the whole

accuracy of test was 98%, where some misjudgments were appeared in base state and 80% UTS state. The results of the feature maps visualization have already showed the trend that some data in base state was drop into the 20% UTS group, and cluster 60% UTS and cluster 80% UTS were overlapped (shown in Figure 77(b)). The mix features caused the misjudgments in the test. In 70 dB, only 74% of the data was identified correctly. Obviously, 25% data in the first category were misclassified into the second category, on the contrary, 27% of the data belonged to second category were misled into the first category. The accuracies of the fourth and fifth categories were both equal to 63%. The conclusion was consistent with the previous analysis in feature visualization and accurate curves. In 60 dB, CNN model was not suitable in this situation due to the noise were covered the signals entirely and all the analysis focused on the noise. Thus, all results were low accuracy.

Table 19. Confusion matrices in various noise levels.

	90 dB (100%)					**80 dB (98%)**				
	Base	**20%**	**40%**	**60%**	**80%**	**Base**	**20%**	**40%**	**60%**	**80%**
Base	100.0%	0.0%	0.0%	0.0%	0.0%	99.0%	0.0%	0.0%	0.0%	0.0%
20%	0.0%	100.0%	0.0%	0.0%	0.0%	1.0%	100%	0.0%	0.0%	0.0%
40%	0.0%	0.0%	100.0%	0.0%	0.0%	0.0%	0.0%	100%	0.0%	0.0%
60%	0.0%	0.0%	0.0%	100.0%	0.0%	0.0%	0.0%	0.0%	98%	7.0%
80%	0.0%	0.0%	0.0%	0.0%	100.0%	0.0%	0.0%	0.0%	2.0%	93.0%
	70 dB (74%)					**60 dB (26.8%)**				
Base	75%	27.0%	0.0%	0.0%	0.0%	28.0%	27.0%	20.0%	12.0%	15.0%
20%	25.0%	71.0%	1.0%	0.0%	0.0%	28.0%	22.0%	17.0%	15.0%	12.0%
40%	0.0%	0.0%	98%	0.0%	0.0%	20.0%	16.0%	34.0%	17.0%	22.0%
60%	0.0%	1.0%	1.0%	63.0%	37.0%	14.0%	14.0%	12.0%	23.0%	15.0%
80%	0.0%	1.0%	0.0%	37.0%	63.0%	10.0%	21.0%	17.0%	33.0%	36.0%

The performance of the CNN classifier in Case 2 and 3 was shown in Figure 78. In Case 2, rods were embedded in cement. The training and validation results in 5 noise levels were illustrated in Figure 78(a). Obviously, the training and validation curves had better results when SNRs were higher than 70 dB. All the curves were fluctuated at the first 5 epochs and then fast converged to 0. Nearly 10 epochs time was spent to decrease the accuracies into 100%. In 70 dB, although the training curve took about 20 epochs to converge to 100%, the validation curve only reached to 0.78. However, the performance of the CNN dropped sharply at 60 dB. In Case 3, the error was occurred in 80 dB where the training accuracy and validation accuracy were close to 0.99 and 0.94 respectively. The error rate increased at 70 dB where the validation curve arrived 0.77 at the 20th epoch and then it flattened out. Results in Case 3 were similar with that of Case 1 due to the grease had less effect on guided wave propagation.

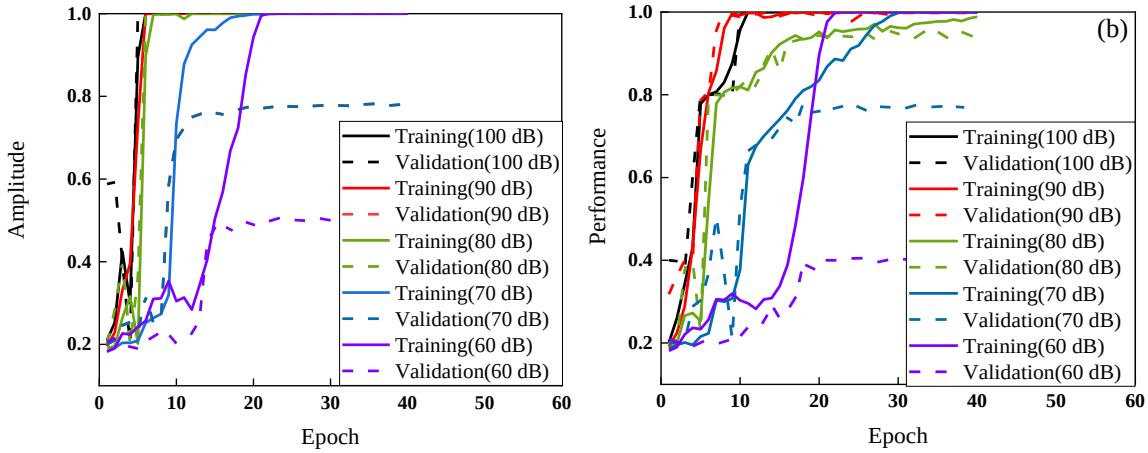

Figure 78. Results of CNN at various noise levels: (a) Case 2; (b) Case 3.

The test results of Case 2 and 3 were shown in Table 20 and 21 when SNRs were from 90 dB to 60 dB. In Case 2, all the test data was identified correctly in 90 dB and 80 dB. In 70 dB, only the base state had a classification rate of 98% and the other 4 groups had lower rates. Among them, 12 of 100 data samples in the second category were misclassified into the third and fourth categories. The accuracy of the third category was 74% with 26% misjudgment. In addition, the

error rate in fourth and fifth categories were 66% and 64%, respectively. When the noise level increased to 60 dB, the accuracy of prestress identification was lowest (46.6%). Most of the data could not be identified except the data in base condition (at 99%). Comparing with Case 2, the approach exhibited a slightly lower accuracy for Case 3, in which 100% data in 90 dB was classified, 94.4% of the data was identified in 80 dB, the ratio was 76% in 70 dB and the accuracy decreased to 41.6% in 60 dB. In 80 dB and 70 dB, most of the errors occurred between the fourth and the fifth categories. Specifically, the predictions of the fourth and fifth categories reached 78% and 94% in 80 dB. In 70 dB, the proportions were reduced to 52% and 51%, respectively. In 60 dB, only the data under base condition could be identified, and it was hard for the data in other conditions.

Table 20. Confusion matrices in Case 2.

Case 2 (Grease as the grout material)										
	90 dB (100%)					**80 dB (100%)**				
	Base	**20%**	**40%**	**60%**	**80%**	**Base**	**20%**	**40%**	**60%**	**80%**
Base	100.0%	0.0%	0.0%	0.0%	0.0%	100.0%	0.0%	0.0%	0.0%	0.0%
20%	0.0%	100.0%	0.0%	0.0%	0.0%	0.0%	100.0%	2.0%	5.0%	4.0%
40%	0.0%	0.0%	100.0%	0.0%	0.0%	0.0%	8.0%	100.0%	15.0%	18.0%
60%	0.0%	0.0%	0.0%	100.0%	0.0%	0.0%	4.0%	14.0%	100.0%	14.0%
80%	0.0%	0.0%	0.0%	0.0%	100.0%	0.0%	0.0%	10.0%	14.0%	100.0%
	70 dB (78%)					**60 dB (46.6%)**				
Base	98%	0.0%	0.0%	0.0%	0.0%	99%	1%	0%	1%	0%
20%	2.0%	88%	2.0%	5.0%	4.0%	0%	50%	16%	29%	8%
40%	0.0%	8.0%	74%	15.0%	18.0%	0%	13%	24%	16%	25%
60%	0.0%	4.0%	14.0%	66%	14.0%	1%	26%	31%	26%	33%
80%	0.0%	0.0%	10.0%	14.0%	64.0%	0%	10%	29%	28%	34%

Table 21. Confusion matrices in Case 3.

Case 3 (Cement as the grout material)										
	90 dB (100%)					80 dB (94.4%)				
Base	100.0%	0.0%	0.0%	0.0%	0.0%	100.0%	0.0%	0.0%	0.0%	0.0%
20%	0.0%	100.0%	0.0%	0.0%	0.0%	0.0%	100.0%	0.0%	0.0%	0.0%
40%	0.0%	0.0%	100.0%	0.0%	0.0%	0.0%	0.0%	100.0%	0.0%	0.0%
60%	0.0%	0.0%	0.0%	100.0%	0.0%	0.0%	0.0%	0.0%	78.0%	6.0%
80%	0.0%	0.0%	0.0%	0.0%	100.0%	0.0%	0.0%	0.0%	22.0%	94.0%
	70 dB (76%)					60 dB (41.6%)				
Base	99.0%	1.0%	0.0%	0.0%	0.0%	79.0%	18.0%	2.0%	5.0%	3.0%
20%	0.0%	99.0%	0.0%	0.0%	0.0%	18.0%	38.0%	20.0%	9.0%	11.0%
40%	1.0%	0.0%	79.0%	13.0%	12.0%	1.0%	19.0%	29.0%	29.0%	23.0%
60%	0.0%	0.0%	11.0%	52.0%	37.0%	1.0%	15.0%	25.0%	27.0%	28.0%
80%	0.0%	0.0%	10.0%	35.0%	51.0%	1.0%	10.0%	24.0%	30.0%	35.0%

6.4.3. Classification for Embedding Situation by CNN

The embedding situation of the rod could also be predicted by CNN classifier. A total of 1500 data sample was used for training the CNN, including unembedded rods, rods embedded with cement and rods embedded with grease. The Training and validation curves were shown in Figure 79. At lower noise level, the classifier was entirely predicted the state of the rod. Until SNR was 70 dB, the validation curve was reached 0.956, which experienced 40 epochs' training. However, the accuracies in 60 dB dropped sharply. Test results were indicated in Table 22. Predictions were equal to 100% in each category when SNRs were from 100 dB to 80 dB. Several errors were occurred in 70 dB and the accuracy was 92%. Specifically, the rod samples labeled in unembedded were much easier to be confused into the rod embedded in grease, in which 15% of

the data in that category were misclassified into grease state. On the other hand, 7 of 100 data were misclassified into unembedded state. Only 1% data in cement was predicted incorrect. The worst results were the classification in 60 dB, the total accuracy was only 35% which means the model cannot identify the signals.

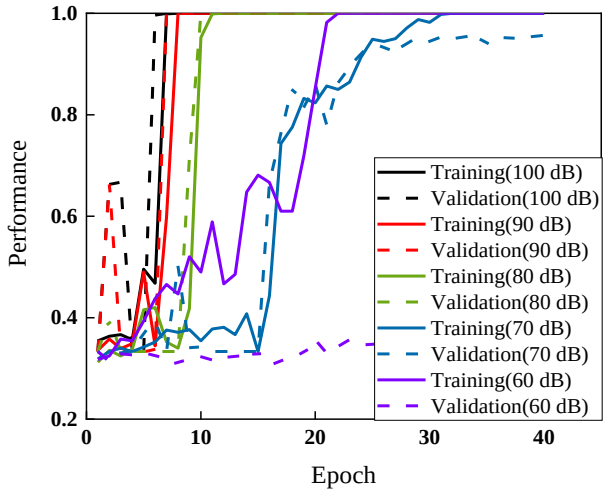

Figure 79. Results of CNN at various noise levels.

Table 22. Confusion matrices in varying embedding conditions.

	90 dB (100%)			80 dB (100%)		
	Unembedded	**Cement**	**Grease**	**Unembedded**	**Cement**	**Grease**
Unembedded	100.0%	0.0%	0.0%	100.0%	0.0%	0.0%
Cement	0.0%	100.0%	0.0%	0.0%	100.0%	0.0%
Grease	0.0%	0.0%	100.0%	0.0%	0.0%	100.0%
	70 dB (92%)			**60 dB (35%)**		
Unembedded	84.0%	0.0%	7.0%	37.0%	24.0%	39.0%
Cement	1.0%	99.0%	0.0%	28.0%	43.0%	36.0%
Grease	15.0%	1.0%	93.0%	35.0%	33.0%	25.0%

6.5. Summary

This study investigated the deep learning based guided wave process for stress level prediction of the prestressed rods. The CNN model was established for automatically encoding the hidden information from complex signals that accounted for the impacts of different noise levels and embedded grout materials. Some conclusions can be listed as follows:

a) Deep learning method effectively encoded the guided waves under complex uncertainties and assisted in stress level prediction and the embedded conditions of the rods, thereby offering great potentials for signal process of NDE methods in structural health monitoring of PC structures.

b) Feature visualization method, t-SNE, provided an effective window that the different feature patterns could be clearly identified from visual two-dimensional plot. The distances between each feature point were clearly indicated the correlation among data. In addition, the impacts of noise interference on the data were obviously observed with the use of this approach.

c) The deep learning approach also exhibited high accuracy and robustness for data with high noise interference. The CNN classification for most cases could reach up to 100%, when the noise levels were lower (80 dB – 100 dB). However, with the energy of the noise (SNR = 70 dB) close to the signals, data classification exhibited certain level of reduction, which the error rates were close to 80%. Particularly, when the noise increased to a much higher level (60 dB), all the signals were totally contaminated, which was the reason why the effectiveness of the classification dropped.

6.6. Reference

Beard, M. D. and M. Lowe (2003). "Non-destructive testing of rock bolts using guided ultrasonic waves." *International Journal of Rock Mechanics and Mining Sciences* 40(4): 527–536.

James A. Evans and Richard W. Haskins. (2015). "Detection of Microcracks in Trunnion Rods Using Ultrasonic Guided Waves." *Information Technology Laboratory.*

Maaten, L. v. d. and G. Hinton (2008). "Visualizing data using t-SNE." *Journal of machine learning research* 9(Nov): 2579-2605.

7. DEEP CNN BASED DAMAGE DETECTION FOR STRUCTURES WITH WELDMENT BY ULTRASONIC GUIDED WAVES

7.1. Introduction

Data-driven methods received wide attention in structural health monitoring system (SHM) due to the broad range of applications. Ultrasonic guided wave, a non-destructive testing, is a rapid and efficient method to detect the minute cracks. Despite a mass of research was devoted to simplifying the wave modes propagated in the structure, the interpretation of the hidden information from signals and the extraction of damage-sensitive and noise-robust features is still challenge especially in complicated structures. In order to overcome the challenges, the frameworks of machine learning-based damage detection systems were set up with shallow learning and deep learning algorithms respectively. In addition, deep learning method, a 20-layer residual network (ResNet), was adopted for damage detection and localization in pipeline with welding part, accelerating the entire processing and leading to more accurate predictions. Overall, 4 Cases were component by 16 damage states, attempting to investigate the classification capability of the proposed network from damage location, type, severity and more complex situations. The performance of each ResNet was estimated by training and validation accuracy curves, loss curves and confusion matrices. The results indicated that the networks can correctly classify the damage state in low noise level (not lower than 80 dB). Only a few errors were occurred at 70 dB. and the accuracy dropped dramatically at 60 dB. Although the predictions were not entirely correct under high level noise condition, the accuracies were much higher than the results calculated by shallow learning method (SVM) and short layer deep network (CNN). It verified that the proposed approach is implemented effectively and accurately for ultrasonic guided wave-based damage detection

7.2. Machine Learning-based Damage Detection Method

Machine learning-based damage detection methods aimed to develop trainable algorithms that could identify a set of representative features from provided dataset, and then classify future damage signals (Pan, Azimi et al. 2018, Pan, Zhang et al. 2019, Zhang, Wang et al. 2019). These algorithms are not only generally used for a series of problems, but also contained the characteristics of data itself. In this study, damage was detected through ultrasonic guided wave propagating in the pipeline and classified by supervised machine learning algorithms. These algorithms were divided into shallow learning-based damage detection and deep leaning-based damage detection, shown in Figure 80.

Shallow learning-based damage detection contained 4 main steps in Figure 80 (a): (a) data acquisition, (b) feature extraction and selection, (c) label data, (d) classification and prediction. In detail, raw data, a set of time series data, was acquired by the propagation of ultrasonic guided waves. At first, the data operated by the processes of data normalization and data cleansing. Next, features were extracted by statistic model (Zhang, Pan et al. 2020) (e.g., amplitude, RSM and correlation coefficient) or analytical models (Pan, Lin et al. 2019) (e.g., vector autoregressive model, singular value decomposition and autoregressive model) in different domain. To apply more sensitive features for data training, feature selection was engaged herein as a critical step. Furthermore, shallow learning methods (e.g., support vector machine, random forest and k-nearest neighbor) were employed to training and validating data by labeled training set and testing set. However, methods based on shallow learning require complicated processes and are not suitable for high-dimensional sensory data.

The strategy of deep learning-based damage detection was automatically extracted and selected features from raw data; thus, the procedure, shown in Figure 80 (b), was much more

simplified, which consisted (a) data acquisition and labeled, (b) classification by deep learning methods, (c) prediction. Specifically, data was generated and label at first, and then separated into training set and validation set. In order to abstract high-level details from original data, deep learning algorithms stacked block of multiple convolutional layers with nonlinear mappings(Azimi, Eslamlou et al. 2020). Trough the training and validation, well-trained and high accuracy classifiers were built for predicting. Accordingly, deep learning-based damage detection gets rid of the shortcomings from shallow learning, which has the brief procedures and is workable for high-dimensional sensor system.

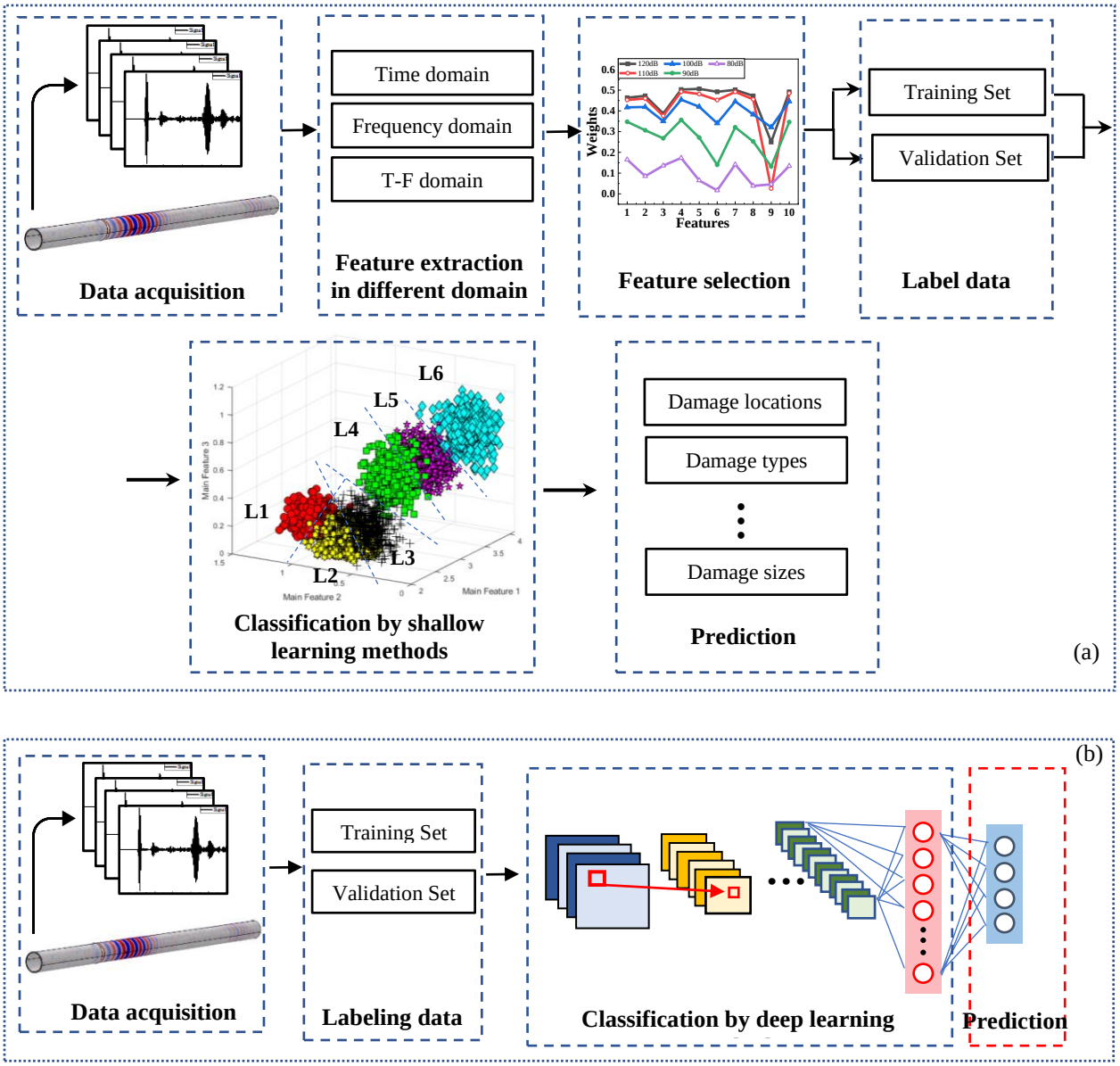

Figure 80. Frameworks of machine learning based damage detection methods: (a) shallow learning, (b) deep learning.

7.2.1. Residual Network (ResNet)

The deep convolutional neural network has been widely used in the area of computer vision (Gopalakrishnan, Khaitan et al. 2017, Layouni, Hamdi et al. 2017), natural language processing (Conneau, Schwenk et al. 2016) and biomedical systems(Pourbabaee, Roshtkhari et al. 2018), which have outperformed shallow learning models. Since Krizhevsky et al.(Krizhevsky, Sutskever et al. 2012) introduced AlexNet in 2012, the architecture of the convolutional network has become deeper and more complicated. While the problems of vanishing or exploding gradients has been solved by normalized initialization (Glorot and Bengio 2010, LeCun, Bottou et al. 2012) and intermediate normalization layers (Ioffe and Szegedy 2015) , the degradation problem was also exposed for deep networks. This issue was addressed by Resnet. He et al. (He, Zhang et al. 2016) proposed residual learning framework which was substantially deeper and easier to train than the previous networks. The empirical results from Szegedy showed that ResNet had the advantage of fast convergence (Szegedy, Ioffe et al. 2016). Subsequently, ResNet was originally applied for time series data by Wang et al. (Wang, Yan et al. 2017), who tested 44 distinct datasets from UCR.

In this section, a 20-layer ResNet was established for ultrasonic guided wave-based damage detection. The input layer was the waves received in the simulation of pipe. The main structure of the Resnet was illustrated in Figure 81 which contains 19 convolutional layers and one fully connected layer. After each convolutional layer, a batch normalization layer and a rectifier linear Unit (ReLu) are followed. The special part in ResNet is the identify shortcut connections which addressed the degradation problem.

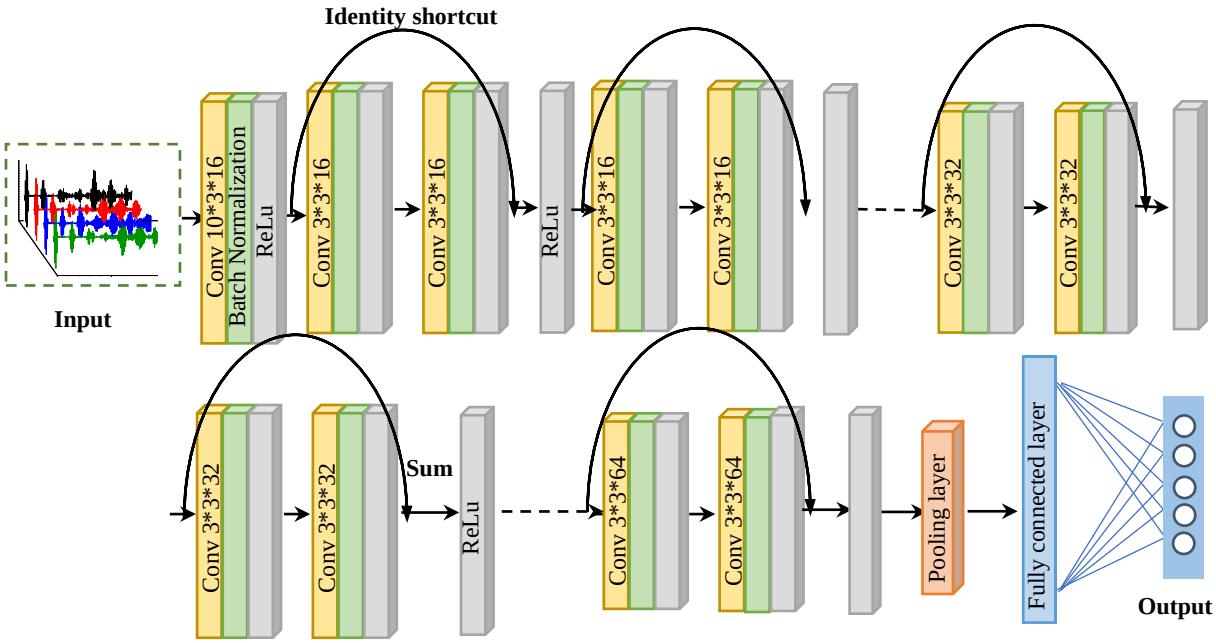

Figure 81. The architecture of 20-layer ResNet.

7.2.2. Batch Normalization

Batch normalization (BN) was created to improve the training of deep neural networks and avoid activation explosion by repeatedly fixing the input of intermediate layers to zero-mean and constant standard deviation(Ioffe and Szegedy 2015). The application of this mechanism has successfully proliferated in most of deep architectural techniques which got the beneficial effect on increasing the training speed, leaning rate and accuracy (Bjorck, Gomes et al. 2018, Santurkar, Tsipras et al. 2018). In ResNet, BN, as a layer perceptron, was a part of the building block. The BN layer can be expressed as

$$f = \delta(\hat{x}) \tag{54}$$

$$\hat{x} = \frac{x - \mu}{\sigma}\gamma + \beta \tag{55}$$

where f is the output of each layer, $\delta(x)$ represents the activation function, $\hat{x}$ is the hidden value after batch normalization layer. μ and σ are the mean and standard deviation calculated from the input x. γ and β represent the scale parameter and shift parameter.

7.2.3. Identity Shortcut Connections

With the converging of the deeper networks, several issues were exposed, such as vanishing/exploding gradients, degradation issues. The accuracy was arising, reached saturation and then degraded sharply as the network depth increased. The obstruction was not resulted in overfitting but the depth of the networks. However, identity shortcut connections avoid the degradation happened in deep network by adding low-level features directly to high-level features (He, Zhang et al. 2016, Li and He 2018). It has been proved to be the best solution for ResNet at present, with neither extra parameter nor computational complexity (He, Zhang et al. 2016).

The building block (Residual Units) of two stacked layers was illustrated in Figure 82. Assume that the input vector of the building block is x, then the output $H(x)$ is expressed as (He, Zhang et al. 2016)

$$H(x) = F(x) + x \tag{56}$$

$$F(x) = W_2\delta(W_1x) \tag{57}$$

where, $F(x)$ is the residual mapping, W_1 and W_2 are the weights in the first and second convolutional layer and $\delta(x)$ represents the activation function.

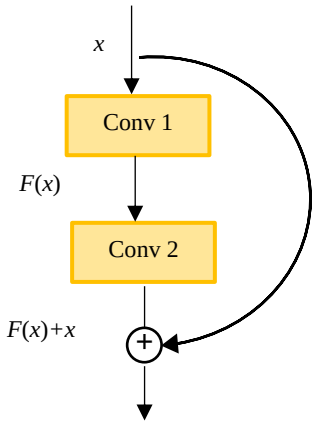

Figure 82. The building block of ResNet.

7.2.4. Loss Function

Loss function, as a part of the optimization algorithm, was introduce in neural networks to estimate the deviations between the forecasted and actual categories. The critical of it is faithfully distill all the parameters of the model into a signal number. Base on this criterion, loss function updates the parameters in networks through the gradient, thereby reducing the loss of output. Loss can be separated into classification and regression loss. The common loss functions for classification are square loss, exponential loss, hinge loss and cross-entropy loss. In this proposed network, Softmax loss combined with cross-entropy was used as a loss function. Softmax function was used to obtain the prediction probability that input signals belongs to each class. Then, cross-entropy loss was used to determine the distance between the predicted distribution and the target distribution. The function was expressed as

$$\hat{y} = log \frac{e^{W_j^{\mathrm{T}} x^{(i)}}}{\sum_{j=1}^{m} e^{W_j^{\mathrm{T}} x^{(i)}}} \tag{58}$$

$$L(y, \hat{y}) = -\frac{1}{n} \sum_{i=1}^{n} 1\{\hat{y}_i = y_i\} log \hat{y} \tag{59}$$

where W is the weight; x(i) is the value of the i^{th} sample; $\hat{y}$ represents the predicted probability for the i^{th} sample calculated by Softmax function; y_i is the target label of the i^{th} sample and n is sample number.

7.2.5. Architecture of ResNet

In this section, a 20-layer ResNet was selected as training model for the following dataset. More layers such as 34-layer or 56-layer networks may improve the accuracy of predictions to some extent, however, more parameters will occur during training process, resulting long computing time. In addition, the basic structure of the ResNet with different layers is similar, excepted the number of building block. Thus, the detail configuration was listed in Table 23. For

instance, the input data was consisted by several signal matrices sized 2000×4. A convolutional layer, a BN layer and a ReLu layer were composed as a convolutional block. In the first convolutional block, 16 convolutional filters sized 10×3 were decreased the input data into 1993×4. BN layer and ReLu layer were not affect the size of the output. Then, 6 convolutional blocks(C_2) were stacked as follow. In each C_2, 16 kernels (3×3) made the multiplication with the input in receptive field. Due to the special structure of identity shortcut connection, the output size obtained by the ResNet unit containing two convolutional blocks should be the same as the input size, thus they can be added reasonably. As such, the padding was set to balance the dimensions of input and output. The strides in C_3 and C_4 were designed as 3 and these down sampling operations made the dimension of output reduced sharply. Before the last full connection layer, a pooling layer was built, and then through the full connection layer, the final output was a vector which size was equal to the number of categories.

Table 23. Detail of the proposed ResNet-20.

Name	Filters	Filter size	Stride	number	Output layer size
Input layer	--	--	--	--	2000×4
Convolutional block (C_1)	16	10×3	1	1	1993×4
Convolutional block (C_2)	16	3×3	1	6	1993×4
Convolutional block (C_3)	32	3×3	3	6	665×2
Convolutional block (C_4)	64	3×3	3	6	222×1
Full connected layer (F_1)	6	215×1	1	1	1×6

7.3. Case Study

7.3.1. An Ultrasonic Guided Wave-based Damage Detection System of a Pipeline

Ultrasonic guided wave with high frequency nature was more sensitive for testing the quality of welding and detecting tiny material discontinue. The waves were generated by piezoelectrical actuators which convert the voltage signals into mechanical signals. Then these waves propagated in the pipe until meet the damage or boundary. The reflected signals will bring the detailed information about damages. Hence, the decoding techniques such as deep learning methods can help to interpret and classify of the ultrasonic signals.

As a case study, a steel pipe model was designed in finite element software. The prototype of the model was from literature (Xu, Luo et al. 2019) which is a 2000 mm-long pipeline with two cuts as the damage located at 1400mm away from the left side. The out diameter was 76 mm with the wall thickness of 4 mm. Ultrasonic waves were involved to detect the damage appeared in pipeline. In paper (Xu, Luo et al. 2019), the excitation wave was a 10-cycle sinusoidal signal with a frequency of 120 kHz operated by Hanning window. Therefore, the verification of the simulation was shown in Figure 83. The compared signal was an experiment results from one actuator in paper (Xu, Luo et al. 2019). The simulation result was from the model built in this section. For a more intuitive comparison, the amplitudes of the simulation data and experiment data were normalized. Clearly, the input data was same, and the position of damage and boundary reflection was similar. Some distinction occur was because of the difference in material parameter. Therefore, the validation of the numerical simulation model was verified, and the model was used as a fundamental simulation to generate more dataset for further research.

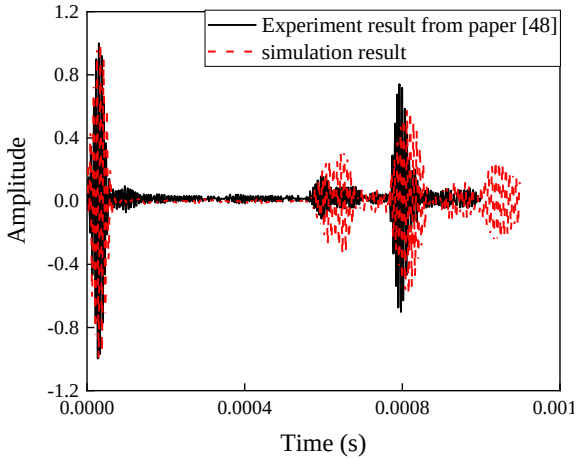

Figure 83. Calibration of simulation.

For the following study, damage locations, types and severities are detected by ultrasonic guided wave, thus, more complicated conditions were designed in this section. To obtain more general results and reduce the uncertainty from geometric parameters, most of dimensions involved in the model were designed as multiples of the outer diameter (D = 76 mm) of the pipe. Specifically, the length of the pipeline was 20*D (approximately 1520 mm), the welding position was located at 5*D from the left side and the damage was in the middle of the pipe. 64 excited nodes were axisymmetrically placed at the left end and 4 receivers were located at the adjacent 15 mm on the left recorded the echoes. Figure 84 demonstrated the detail of the pipeline. Position A to D represented the location of excitations, receivers, welding, and damage respectively. A V-shaped butt-welding joint was sized 10 mm in outside width and 4 mm higher than the pipe. The material of welding filler was Ti-6Al-4V which the density of this material is 4453 kg/m3, Young's modulus is 125.8 GPa and Poisson's ration is 0.40. The pipeline model was meshed by free tetrahedral element, with 5 mm as the maximum element size, and 0.5 mm the minimum element size. The time step was 0.5 E-7 s. In order to simplify the reflected wave package from multi different damage, we used a 100kHz 5-cycle signals to instead. These was less effect for the model, due to the velocities of the guided wave were closed at 100 kHz and 120 kHz.

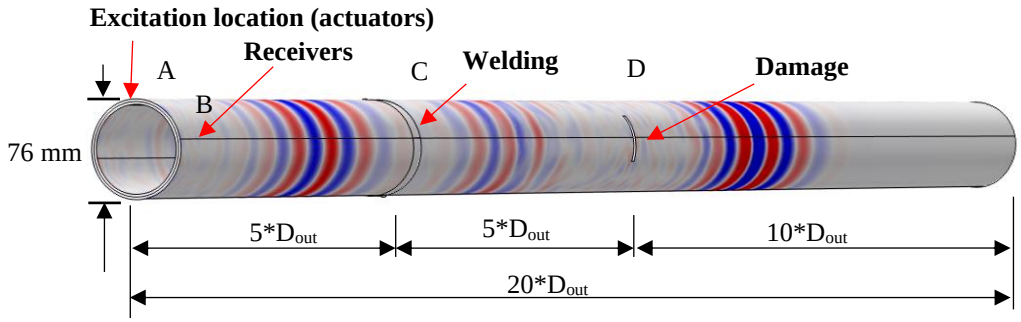

Figure 84. Simulation model of the pipeline.

7.3.2. Data Acquisition and Labeling

Overall, 16 states were designed in this research to explore the characteristics of the damage, including damage locations, types, severities, and the combination between them. Two types of risks commonly occurred in pipelines due to the aging and loading, one is cracks, and the other was welding defects. Through-the-thickness notches were modeled as cracks in this simulation, and the welding defects were composed 4 damage patterns, including lack of fusion, cracks and undercut, lake of penetration. The length of notches was 0.1*D (0.76 mm) and the width was 10^{-4} mm. The welding defects had 3 severities with 1%, 5% and 10%. The location of the welding was fixed, but 5 different locations (0.5*D, 1*D, 2*D, 5*D, 10*D) of the crack was planned in State #2 to 6. State #7-11 was investigated the crack locations under more complicated situations (welding defect appeared at the meanwhile). Further, the types (State #10, 12~14) and severities (State #10, 15, 16) of the welding defects was detected by ultrasonic waves. The detailed information was illustrated in Table 24. Five noise levels from 60 dB to 100 dB were added by additive white Gaussian noise to enlarge data and increase uncertainties.

In order to describe the performance of the proposed network in different areas, 4 main characteristics were considered in this study. The detection of damage location consisted of the data in State #1 to 6 (Case 1), including reference state and five different positions. In addition,

damage location was still inspected in State #1, 7-11 (Case 2), which existed the welding detect in pipeline, to investigate the model capability under more complex condition. Since the welding part is one of the most commonly problems in pipeline disaster, and it is also a difficult issue for inspection. As such, the third and fourth cases was focused on the types and severities of the welding defects.

Table 24. Data acquisition and labeling.

Case	Label	Damage location	Welding defect patterns	Severity of welding defect	Noise Interference
Reference	State #1	/	/	/	Noise levels of from 60dB to 100dB
Variance due to damage locations (Case 1)	State #2~6	0.5* D_{out} ~10* D_{out}	/	/	
Variance due to damage locations (Case 2)	State #7~11	0.5* D_{out} ~10* D_{out}	Defect 1	1%	
Variance due to the types of weld defect (Case 3)	State #10~14	5* D_{out}	Defect 1 ~4	1%	
Variance due to severities of weld detect (Case 4)	State #10, 15, 16	5* D_{out}	Defect 1	1%, 5%, 10%	

7.3.3. Design and Training ResNet-based Damage Detection

ResNet-based damage detection method was attempted to classify the damage categories from the received ultrasonic data. In contrast to image classification, the input data was consisted by multiple 1-dimensional signals. Thus, the ResNet was modified for damage detection tasks. For training network model, 2000 samples of each scenario were generated by additive white Gaussian noise, which included 60% for training, 20% for validating and 20% for testing.

To clearly understand the learning process of ResNet model, a sample chosen from State #1 to #6 was experienced the whole procedure and predicted its category. Several feature maps getting from the middle layers was depicted Figure 85. The input data was a 2000×4 matrix in which each receiver collected one time series data. Multiplications were performed element by element between input data and filters during each convolutional layer. Two large-scale reductions in data length were happened after the 8^{th} and 15^{th} convolutional layers since the stride was equal to 3. Obviously, in the feature maps of the 8^{th} and 15^{th} convolutional layers, the original signals were split by convolutional kennels, which decomposed into 32 and 64 slices respectively. Each slice contained different information due to the different filters. With the layers getting deeper, the feature maps became more abstractive. The reason was that deeper layers were attempted to encode high level abstractions, and simple features, like shapes, were much easier to be detected by lower layers. In deeper feature maps, some trivial content seemed to be omitted, and important features were retained. Whether the information was significant or not was judged by the network. Clearly, for the input signals, the most important factors were including two main wave packets (one was the excitation, the other was the echo from boundary.) and some small packets echoed from welding or damage located at middle. During the entire network, these features were continuously extracted. The feature maps became sparser at the last pooling layer. The efficient characteristic has been learned. Then through the full connected layer, all the information has been absorbed by the network and transformed into the probability of each category. The result indicated that the input was near 99.8% belonging to State #1.

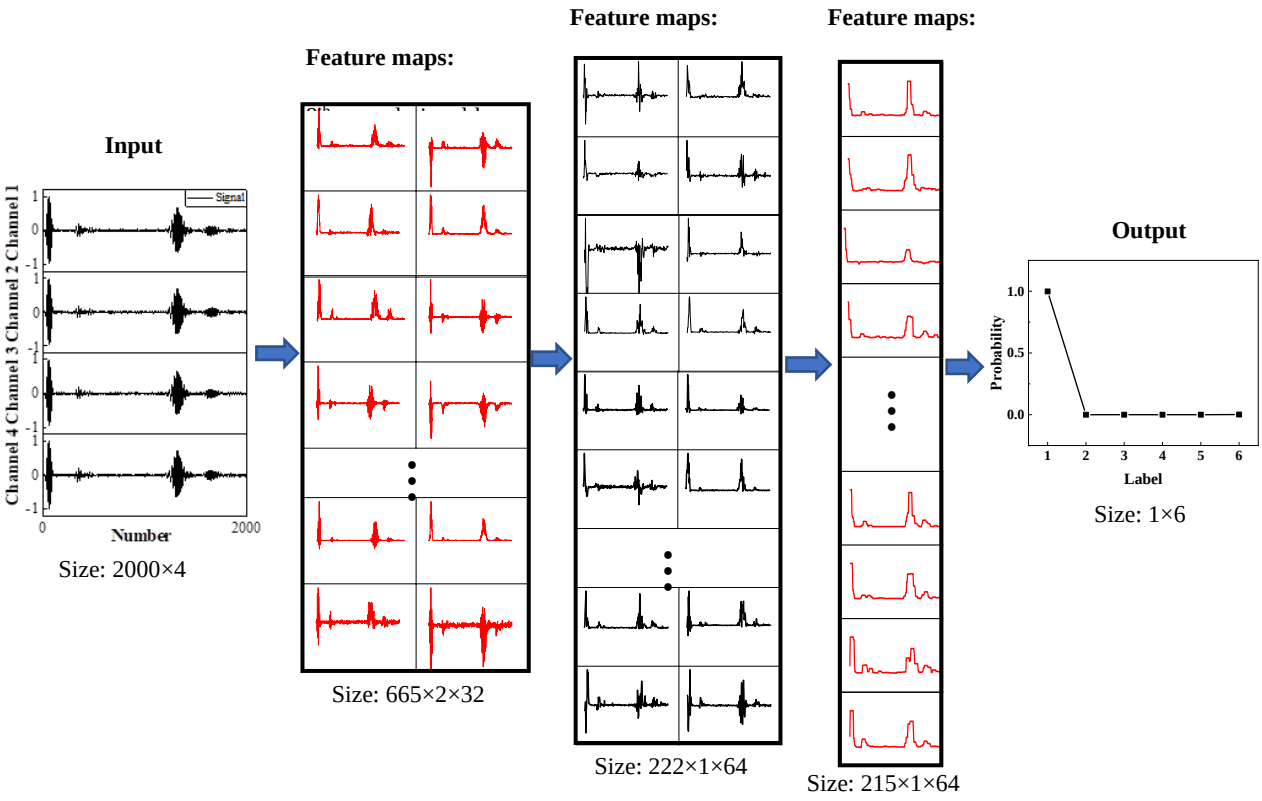

Figure 85. Feature maps in ResNet.

7.4. Results and Discussion

7.4.1. Damage Location Identification: Case 1 and 2

The damage location classification calculated by ResNet were illustrated in Figure 86 when SNRs were equal to 80 dB and 70 dB. It is observed that with the epoch increased, the loss of training and validation was decreased, and the accuracy of training and validation was risen. The confusion matrices were demonstrated the testing results in each category. The ResNet classifier could 100% predict the data with the SNR higher than 80 dB. When noise level was 80 dB, in Figure 86 (a), the losses of the training and validation dropped rapidly at the first 100 epochs, and then converged to zero at the 400th epoch. Meanwhile, the accuracies were increased sharply and then steadily approached to 99%. 99.08% of the testing data was classified correctly, however the misleading was mainly happened when damaged located at 5*D and 10*D. Since the noise level

increased, the training and validation errors could not converge to zero which were closed to 0.08 and 0.14 respectively. The losses were just reached to 0.2 approximately after 2500 epochs' update. The training results caused the low accuracy of the test set with 91.25% in which 219 of the testing data was classified into incorrect label. The results signified that noise level was one of the most essential factors which lead to the reduction of predicted accuracy.

Figure 87 depicted the case that identifying the damage location with the interference of the welding defect. However, these results were a little bit better than before under the same noise level. It seems that when the complication of the signals increase, the model can extract features much more easily. Specifically, the losses were close to 0.1 at the 3000^{th} epoch and the accuracies of training and validation were 95% and 92.7%. The prediction result for testing was 94.08%, which had 1.5% error rate in label 1 D (State #8) and 1% in 2 D (State #9), 75 data in State #10 were misjudged into State #11 and 57 data were judged incorrectly to State #10. In the 60 dB state, the training and validation error were as high as 11.4% and 28.6%. Similarly, loss values were also high to 0.27 and 0.76 respectively. The testing accuracy was only 81.21% where the worse classification occurred in 5 D. The reason was that the reflection waves were overlapped when damage position was 5*D away from the welding part. Although the result in high noise level was not accurately enough, the performance of the proposed network was acceptable due to the signals were submerged by the high-level noise.

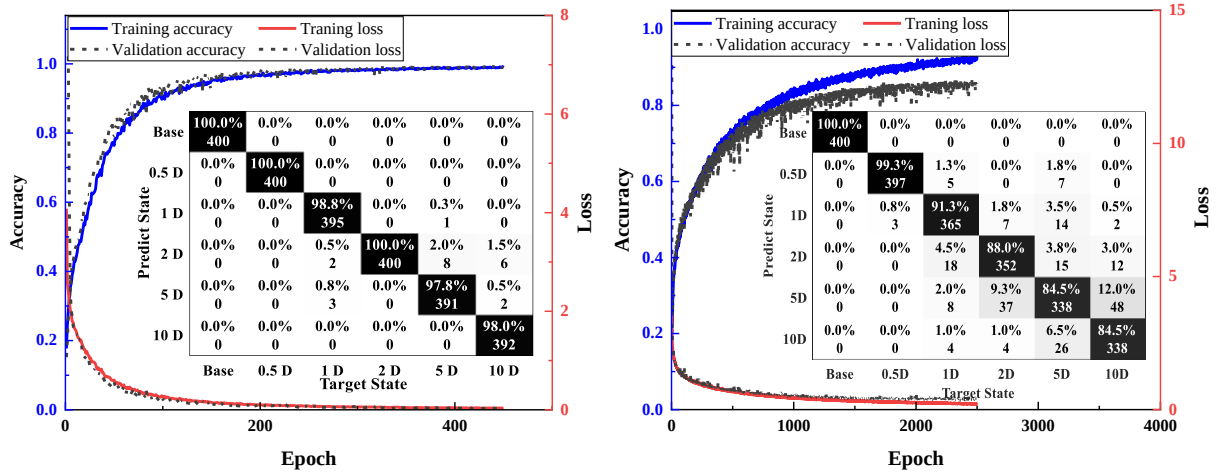

Figure 86. Result of notch-shaped damage location (pipe with health welding): (a) SNR = 80 dB; (b) SNR = 70 dB.

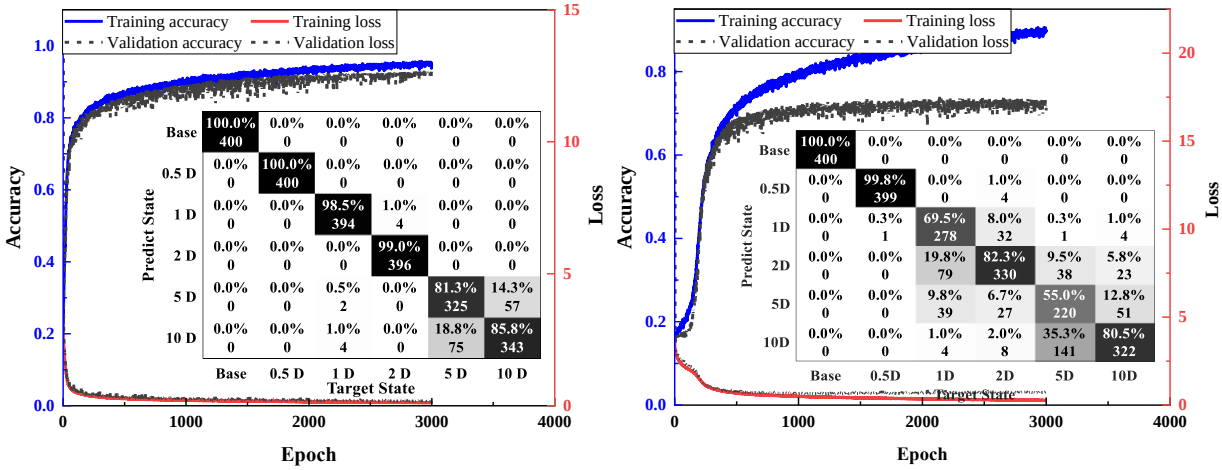

Figure 87. Result of notch-shaped damage location (pipe with welding defects): (a) SNR = 70 dB; (b) SNR = 60 dB.

7.4.2. Identification of Welding Defect Types and Severities: Case 3 and 4

Four welding defects and the reference state were identified by the trainable ResNet model. Figure 88 illustrated the training and predicting results at 70 dB and 60 dB respectively. When noise level was 70 dB, the model spent nearly 200 epochs to increase the accuracies from zero to 95% then approach to 99.8% at the 3000th epoch. The losses were decreased dramatically which means the distance between the prediction and the target label became shorter. The testing result showed the gap with the target state which only 10 of the signals with undercut damage (Defect 3)

misled into lake of penetration (Defect 4) and other labels were predicted 100 % correctly. With the noise increased, the model training became difficult, which required more epochs to minimize the loss and maximize the accuracies. At 60 dB, the validation accuracy was reached to 96% a little bit lower than that of training. As the same, the value of validation loss was 0.1 after the training, noted that some deviation was still existed during prediction. The mainly errors were happened on the distinction of Defect 3 and 4, and the error rates were 14.5% and 17% respectively.

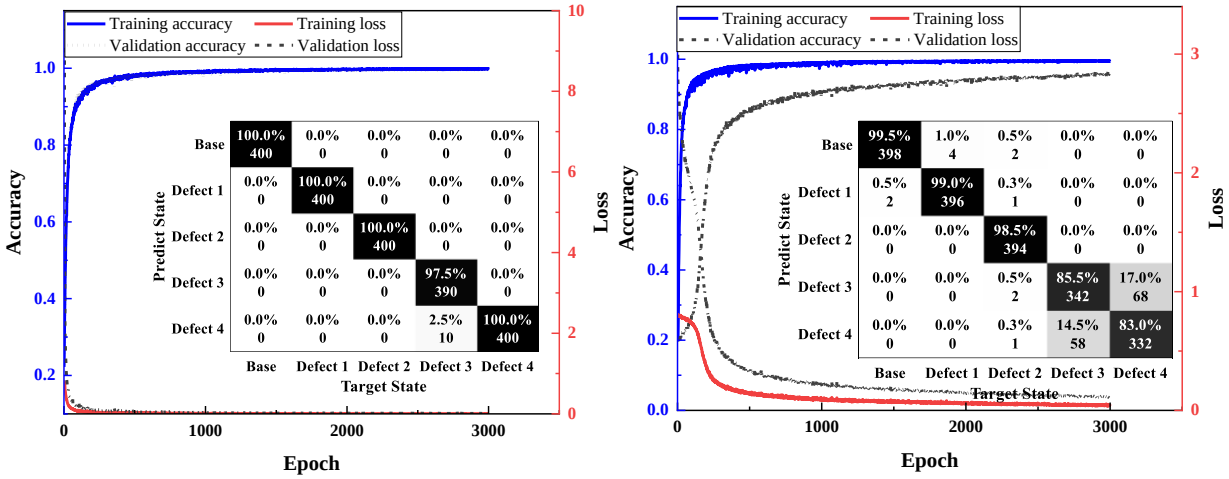

Figure 88. Result of damage types: (a) SNR = 70 dB; (b) SNR = 60 dB.

The detection of welding defect severity is also a tricky issue for ultrasonic guided wave methods. Three different sizes were 10%, 5% and 1% respectively. The convergences of the learning network were demonstrated in Figure 89. In both 70 dB and 60 dB, the training could not arrive 100%, as about 92% and 72% respectively. In addition, the testing results were 88.75% and 62.5% that was worse than the identification of damage types. Most of the signals in base state and label 5% were predicted rightly, but the accuracies labeled 10% (State #16) and 1% (State #10) were much lower, with 79.3% and 93.5% at 70 dB and 34% and 45% at 60 dB. Clearly, signals from State #15 (which 5% welding was lacking fusion) was more likely to extract the features.

However, when the SNR was higher than 70 dB the signals could entirely classify into the real label by the ResNet.

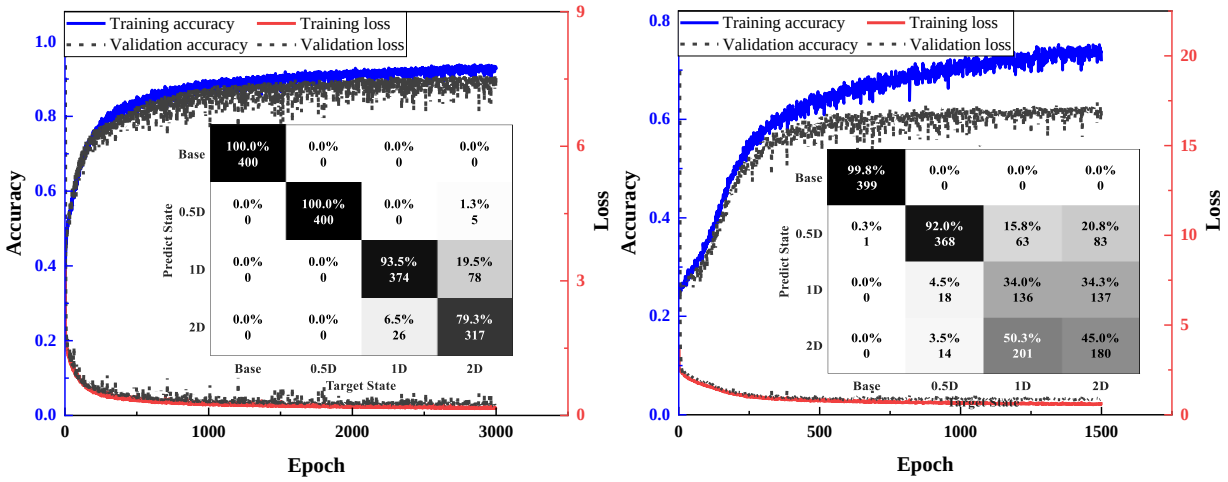

Figure 89. Result of damage severity: (a) SNR = 70 dB; (b) SNR = 60 dB.

7.5. The Effectiveness of Damage Identification Comparing with Other Methods

To estimate the effectiveness of proposed network, a comparison study was conducted among SVM, CNN and ResNet. On the one hand, shallow learning-based damage detection was employed to obtain the prediction from ultrasonic signals. Note that the feature extraction was a critical step for classification. Thus, 4 different feature groups were used to train the SVM, including wavelet coefficients (SVM_WT), physics-based features (SVM_PH), all the features coming from wavelet coefficients and physics-based (SVM_ALL) and features from feature selection method (SVM_FS). Specifically, the ultrasonic signals were decomposed by wavelet transform which had the property of local zooming, and 10 of wavelet coefficients were selected as the features used to classify the data in SVM_WT method. Physics-based parameters could also express the distance between the signals collected in different states, including amplitude, root mean square and correlation coefficient. Then SVM_ALL method was introduced all the features (from wavelet coefficients and physics-based parameters) to adopt the model. The fourth one,

feature selection method, Relief_F, were combined with SVM to rank the proposed features and 10 items with the highest scores were used in SVM_FS method to identify the ultrasonic signals.

On the other hand, deep learning-based damage detection was trained to improve the accuracy of the damage classification and broader applications. Two deep neural networks, an eight-layer CNN and the proposed ResNet with twenty layers, were involved in this study, attempting to compare their performance. Analogously, the dataset was partitioned into training, validation and test set, which 60% was occupied by training data, validation and testing datasets were account for 20% respectively.

Accordingly, all the testing results computed by these methods were shown in Table 25-Table 28. Specifically, most of the methods could classify the damage characteristics entirely correct in all these cases at 100 dB, except the SVM_WT. However, as the noise increased, every approached had a decline in accuracy to some extent. In general, comparing with two detection systems, deep learning-based detection achieved high accuracies than that of shallow learning methods. For instance, in Case 1, the predictions in the SVM_WT and SVM_PH methods have been misjudged at 100 dB and 90 dB. The detection accuracy of shallow learning was not higher than 74% in 70 dB, while the figures of deep learning methods were 92.33% and 91.25% respectively. The same phenomenon occurred in Cases 2 to 4, where the deep learning methods enhance the accuracy of the damage detection. In addition, when SNR was not less than 70 dB, the results classified by CNN model and ResNet model were pretty close. As noise level was 60 dB, the advantage of the ResNet was obvious that the accuracies have been improved to a certain extent, especially in Cases 1 to 3.

Table 25. The result in Case1.

	100 dB	90 dB	80 dB	70 dB	60 dB
SVM_WT	89.6%	80%	53.33%	23.53%	16.8%
SVM_PH	**100%**	94.2%	65.13%	30.33%	16.13%
SVM_ALL	**100%**	**100%**	99.93%	74%	28.67%
SVM_FS	**100%**	**100%**	97.93%	64.6%	32.07%
CNN	**100%**	**100%**	**100%**	**92.33%**	35%
Resnet	**100%**	**100%**	99.08%	**91.25%**	**55.58%**

Table 26. The result in Case2.

	100 dB	90 dB	80 dB	70 dB	60 dB
SVM_WT	97.32%	83.2%	57.27%	24.2%	
SVM_PH	**100%**	99.93%	72.87%	27.67%	15.8%
SVM_ALL	**100%**	**100%**	99.4%	83.4%	40.27%
SVM_FS	**100%**	**100%**	98.87%	82.8%	39.93%
CNN	**100%**	**100%**	**100%**	**95%**	68%
Resnet	**100%**	**100%**	**100%**	**94.08%**	**81.21%**

Table 27. The result in Case3.

	100 dB	90 dB	80 dB	70 dB	60 dB
SVM_WT	**100%**	98.32%	50.48%	22.48%	19.36%
SVM_PH	**100%**	98.32%	67.28%	38.32%	20.8%
SVM_ALL	**100%**	**100%**	**100%**	96.71%	60.16%
SVM_FS	**100%**	**100%**	**100%**	96.72%	64.56%
CNN	**100%**	**100%**	**100%**	**99.4%**	75.4%
Resnet	**100%**	**100%**	**100%**	**99.5%**	**93.10%**

Table 28. The result in Case4.

	100 dB	**90 dB**	**80 dB**	**70 dB**	**60 dB**
SVM_WT	98.5%	84.1%	57.3%	31.4%	26.5%
SVM_PH	**100%**	91.1%	64.9%	42.2%	26.5%
SVM_ALL	**100%**	**100%**	**100%**	84.00%	46.4%
SVM_FS	**100%**	**100%**	98.4%	77.9%	49.9%
CNN	**100%**	**100%**	**100%**	88.75%	62.5%
Resnet	**100%**	**100%**	**100%**	**93.19%**	**67.69%**

Three measures, precision, recall and F1-score, were popular used in classification problem to estimate the effectiveness of an empirical decision system. The predictions can be separated into 4 groups, true positives (TP) where the classes are predicted correctly into positive, true negatives (TN) where the class are predicted correctly into negative, false positives (FP) that the actual classes are negative but predicts into positive and false negatives (FN) that the actual classes are positive but predicted into negative. Precision is the ratio of predicted positive cases which are correctly real positives which can be calculated as $P = TP/(TP + FP)$. Conversely, recall denotes the ration of real positive case that are correctly predicted positive which is expressed as $R = TP/(TP + FN)$. F1_score represents the weighted average of precision and recall which is equal to $2 * PR/(P + R)$. Figure 90 and Figure 91 depicted the boxplots of these three measures in different methods in Case 2 when nose levels were 70 dB and 60 dB. Clearly, SVM_WT and SVM_PH methods had low proportions which means that for complexity signals, the characteristics from only one aspect factors could not represent the signals well. When multiple features ensembled together, the results became better such as SVM_ALL and SVM_FS, but the range of the proportion was large from 0.6 to1 and the average ratios were 0.8 approximately. The

larger range represented that the classifier performed better in some categories but worse in others. CNN and ResNet were got the highest scores, resulting the best performances. In 60 dB, four SVM-based methods were failure to detect, while ResNet was superior to others and acquired the highest accuracy proportions. Meanwhile, CNN model also showed the shortcomings in this situation which caused the range of the scores were larger. Consequently, the proposed method, ResNet, can be verified more suitable for ultrasonic guided wave-base damage detection.

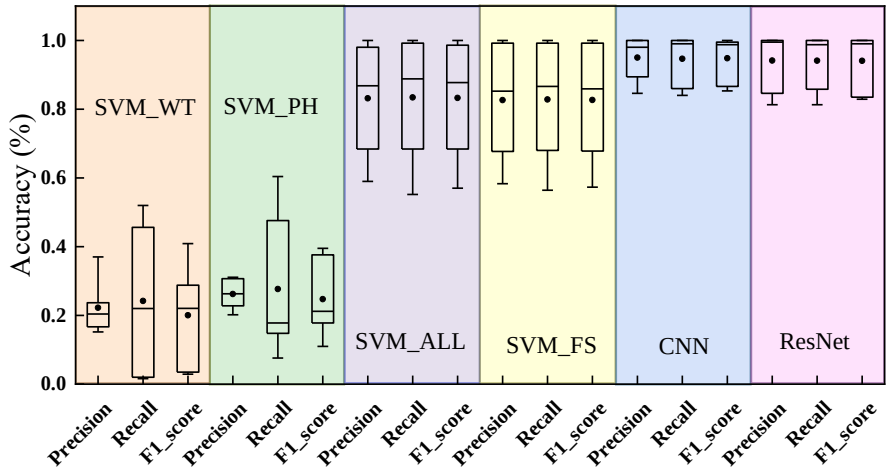

Figure 90. Parametric comparison in different models in Case 2 (70 dB).

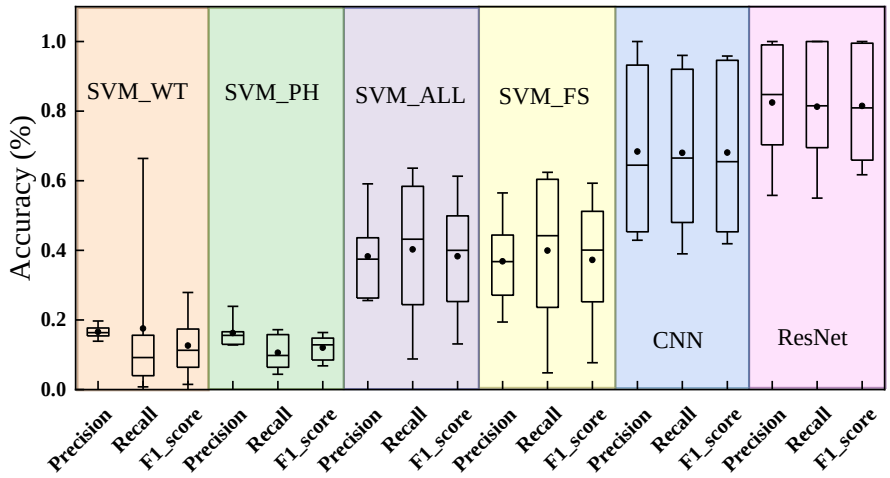

Figure 91. Parametric comparison in different models in Case 2 (60 dB).

7.6. Summary

In this section, ultrasonic guided wave testing coupled with deep learning approaches was proposed to identify the pipeline structures damage locations, types, and severities. Ultrasonic guided wave was propagated through the pipeline established by simulation and collected as the dataset. 4 main Cases were established from 16 distinct damage states, corresponding to four aspects to investigate the general applications of this method. A 20-layer ResNet were designed and then training by response signal groups. The damage detection results were associated with the classification categories, where each category represents the damage state of the pipeline. Impacts of welding defects and tiny cracks were comprehensively considered. The conclusions can be summarized as follows,

(a) The frameworks of machine learning-based damage detection systems were provided from data acquisition to decision making, involving shallow learning approaches and deep learning approaches. Comparing with the conventional techniques, these approaches were simplified the process, improved the accuracy and effective for data-intensive system.

(b) The prediction results indicated that the proposed network, ResNet, could accurately and effectively localize and estimate the damage, especially when SNRs were not lower than 80 dB. The accuracy decreased sharply to 55.58% in Case 1 and 93.1% in Case 3 when noise level increased into 60 dB.

(c) The effectiveness of the ResNet model was not affected when welding defect appeared to impact the classification of damage localization, as Case 2. The accuracy results were arrived to 99.5% and 93.1% while SNRs were 70 dB and 60 dB.

(d) The comparation were emerged between shallow learning methods (SVM with four different feature selection) and deep learning methods (CNN and ResNet). The results

demonstrated that, deep learning methods got higher accuracies in all the cases and obtained higher scores in precision, recall and F1-score.

(e) When noise interference existed, deep learning methods, especially ResNet, effectively improved the robustness of the damage detection methods and addressed the shortcomings in shallow learning. In addition, CNN and ResNet got similar results as noise lever no less than 70 dB, however, the advantage of ResNet was obvious under 60 dB noise, where improved the accuracy to some extent.

7.7. Reference

Azimi, M., A. D. Eslamlou and G. Pekcan (2020). "Data-Driven Structural Health Monitoring and Damage Detection through Deep Learning: State-of-the-Art Review." *Sensors* 20(10): 2778.

Bjorck, N., C. P. Gomes, B. Selman and K. Q. Weinberger (2018). *Understanding batch normalization*. Advances in Neural Information Processing Systems.

Conneau, A., H. Schwenk, L. Barrault and Y. Lecun (2016). "Very deep convolutional networks for natural language processing." *Computation and Language* 2.

Glorot, X. and Y. Bengio (2010). *Understanding the difficulty of training deep feedforward neural networks*. Proceedings of the thirteenth international conference on artificial intelligence and statistics.

Gopalakrishnan, K., S. K. Khaitan, A. Choudhary and A. Agrawal (2017). "Deep convolutional neural networks with transfer learning for computer vision-based data-driven pavement distress detection." *Construction and Building Materials* 157: 322-330.

He, K., X. Zhang, S. Ren and J. Sun (2016). *Deep residual learning for image recognition*. Proceedings of the IEEE conference on computer vision and pattern recognition.

He, K., X. Zhang, S. Ren and J. Sun (2016). *Identity mappings in deep residual networks*. European conference on computer vision, Springer.

Ioffe, S. and C. Szegedy (2015). "Batch normalization: Accelerating deep network training by reducing internal covariate shift." *arXiv preprint arXiv:1502.03167*.

Krizhevsky, A., I. Sutskever and G. E. Hinton (2012). *Imagenet classification with deep convolutional neural networks*. Advances in neural information processing systems.

Layouni, M., M. S. Hamdi and S. Tahar (2017). "Detection and sizing of metal-loss defects in oil and gas pipelines using pattern-adapted wavelets and machine learning." *Applied Soft Computing* 52: 247-261.

LeCun, Y. A., L. Bottou, G. B. Orr and K.-R. Müller (2012). Efficient backprop. *Neural networks: Tricks of the trade*, Springer**:** 9-48.

Li, B. and Y. He (2018). "An improved ResNet based on the adjustable shortcut connections." *IEEE Access* 6: 18967-18974.

Pan, H., M. Azimi, F. Yan and Z. Lin (2018). "Time-frequency-based data-driven structural diagnosis and damage detection for cable-stayed bridges." *Journal of Bridge Engineering* 23(6): 04018033.

Pan, H., Z. Lin and G. Gui (2019). "Enabling Damage Identification of Structures Using Time Series–Based Feature Extraction Algorithms." *Journal of Aerospace Engineering* 32(3): 04019014.

Pan, H., Z. Zhang, X. Wang and Z. Lin (2019). Image-based damage conditional assessment of large-scale infrastructure systems using remote sensing and deep learning approaches. *2019 TechConnect World Innovation Conference*. Boston, MA, USA.

Pourbabaee, B., M. J. Roshtkhari and K. Khorasani (2018). "Deep convolutional neural networks and learning ECG features for screening paroxysmal atrial fibrillation patients." *IEEE Transactions on Systems, Man, and Cybernetics: Systems* 48(12): 2095-2104.

Santurkar, S., D. Tsipras, A. Ilyas and A. Madry (2018). *How does batch normalization help optimization?* Advances in Neural Information Processing Systems.

Szegedy, C., S. Ioffe, V. Vanhoucke and A. Alemi (2016). "Inception-v4, inception-resnet and the impact of residual connections on learning." *arXiv preprint arXiv:1602.07261*.

Wang, Z., W. Yan and T. Oates (2017). *Time series classification from scratch with deep neural networks: A strong baseline*. 2017 International joint conference on neural networks (IJCNN), IEEE.

Xu, Y., M. Luo, Q. Liu, G. Du and G. Song (2019). "PZT transducer array enabled pipeline defect locating based on time-reversal method and matching pursuit de-noising." *Smart Materials Structures* 28(7): 075019.

Zhang, Z., H. Pan, X. Wang and Z. Lin (2020). "Machine Learning-Enriched Lamb Wave Approaches for Automated Damage Detection." *Sensors* 20(6): 1790.

Zhang, Z., X. Wang, H. Pan and Z. Lin (2019). Corrosion-induced damage identification in metallic structures using machine learning approaches. *2019 Defense TechConnect Innovation Summit*. National Harbor, Maryland, USA.

8. CONCLUSIONS AND FUTURE WORK

8.1. Conclusions

The dissertation investigates the ultrasonic guided wave-based damage detection method empowered by artificial intelligence techniques to accelerate the damage diagnosis and prognosis of metallic structures. The ultrasonic guided waves are sensitive to minute damages and tiny anomaly in structures. However, due to intrinsic guided waves propagation and scattering, complex modes generated near defects post great challenges in data classification. Particularly, combined effects introduced from other interferences, including measuring noise and inherent structural uncertainty, hinder the applications of conventional physics-based methods. Artificial intelligence technologies, shallow learning method and deep learning methods, are involved in the study to improve efficiency and accuracy for ultrasonic guided wave-based damage detection.

Metallic structures, thin plate, pipelines and rods, are involved in this study, in which ultrasonic guided waves propagate from one dimension to three dimensions. Several types of damage are discussed such as mechanical damage and environmental damage. In mechanical damage, damage shapes, length, locations, and orientations are identified by proposed method. In environmental damage, the severity of corrosion is considered. In addition, the stress reduction of prestressing components is also concerned. Some conclusions can be drawn as follows:

a) The framework combined with shallow learning and deep learning methods provided a workflow from dataset generation, to sensitive feature extraction, to prediction model for ultrasonic guided-wave-based damage diagnosis and prognosis.

b) Different features generated from different domains could provide various levels of sensitivity to damage. Feature selection could improve the accuracy of classification in

shallow learning-based damage detection. In addition, deep learning method could extract the sensitive features automatically, proved by feature visualization method.

c) Multiple types of defects in metallic structures have been discussed in this study, such as mechanical damage, corrosion, welding defects, and stress reduction. Interactions with different damages were also considered. The proposed method also exhibited high accuracy and robustness for classification

d) Noise interference, mixed data types, and level, and material discontinuity from weldment were used to address structural uncertainty and their impacts to the effectiveness of the proposed methods. The findings revealed that the proposed methods were still effective for data classification.

e) The comparation were emerged between shallow learning methods (SVM with four different feature selection) and deep learning methods (CNN and ResNet). The results demonstrated that, deep learning methods got higher accuracies in all the cases and obtained higher scores in precision, recall and F1-score.

8.2. Future Work

From the results drawn from this research, the following recommendations can be drawn for further research:

a) Since the structural uncertainty and environmental noise cannot be replaced by white noise, future experimental research will concern on the field work to detect the damage of metallic structures.

b) Future work will focus on the analysis of structures in life-cycle by artificial intelligence technique.

c) Ultrasonic guided waves also have good performance on composite material. Thus, future work could also consider the damage detection on composite material structures.